Comprehensive Study of Refractive Index Sensors for Bio-Sensing Applications

by

Tahmina Tabassum Treena (180021106)

Nasir Muhammad Munim (180021312)

Musarrat Amin (180021320)

A Thesis Submitted to the Academic Faculty in Partial Fulfillment of the Requirements for the Degree of

BACHELOR OF SCIENCE IN ELECTRICAL AND ELECTRONIC ENGINEERING

Department of Electrical and Electronic Engineering

Islamic University of Technology (IUT)

Board Bazar, Gazipur-1704, Bangladesh.

June, 2023.

Declaration of Authorship

We, Tahmina Tabassum Treena (**180021106**), Nasir Muhammad Munim (**180021312**), and Musarrat Amin (**180021320**), declare that this thesis titled, '**Comprehensive Study of Refractive Index Sensors for Biosensing Applications**' and the works presented in it are our own. We confirm that:

- This work has been done for the partial fulfillment of the Bachelor of Science in Electrical and Electronic Engineering degree at this university.
- Any part of this thesis has not been submitted anywhere else for obtaining any degree.
- Where we have consulted the published work of others, we have always clearly attributed the sources.

Submitted by:

Treena

____

Tahmina Tabassum Treena

Munim

____

Nasir Muhammad Munim

Musarrat Amin

____

Musarrat Amin

Comprehensive Study of Refractive Index Sensors for Bio-sensing Applications

Approved by:

Iftekhar

____

Dr. Syed Iftekhar Ali (Supervisor)

Professor

Electrical and Electronic Engineering Department,

Islamic University of Technology (IUT),

Boardbazar, Gazipur-1704.

Date: 28/05/2023

Table of Contents

List of Figures

List of Tables

List of Abbreviations

PCF-Photonic Crystal Fiber

SPR-Surface Plasmon Resonance

RIU-Refractive Index Unit

SPP-Surface Plasmon Polariton

FOM-Figure of Merit

PADS-Peak Amplitude Difference Sensitivity

RI-Refractive Index

EM-Electromagnetic

RW-Resonance Wavelength

MIM-Metal-Insulator-Metal

FEM-Finite Element Method

FDTD-Finite Difference Time Domain

PML-Perfectly Matched Layer

ABC-Absorbing Boundary Condition

FIT-Finite Integration Technique

PDE-Partial Differential Equations

WGM-Whispering Gallery Mode

CL-Confinement Loss

MTIR-Modified Total Internal Reflection

EML-Effective Material Loss

FWHM-Full Width Half Maximum

AS-Amplitude Sensitivity

WS-Wavelength Sensitivity

TM-Transverse Magnetic

AZO-Aluminum-doped Zinc Oxide

FIB-Focused Ion Beam

EBL-Electron Beam Lithography

NIL-Nanoimprint Lithography

CVD-Chemical Vapor Deposition

List of Symbols

κ_0 - Wave vector

ω - Angular frequency

c - Speed of light

ε_d - Relative permittivity of dielectric

ε_m - Relative permittivity of metal

η - Refractive index

λ - Wavelength of light

μ_0 - Absolute permeability

ε_0 - Absolute permittivity

P - Polarization

χ_e - Electric susceptibility

$\hbar\omega_p, \omega_d$ - Plasma frequency

Γ_0 - Collision frequency

γ_i - Oscillator strength

Γ_i, γ_D - Damping frequency

ω_i - Resonant frequency

η_{eff} - Effective refractive index

β - Propagation constant

n - Real Part of Effective Refractive Index

k - Imaginary Part of Effective Refractive Index

n_{silica} - Refractive Index of Silica without Strain

n'_{silica} - Refractive Index of Silica with Strain

B_1 - Sellmeier Constant

B_2 - Sellmeier Constant

B_3 - Sellmeier Constant

C_1 - Sellmeier Constant

C_2 - Sellmeier Constant

C_3 - Sellmeier Constant

T - Temperature

ε_z - Strain

P_e - Elastic-optic Constant

ε_{Au} - Permittivity of Gold

ε_∞ - High-frequency Permittivity

$\Delta\varepsilon$ - Weighting Factor

Acknowledgements

First, we would like to express our gratitude to Allah (SWT), the most merciful and compassionate.

We would like to offer our heartiest gratitude to our thesis supervisor Dr. Syed Iftekhar Ali, Professor, Department of Electrical and Electronic Engineering, Islamic University of Technology (IUT), for his invaluable advice, support, and guidelines throughout our studies and research work. We are thankful for all his lessons and knowledge.

We would also like to thank Dr Mohammad Rakibul Islam, Professor and Head of the Department, Department of Electrical and Electronic Engineering, Islamic University of Technology (IUT), for his continuous support and teachings throughout our research journey. We are also grateful to all the faculty members of the Electrical and Electronic Engineering Department, Islamic University of Technology (IUT), for their inspiration and support. Finally, we are thankful to our families for their continuous mental support during the entire writing of this thesis.

Tahmina Tabassum Treena

Nasir Muhammad Munim

Musarrat Amin

June, 2023

Abstract

In this thesis, three high-yielding plasmonic refractive index sensors are proposed to satisfy the current sensing demands in different sectors, for example, medical, forensic, and industrial. The proposed works employ a straight waveguide and octagonal ring resonator, a PCF-SPR sensor using symmetrical arrays of plasmonic layers, and another PCF-SPR sensor with dual plasmonic layers. COMSOL Multiphysics is chosen as the wave-solver, which inherently deploys the Finite Element Method. The re-simulations of existing structures corroborate the computational accuracy of COMSOL Multiphysics. Furthermore, the first two sensors fabricated through nanoimprint lithography technique and the stack-and-draw approach, respectively, exhibit linear correlation with the refractive index and the resonant wavelength. Moreover, the structural parameters of the plasmonic sensors are sensitive to variations. Thus, the suggested sensors undergo extensive simulations and optimization processes to maximize their performance. The proposed first work with the concentric octagonal-ring resonator exhibits a maximum sensitivity of 13157, and a high dip strength of 0.8311 nm/RIU is obtained after optimization. This proposed work is deployed to detect various types of fluids like air, optic oil, and different types of water. The proposed first PCF-SPR sensor displays a wavelength sensitivity of 85,300 nm/RIU and amplitude sensitivity of 800.037 RIU^{-1}. The device has also shown FOM of 370.8 RIU^{-1} which denotes high accuracy and reliability. A novel parameter was proposed in this work named Peak Amplitude Difference Sensitivity (PADS) for higher precision interrogation in case of multiple peak analysis. The proposed third work with dual plasmonic layer shows an initial wavelength sensitivity of 24,000 nm/RIU and 34,000 nm/RIU for two different peaks from 2 different regions. After optimization, the wavelength sensitivity of the second peak was achieved 1,12,500nm/RIU which is one of the highest among its competitors. The amplitude sensitivity was found 1248 RIU^{-1}. The structural parameters will be optimized to maximize the performance of the suggested refractive index sensor in future.

Chapter 1

Introduction and Background

1.1 Surface Plasmon Polariton

In the past, optical devices operated at gigahertz velocities and had micrometer-scale dimensions. The development of semiconductor technology has led to a decrease in component size to the nanometer scale while maintaining the same operating speed. However, these developments are limited by issues such as heat loss and delays in time. The necessity for high-speed optical systems has led to the development of dielectric photonics, which provides operating frequencies in the PHz range and lower device dimensions. Due to light's diffraction limit, the unwieldy nature of dielectric photonics hinders the high-density packaging of optical instruments. Surface plasmon polaritons (SPPs) are developed to bridge the gap between dielectric photonics and semiconductor technologies, allowing for the integration of optical devices on a chip scale [1].

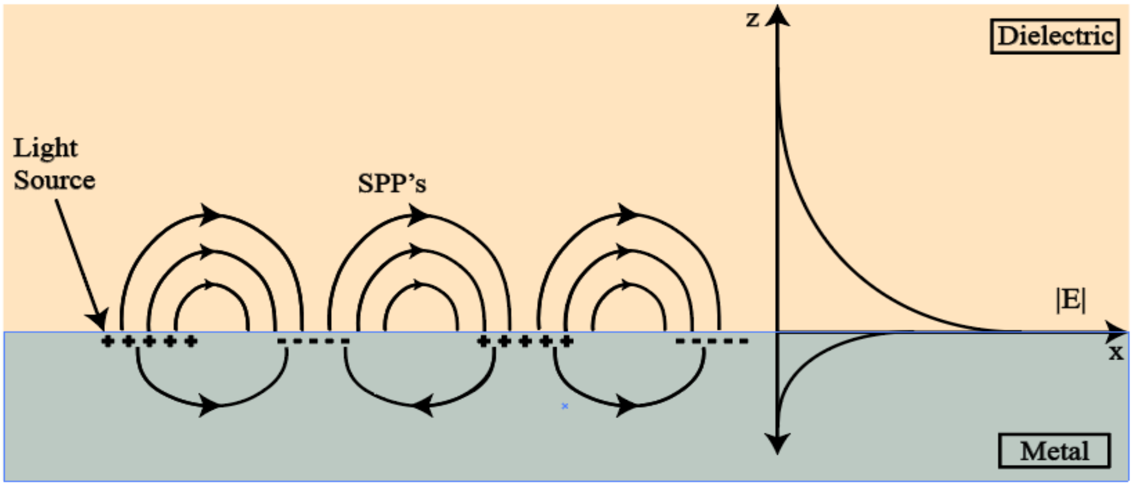

Figure 1.1: Formation and propagation of Surface Plasmon Polaritons (SPPs).

SPPs are electromagnetic waves that result from the interaction of photons and oscillating electrons along a metal-dielectric surface, as seen in figure 1.1 [2]. These waves enhance light-metal interactions by efficiently coupling light to the interface. Consequently, they surpass the diffraction limit, enabling the nanoscale miniaturization of photonic circuits and the generation of a significant localized EM field [3]. In addition, SPPs are transverse-magnetic waves that decay exponentially in the direction perpendicular to the interface. The dispersion relation of the wave vector SPP_{kx}, where the x-axis is the propagation direction and the z-axis is perpendicular to the interface, is written as [4]

$$k_x = k_0 \times \sqrt{\varepsilon_d . \varepsilon_m \big/ \varepsilon_d + \varepsilon_m} \qquad (1.1)$$

where, $k_0 = \frac{\omega}{c}$ represents the wave vector in free space in this equation. The exponential decay characteristic of SPPs is extremely sensitive to environmental variations. This unique property has enabled the development of numerous SPP-based devices, including splitters, couplers, filters, and sensors [5, 6].

1.2 Surface Plasmon Resonance

In surface plasmon resonance (SPR), incident light photons excite electrons in a metal's surface layer, causing the electrons to propagate in a direction parallel to the metal's surface. Figure 1.2 illustrates the SPR phenomenon. SPR depends on the refractive index of the material near to the metal surface when the wavelength of the light source is constant and the metal surface is thin [7]. As a result, the SPR phenomenon can be disrupted by even a little shift in the refractive index of the sensing medium, allowing for the detection of analytes. SPR assays enable label-free, real-time detection by identifying analytes by measuring changes in reflected light intensity or resonance angle. Various types of SPR biosensors for detecting clinically relevant biomarkers have been developed over time, and the efficacy of SPR biosensors has been improved using various nanomaterials.

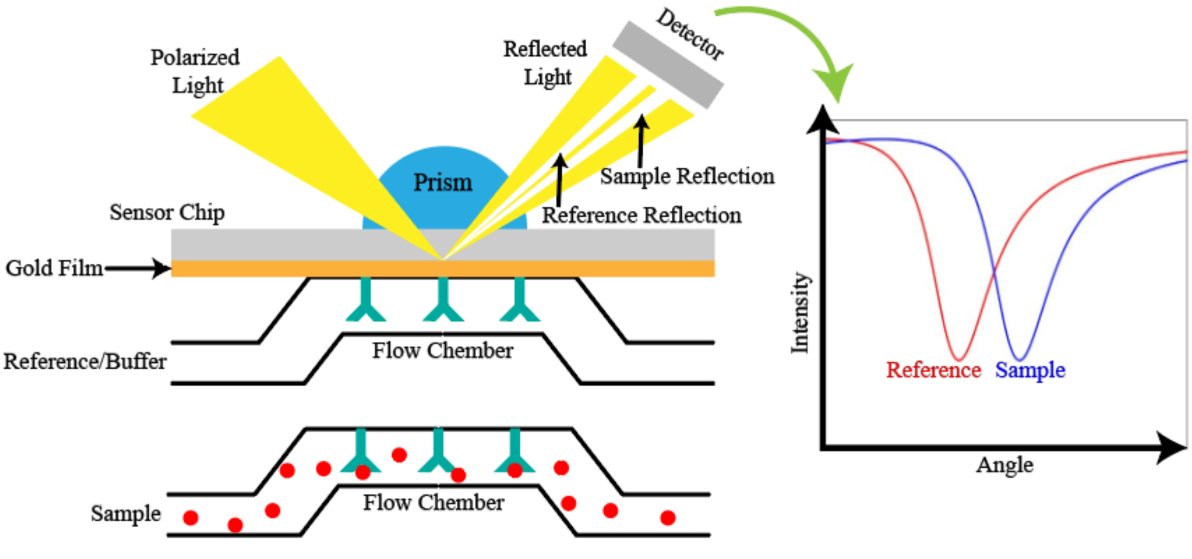

Figure 1.2: Surface Plasmon Resonance

1.3 Refractive Index Sensors

As RI is a significant parameter that reflects the intrinsic properties of materials, RI sensors have widespread use in disciplines, including petroleum, chemical, biological, food, pharmaceutical, and environmental monitoring. Multiple methods for detecting RI have been described in scientific literature.

I. **Surface plasmon polaritons (SPPs) in sensors** constitute one approach [8]. SPR-based sensor relies on the sensitivity of the SPR wavelength to dielectric environment surrounding the metal structure, frequently measure the wavelength shift of the resonance peak or dip caused by variations in RI and employ a figure of merit to evaluate the sensing performance. However, this detection procedure presents some obstacles. Since the SPR wavelength is extremely dependent on the RI of the surrounding dielectric, a broad range of analyte RIs can result in substantial shifts in the SPR spectrum [9]. This necessitates an extensive traversing range for optical detectors, which may restrict the adaptability of RI sensors.

II. The development of **optical-based wireless sensors** is another approach, although their accuracy is not yet satisfactory. For severe chemical environments and high temperatures, microsensors based on SiC and Si_3N_4 have been developed, but their complex fabrication process makes them expensive [10]. Due to their compatibility with on-chip integration, silicon photonics-based devices have also garnered considerable interest. In silicon photonics, refractive index sensors employ directional couplers [11], coupled slot waveguides [12], and micro-ring resonators [13].

1.3.1 PCF based SPR Sensors

Compared to other fiber-based sensors, PCF-based sensors offer increased sensitivity and lower resonance peaks, resulting in enhanced accuracy for detecting unknown analytes. In addition, the structural parameters of PCF can be varied to exert a greater degree of control over the transient field. For obtaining desirable sensing characteristics, the SPR technique is preferred. When SPR-based technology is combined with PCF's inherent characteristics, SPR-based PCF sensors develop [14]. Light contacts with the fiber that excites free electrons on the plasmonic metal surface, resulting in surface plasmon waves (SPWs) that travel through the sensor's core and cladding. When the real component of the effective refractive index is the same for both the SPP mode and the core mode, they couple together under a phase-matching condition at a specific wavelength. This circumstance creates a sharper resonance peak at a given wavelength, which is highly sensitive to the refractive index of the analyte. Consequently, even small variations in the refractive index cause the resonance wavelength (RW) to shift upwards or downwards. Consequently, unknown analytes can be identified by monitoring the RW fluctuations of various analyte refractive indices. Initially, prism-based and D-shaped sensors were utilized frequently in SPR-based sensors, but as technology advanced, PCF sensors became the preferred option. PCF-SPR sensors have undergone extensive development depending on whether the plasmonic metal layer and the analyte channel are positioned outside or inside the fiber.

1.3.2 Waveguide based Sensors

The metal-insulator-metal (MIM) plasmonic waveguide (WG) structure is extensively utilized for integrated optical circuitry. In Figure 1.3, the MIM WG is composed of two metal claddings surrounding an insulator. Key characteristics include fabrication simplicity and the capacity of confinement of light at subwavelength scales [15]. Changing the medium's refractive index even slightly alters the effective index of the propagating mode. The insulator-metal-insulator (IMI) WG is a notable plasmonic WG structure [16] that consists of metal layers sandwiched between insulator claddings. Propagation losses are reduced in IMI WGs compared to MIM WGs, allowing them to transmit near-infrared optical power greater than 10 µm. When the criterion is met, they can support a transverse magnetic mode analogous to dielectric mode. In the past two decades, numerical simulations have been performed on MIM plasmonic WG devices for a variety of applications, such as temperature sensing [17], refractive index sensing [18], pressure sensing [19], filtering [20], and biochemical sensing [21]. The fact that refractive index sensors can monitor solution concentration, pH levels, and other biological and chemical parameters has attracted considerable research interest. These sensors facilitate accurate detection and analysis by stimulating the sensing element.

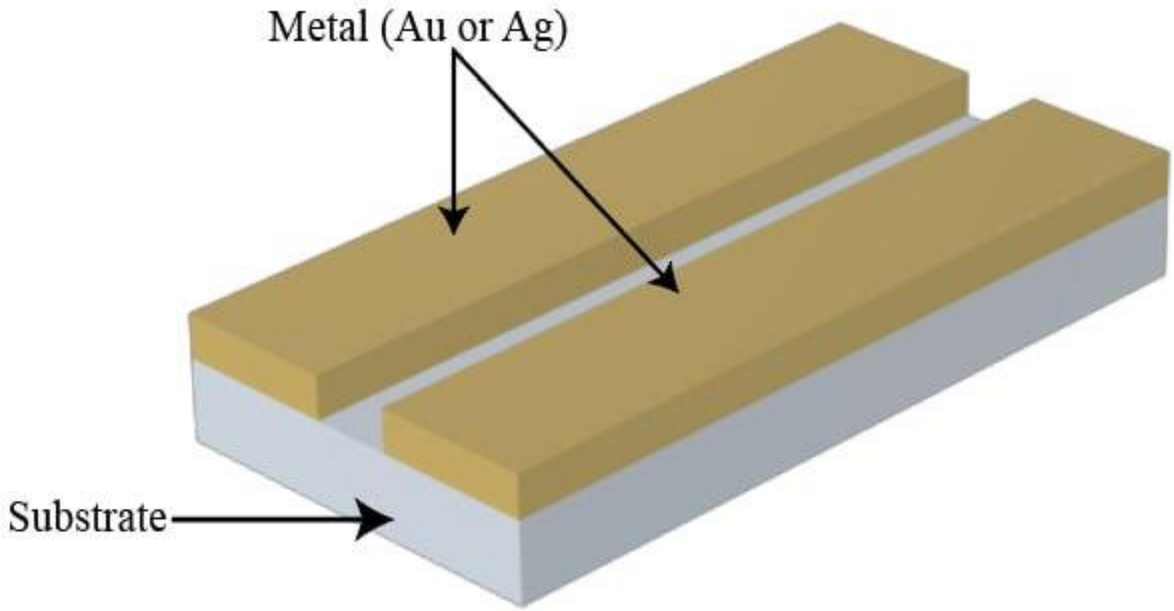

Figure 1.3: 3D schematic of a MIM waveguide structure.

1.4 Literature Review

Currently, it is impossible to overstate the importance of achieving high speed and miniaturization in devices. To achieve high speeds, the strategy involves decreasing device size and increasing carrier mobility. In addition, the diminution of capacitance and interconnection is a consequence of the diminution of device dimensions. However, quantum effects and the difficulty of non-uniform scaling impose certain restrictions. In the last two decades, the field of optics and photonics has undergone a remarkable revolution, resulting in the emergence of numerous industries specializing in optical instrumentation and fiber optic communication [22]. Sensing technology, particularly in the realms of ring resonator-based sensing and PCF-based SPR sensing, is a second area of research that has attracted considerable interest. These research advancements are being actively applied to practical sensing applications. Moreover, ring resonators have shown intriguing potential for extensive applications, such as optical filters, switches, modulators, routing, delay lines, and detectors [23].

Numerous plasmonic sensors utilizing the properties of SPPs have been published over time. In the study by Zhao et al. [24], a refractive index (RI) sensor based on MIM architecture with Fabry-Perot and a sensitivity of 718 nm/RIU (nanometers per refractive index unit) was presented. Another study [25] demonstrated a sensitivity of 986 nm/RIU using a MIM WG structure. Using a baffle and a cross-shaped cavity, Yang et al. [26] created a RI sensor with a sensitivity of 1100 nm/RIU. Similarly, a MIM structure with dual concentric double square-resonators had a sensitivity of 1380 nm/RIU [27]. The reported sensitivity for a hexagonal cavity coupled to a bus WG was 1562,5 nm/RIU [28]. Moreover, a T-shaped MIM structure-based RI sensor achieved 680 nm/RIU sensitivity [29].

Zhang et al. [30] developed a MIM WG coupled with two stubs and a ring resonator, with a sensitivity of 1268 nm/RIU. The sensitivity of a plasmonic square ring resonator was reported to be 1 367 nm/RIU in a separate study [31]. Su et al. exhibited a MIM waveguide coupled with an elliptical ring cavity with a sensitivity of 1550 nm/RIU [32]. In addition, the combination of an umbrella resonator and a metal baffle produced a sensitivity of 1600 nm/RIU [33]. Diest and his coworkers inserted two slits into the waveguide to enable the differentiation of three colors: red, green, and blue [34]. Butt et al. [35] reported the use of six unequal square cavities to filter white light into six distinct colors with a sensitivity of 700 nm/RIU. Zhang et al. [36] presented a 4-mode color filter with elliptical shaped resonator that had the maximum sensitivity at 608 nm/RIU and a FOM of 105.02.

SPR is an advanced label-free optical sensing technology, widely employed in biosensors [37]. Surface plasmons are generated when an evanescent field travels through the surface of a plasmonic metal and a dielectric medium in response to an electrical excitation. When the frequencies of the free electrons and the incident light photon coincide, a resonance condition happens at a certain resonant wavelength, resulting in observation of a sharp loss peak. Changes in the RI of the analyte cause variations in the resonant wavelength, allowing for the detection and measurement of the analyte. Novel designs such as Hollow Core PCF (HC-PCF) [38], dual-core structures [39], and twin core PCF (TC-PCF) [40] have been utilized to enhance the sensing ablities of SPR. These inventive designs serve as efficient platforms for biosensing applications.

Using SPR-PCF, a novel sensor that can simultaneously measure temperature and magnetic fields has been developed. It includes two elliptical channels on the core fiber [41]. PCF-based SPR biosensors are suitable for RI-based biosensing through various optical parameters. PCFs have desirable characteristics including design flexibility, scalability, efficient birefringence [42], controllable dispersion properties [43], and a variety of nonlinear effects [42]. These characteristics make it possible to tailor PCFs to specific sensing requirements. This has led to an increase in research into SPR-based biosensing applications [44].

PCF SPR imaging technologies overcome the limitations, such as their cumbersome design, need for precise incident angles, and the presence of numerous mechanical components that can be adjusted. The application potential of conventional SPR sensing techniques has been hampered by these limitations [45]. Even a slight change in the RI caused by an unidentified analyte can shift the loss peak. Resonance occurs when the wavelength of the incident photons is exactly equal to the wavelength of the surface electrons. SPP interacts with the surrounding medium at the resonance frequency [46]. This SPP mode is extraordinarily sensitive to even the smallest changes in the RI of the analyte [47]. PCF-based SPR sensors have numerous applications, i.e, DNA detection [48], gas sensing [49], water sample monitoring [50], and early cancer detection [51]. While SPR technology can be implemented using various configurations, such as prism-based setups [52] and Mach-Zehnder interferometers [53], it faces challenges related to optomechanics, including complex and bulky systems. By employing PCF-based biosensors, these limitations can be circumvented. The selection of plasmonic materials is crucial to the design and development of PCF-SPR sensors. Due to their unique properties, plasmonic materials such as silver [54], zinc oxide [55], gold [56], titanium dioxide [57], and graphene [58] are utilized to fabricate SPR biosensors.

1.5 Thesis Objectives

The objectives of the thesis:

- Introducing innovative plasmonic refractive index sensors.
- Exploring various plasmonic material combinations.
- Optimizing structural parameters in order to boost sensitivity.
- Conducting a thorough analysis of the existing research on surface plasmon resonance (S PR) sensors and polarization filters.
- Evaluating the efficacy of our designs by employing wavelength/amplitude interrogation techniques and assessing filter crosstalk.
- Investigating the applicability of the proposed sensors in biological applications, specifically for detecting biochemical components.
- Integrating external plasmonic materials to improve detection capabilities and overall performance.
- Presenting our design proposal with the most effective outcomes.

1.6 Thesis Layout

Chapter 1 presents a concise discussion of Surface Plasmon Polaritons (SPPs) and their importance in nanotechnology. Devices based on SPPs, and different waveguide schemes are elaborately discussed. A literature review on refractive index sensors to date and the thesis layout are also conferred.

Chapter 2 includes Maxwell's equations and generalized constitutive relations. The chapter also discusses the features of different EM wave solving algorithms, for example, FDTD, FIT, and FEM. The chapter concludes with the theoretical analysis of boundary conditions and fundamental mode.

Chapter 3 establishes the relationship between complex refractive index and complex relative permittivity. Notable plasmonic materials are designed using the Lorentz-Drude model. The chapter ends with the performance comparison of those materials.

Chapter 4 details the theories of different refractive index sensors, for example, ring resonator, and PCF based SPR sensors. Various performance indicators of RI sensors, such as sensitivity, FOM, Q-factor, and detection limit are defined.

Chapter 5 displays our first research work on a plasmonic RI sensor along with their fabrication technique. Extensive simulation and optimization are performed to capitalize on the performance of the sensors. The sensitivity achieved is higher than all previous research so far of our knowledge. The sensors are then deployed in various applications, for example, biosensing, water sensing, and filtering.

Chapter 6 displays another work of ours which is symmetrical array based SPR-PCF sensor with multiple peaks. Various fiber design parameters bimetallic layer thickness, and air hole diameters have been optimized to improve the sensitivity of the sensor. A novel sensing parameter, named Peak Amplitude Difference Sensitivity for multiple peaks has been proposed.

Chapter 7 illustrates yet another of our designs of a PCF based SPR sensor for wideband double peak sensing. Extensive simulations are performed to identify the performance of the sensors. The sensors have been fine-tuned to obtain the highest wavelength sensitivity which is the highest sensitivity achieved from previous research.

Chapter 8 concludes by summarizing and comparing all the findings with recent works. Future approaches for potential improvement are also mentioned.

Chapter 2

Wave Theory

2.1 Maxwell’s and Wave Equations

2.1.1 Maxwell’s Equations

Maxwell’s equations are a set of differential or integral mathematical expressions that depict the fundamental relationships between electromagnetic quantities. Maxwell's equations must be solved in order to conduct electromagnetic analysis. To employ the Finite Element Method (FEM) for this purpose, the equations are typically expressed in differential form. Maxwell's equations for time-varying electromagnetic fields can be written as follows:

$$\nabla \times H = J + \frac{\partial D}{\partial t} \tag{2.1}$$

$$\nabla \times E = -\frac{\partial B}{\partial t} \tag{2.2}$$

$$\nabla . D = \rho \tag{2.3}$$

$$\nabla . B = 0 \tag{2.4}$$

where,

E = Electric field intensity,

D = Electric flux density,

H = Magnetic field intensity,

B = Magnetic flux density,

J = Current density,

ρ = Electric charge density.

These equations are commonly referred to in their electric and magnetic formulations as Maxwell-Ampere's Law, Faraday's Law, and Gauss's Law. These are the fundamental principles that govern electromagnetic waves. Another essential equation in the study of electromagnetic waves is the continuity equation, which is written as follows:

$$\nabla . J = -\frac{\partial \rho}{\partial t} \tag{2.5}$$

2.1.2 Constitutive Equation

The characteristics of a medium within a closed system can be effectively described by constitutive equations, which can be written as follows:

$$D = \varepsilon_0 E + P \tag{2.6}$$

$$B = \mu_0 (H + M) \tag{2.7}$$

$$J = \sigma E \tag{2.8}$$

where, ε0, μ0, and σ denote the permittivity of vacuum, the permeability of vacuum, and the electric conductivity, respectively. ε0 and μ0 have the following values,

where ε_0 represents the permittivity of air, μ_0 represents the permeability of air, and σ represents the electrical conductivity. The exact values of ε_0 and μ_0 are as follows:

$$\mu_0 = 4\pi \times 10^{-7} H / m \tag{2.9}$$

$$\varepsilon_0 = \frac{1}{c_0^2 \mu_0^2} = 8.854 \times 10^{-12} F / m \tag{2.10}$$

where c_0 is the velocity of electromagnetic wave in a vacuum, which is the same as the velocity of light. Moreover, the electric polarization vector P describes the polarization of a material subjected to an electric field E. Polarization P is directly proportional to the electric field E in linear materials.

$$P = \varepsilon_0 \chi_e E \tag{2.11}$$

here, χ_e represents the electric susceptibility.

Similarly, the magnetization vector M describes the magnetization of a material in response to a magnetic field H. Magnetization M is directly proportional to magnetic field H in linear materials,

$$M = \mu_0 \chi_m H \tag{2.12}$$

here, χ_m represents the electric susceptibility.

So, from eq. (2.6) and eq. (2.7),

$$D = \varepsilon_0 (1 + \chi_e) E = \varepsilon_0 \varepsilon_r E = \varepsilon E \tag{2.13}$$

$$B = \mu_0 (1 + \chi_m) H = \mu_0 \mu_r H = \mu H \tag{2.14}$$

where,

$$\varepsilon_r = (1 + \chi_e) \tag{2.15}$$

$$\mu_r = (1 + \chi_m) \tag{2.16}$$

2.1.3 Generalized Constitutive Equations

Certain materials can display non-zero polarization in the absence of an electric field. In more general circumstances, the constitutive equations for these nonlinear materials can be expressed as follows:

$$D = \varepsilon_0 \varepsilon_r E + D_r \tag{2.17}$$

Certain materials can possess a non-zero electric flux density, known as the remanent electric flux density (D_r), in the absence of an electric field. Similarly, certain materials can exhibit a non-zero magnetization when there is no magnetic field present. The constitutive equations for these nonlinear materials can be formulated as follows in more general situations:

$$B = \mu_0 \mu_r H + B_r \tag{2.18}$$

Certain materials can have a non-zero magnetic flux density known as the remanent magnetic flux density (B_r) in the absence of a magnetic field. To account for the effects of an externally generated current, it is possible to generalize the current density expressed in equation (2.8) by adding an externally generated current J^e to the constitutive equation. This connection can be stated as follows:

$$J = \sigma E + J^e \tag{2.19}$$

2.1.4 Wave Equation

The wave equation describes the propagation of electromagnetic (EM) waves and serves as a fundamental governing equation. The derivation of the wave equation for the electric component of an EM wave from Maxwell's equations is shown. Multiplying (2.2) by the gradient operator (∇) yields the following expression:

$$\nabla \times (\nabla \times E) = \nabla \times (-\frac{\partial B}{\partial t}) = -\frac{\partial}{\partial t}(\nabla \times B) \tag{2.20}$$

From the equation 2.1,2.13 and 2.14,

$$\nabla \times (\nabla \times E) = -\mu\varepsilon \frac{\partial^2 E}{\partial t^2} \tag{2.21}$$

Considering $\frac{\partial}{\partial t} = j\omega, \varepsilon = \varepsilon_0 \varepsilon_r$ and $\mu = \mu_0 \mu_r$, this equation will be

$$\nabla \times (\mu_r^{-1} \nabla \times E) - k_0^2 \varepsilon_r E = 0 \tag{2.22}$$

Now, using the relation $\varepsilon_r = \eta^2$ for the linear materials where η is the refractive index and assuming $\mu_r = 1$, the equation can be re-written as,

$$\nabla \times (\nabla \times E) - k_0^2 \eta^2 E = 0 \qquad (2.23)$$

2.2 Simulation Modeling

2.2.1 Finite-Difference Time Domain (FDTD)

The Yee Algorithm

For the solution of EM wave problems, the finite-difference time-domain (FDTD) employs the Yee algorithm. The essence of FDTD is the sequential update of the electric and magnetic field values from the computational grid, which allows the user to move around a magnetic field component with an electric field and vice versa. Such a scheme reduces the complexity of curl rotations in Maxwell's equations significantly. In addition, only the values of adjacent cells are required to update the corresponding equations, thereby facilitating parallelization. In conclusion, the fundamental two-step computation process of FDTD consists of:

- Updating the magnetic field components based on the electric field components of the previous iteration, and
- Updating the electric field components based on the magnetic field components. FDTD technique begins with equations (2.1) and (2.2).

The fields are vectors in three dimensions. Each equation can be expanded into three coupled scalar first-order differential equations with time and space domain derivatives. Now, the curl of equations (2.1) and (2.2) yields,

$$
\begin{aligned}
\frac{\partial H_x}{\partial t} &= \frac{1}{\mu}\times[\frac{\partial E_y}{\partial z}-\frac{\partial E_z}{\partial y}] \\
\frac{\partial H_y}{\partial t} &= \frac{1}{\mu}\times[\frac{\partial E_z}{\partial x}-\frac{\partial E_x}{\partial z}] \\
\frac{\partial H_z}{\partial t} &= \frac{1}{\mu}\times[\frac{\partial E_x}{\partial x}-\frac{\partial E_y}{\partial z}] \\
\frac{\partial E_x}{\partial t} &= \frac{1}{\varepsilon}\times[\frac{\partial H_z}{\partial y}-\frac{\partial H_y}{\partial z}] \\
\frac{\partial E_y}{\partial t} &= \frac{1}{\varepsilon}\times[\frac{\partial H_x}{\partial z}-\frac{\partial H_z}{\partial x}] \\
\frac{\partial E_z}{\partial t} &= \frac{1}{\varepsilon}\times[\frac{\partial H_y}{\partial x}-\frac{\partial H_x}{\partial y}]
\end{aligned}
\qquad (2.24)
$$

The scalar equations are subsequently transformed into difference equations. The generation of these difference equations requires space and time discretization. Yee introduced spatial discretization by arranging field components within a unit cell. The electric field components are located along the cell's perimeter, whereas the magnetic field components are located in the cell's interior. This configuration produces an electric field encompassed by four magnetic field components (see Figure 2.2).

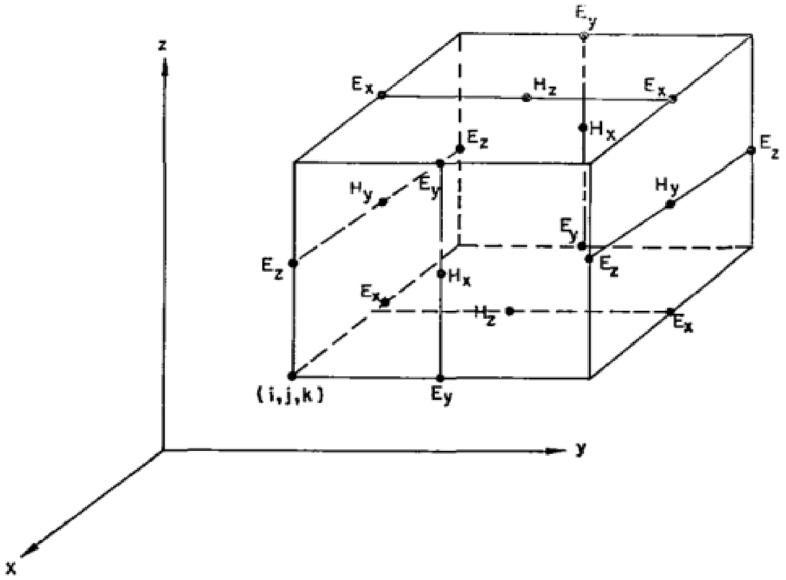

Figure 2.1: Yee’s spatial grid [59]

In terms of the TE$_z$ mode of propagation, the equations are as follows:

$$\begin{aligned}
\frac{\partial H_z}{\partial t} &= \frac{1}{\mu}\times[\frac{\partial E_x}{\partial y}-\frac{\partial E_y}{\partial x}] \\
\frac{\partial E_x}{\partial t} &= \frac{1}{\varepsilon}\times\frac{\partial H_z}{\partial y} \\
\frac{\partial E_y}{\partial t} &= -\frac{1}{\varepsilon}\times\frac{\partial H_z}{\partial x}
\end{aligned} \tag{2.26}$$

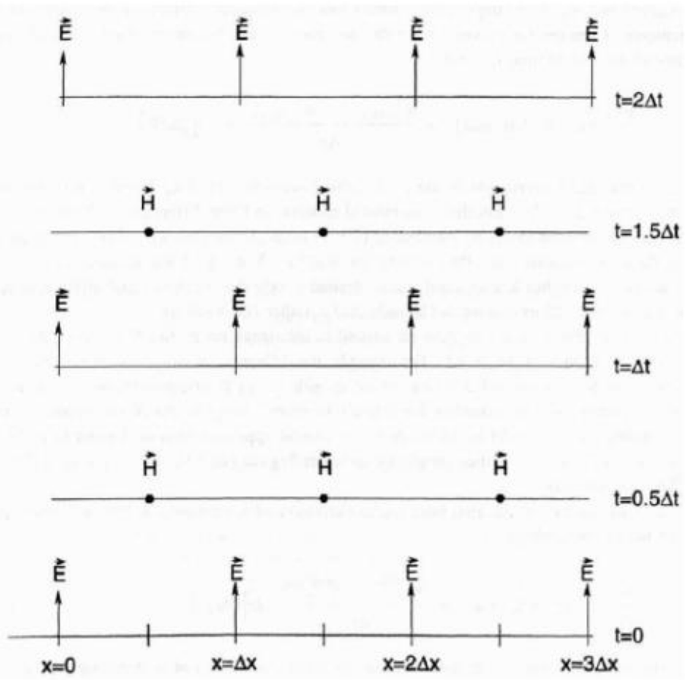

Figure 2.2: Temporal scheme of FDTD [60].

Now, applying the central difference theorem,

$$\begin{aligned}
&H_z(i+\frac{1}{2}, j+\frac{1}{2}, n+\frac{1}{2}) = H_z(i+\frac{1}{2}, j+\frac{1}{2}, n-\frac{1}{2}) + \frac{\Delta t}{\Delta y\mu}[E_x(i+\frac{1}{2}, j+1, n) \\
&-E_x(i+\frac{1}{2}, j, n)] - \frac{\Delta t}{\Delta x\mu}[E_y(i+1, j+\frac{1}{2}, n) - E_y(i, j\frac{1}{2}, n)]
\end{aligned} \tag{2.27}$$

$$E_x(i+\frac{1}{2}, j, n+1) = E_x(i+\frac{1}{2}, j, n) + \frac{\Delta t}{\Delta y\varepsilon}[H_z(i+\frac{1}{2}, j+\frac{1}{2}+1, n+\frac{1}{2}) - H_z(i+\frac{1}{2}, j-\frac{1}{2}+1, n+\frac{1}{2})] \tag{2.28}$$

$$E_y = (i, j+\frac{1}{2}, n+1) = E_y(i, j+\frac{1}{2}, n) - \frac{\Delta t}{\Delta x \varepsilon}\begin{bmatrix} H_z(i+\frac{1}{2}, j+\frac{1}{2}, n+\frac{1}{2}) \\ -H_z(i-\frac{1}{2}, j+\frac{1}{2}, n+\frac{1}{2}) \end{bmatrix} \tag{2.29}$$

The Yee algorithm must be stable during the numerical calculations; otherwise, the values of the electric and magnetic fields will increase exponentially and give erroneous results. The stability criterion is defined by the Courant–Friedrichs–Lewy condition:

$$\Delta t \le \frac{1}{c\sqrt{\left(1/\Delta x\right)^2 + \left(1/\Delta y\right)^2 + \left(1/\Delta z\right)^2}} \tag{2.30}$$

where, Δt = time step, Δx, Δy, Δz are spatial grid increments.

For 2D,

$$\Delta t \le \frac{1}{c\sqrt{\left(1/\Delta x\right)^2 + \left(1/\Delta y\right)^2}} \tag{2.31}$$

Let, Δx = Δy. Now,

$$\begin{gathered} \Delta t \le \frac{1}{c\sqrt{\left(1/\Delta x\right)^2 + \left(1/\Delta x\right)^2}} \\ \therefore \Delta t \simeq \frac{\Delta x}{\sqrt{2}c} \end{gathered} \tag{2.32}$$

Similarly, for 3D, let Δx = Δy = Δz. Now,

$$\begin{gathered} \Delta t \le \frac{1}{c\sqrt{\left(1/\Delta x\right)^2 + \left(1/\Delta x\right)^2 + \left(1/\Delta x\right)^2}} \\ \therefore \Delta t \simeq \frac{\Delta x}{\sqrt{3}c} \end{gathered} \tag{2.33}$$

Absorbing Boundary Condition (ABC)

Due to the limitation of computational power, in the FDTD simulations, a finite computational cell is simulated, which theoretically extends to infinity. The said boundary is an ideal absorber and guarantees zero reflection in interest, ensuring correct output. Such a mechanism can be done by padding the exits of the computational domain with artificial absorbing materials, for example, Berenger's perfectly matched layer (PML) [61]. PML attenuates the fields till their values are zero and ensures zero reflections.

2.2.2 Finite Integration Technique (FIT)

Weiland et al. [62] first introduced the concept of the finite integration technique (FIT). FIT deals with the integral forms of Maxwell's equations eq. (2.1) – eq. (2.4). Furthermore, the technique utilizes all the vector components of the E and H-field located in a double-grid system. Weiland [63] later reformed the FIT equations and arranged them in a matrix format, which enabled the use of irregular and non-orthogonal grids for computation. Furthermore, another advantage of FIT is the use of fewer computational memories than FDTD [64]. A one-dimensional staggered grid is proposed to formulate the computational domain of FIT. Let the grid has an interval of [0, K], where $0 = x_0 < x_1, ..., x_n = K$ is a finite sequence of n grid points. For a uniform 1D grid, let $x_i = i \times \frac{K}{n} . i = 0, ..., m$ is the uniform grid with a mesh size of $S = \frac{K}{n}$. Thus, the corresponding staggered grid is $s_i = (i - \frac{1}{2}) \times \frac{K}{n}, i = 1, ..., m$ (fig. 2.3).

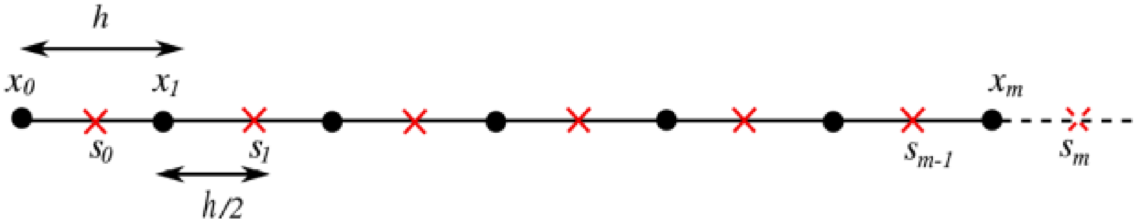

Figure 2.3: Uniform 1D grid.

Now, a set of corner points is defined as,

$$\xi_c := \{x_0, x_1, ..., x_n\} \tag{2.34}$$

Therefore, the corresponding staggered grid points are formulated as,

$$s_i = 0.5 \times \left(x_i + x_{i+1} \right), i = 0, \ldots, n-1, \tag{2.35}$$

denoting a grid increment of h/2. Therefore, the dual grid corresponding to ξ_c is,

$$\xi_s := \left\{ s_0, s_1, \ldots, s_n \right\} \tag{2.36}$$

For a 3D staggered grid, a rectangular domain of the following expression is considered:

$$\xi = \left[0, k_x \right] * \left[0, k_y \right] * \left[0, k_z \right] \tag{2.37}$$

Moreover, it is assumed that the 1D intervals [0, K_x], [0, K_y], and [0, K_z] are discretized by the following 1D grids,

$$\begin{aligned} \xi_c^x &:= \left\{ x_0, x_1, \ldots, x_n \right\} \\ \xi_c^y &:= \left\{ y_0, y_1, \ldots, y_n \right\} \\ \xi_c^z &:= \left\{ z_0, z_1, \ldots, z_n \right\} \end{aligned} \tag{2.38}$$

which are sets of grid points in x, y, and z-direction. Thus, eight possible grids can be formed utilizing these 1D grids, which are described as,

$$\xi_{t_x, t_y, t_z} = \xi_{t_x}^x * \xi_{t_y}^y * \xi_{t_z}^z \tag{2.39}$$

where, t_x, t_y, t_z = $\{c, s\}^3$, c refers to the corner points and s refers to the staggered points. The grids mentioned above are incorporated in the numerical analysis of FIT.

2.2.3 Finite Element Method (FEM)

Partial differentials equations (PDEs) are primarily used to describe the phenomena of fluid dynamics, electromagnetics, and thermal analysis. However, these phenomena involve inhomogeneous media and complicated geometry. Hence, the analytical solutions of the PDEs become complex. Such issues can be better handled by using the finite element method (FEM). The FEM can design EM wave problems with accurate material interfacing, accelerated convergence, adaptive meshing, and high numerical resolution than the conventional easier-to-code algorithms, for example, FDTD, Method of Moments (MoM). Pseudo-code of the FEM can be built for a particular field of interest and can be applied to other fields with little to no modification [65]. The four-step process to analyze any problem using the FEM are [66]:

- Discretizing the computational domain into a finite number of elements,
- Deriving the governing equations for a particular element,
- Assembling all the elements in the solution region, and
- Solving the formulated equations.

A generalized wave equation is

$$\nabla^2\varphi + k^2\varphi = g \tag{2.4}$$

where g represents the source, k represents the wavenumber, and φ is the unknown field potential. To simplify the problem, let $k = g = 0$. Thus, the Laplacian equation $\nabla^2\varphi = 0$ is satisfied, and the mechanism of FEM can be illustrated.

Discretizing the Computational Domain

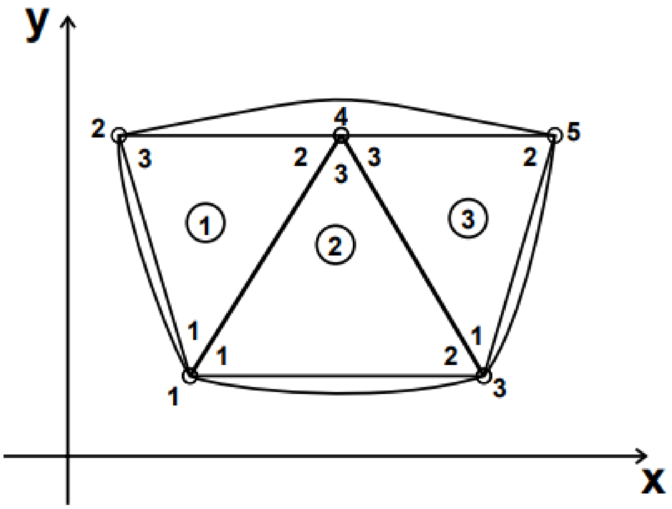

Figure 2.4: Finite Element Discretization

A 2D region with three triangular elements is taken to explain the step-by-step procedure of the FEM (fig. 2.4). The estimated solution of the computational domain can be written as,

$$V(x,y) \approx \sum_{m=1}^{L} V_m(x,y) \tag{2.41}$$

where, L = 3 signifies the total number of elements. The following polynomial function can be used to represent V_m considering triangular element,

$$V_m(x,y) = a + bx + cy \tag{2.42}$$

where, a, b, c are unknown constants to be ascertained. Equation (2.42) approximates a linear association of V_m within the element. Thus, the E-field is also assumed to be uniform considering an element,

$$E_m = -\nabla V_m \tag{2.43}$$

Governing Equations

Figure 2.5 depicts a single triangular element. The potential at different nodes is defined in the matrix form,

$$[V_m] = \begin{bmatrix} V_{m1} \\ V_{m2} \\ V_{m3} \end{bmatrix} = \begin{bmatrix} 1 & x_1 & y_1 \\ 1 & x_2 & y_2 \\ 1 & x_3 & y_3 \end{bmatrix} \begin{bmatrix} a \\ b \\ c \end{bmatrix} \tag{2.44}$$

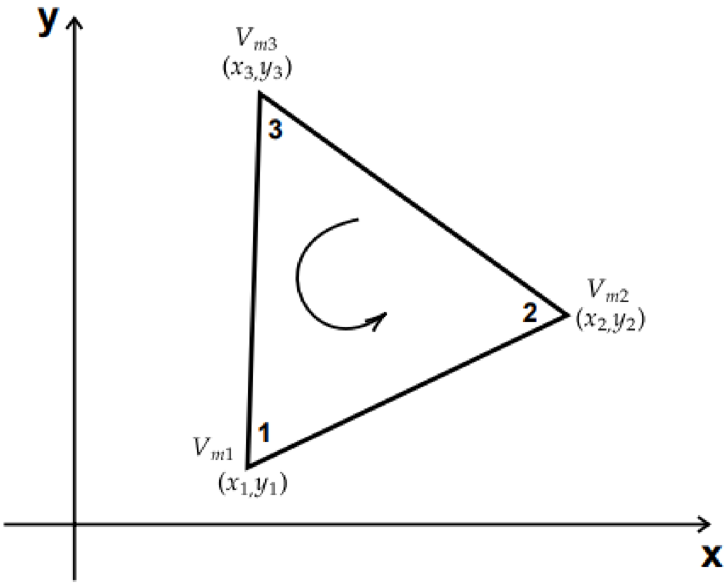

Figure 2.5: Single Triangular Element.

The unknown constants a, b and c can be determined as,

$$\begin{bmatrix} a \\ b \\ c \end{bmatrix} = \begin{bmatrix} 1 & x_1 & y_1 \\ 1 & x_2 & y_2 \\ 1 & x_3 & y_3 \end{bmatrix}^{-1} \begin{bmatrix} V_{m1} \\ V_{m2} \\ V_{m3} \end{bmatrix} \tag{2.45}$$

Plugging the values in eq. (2.42),

$$V_m = \sum_{m=1}^{3} \beta_m \left(x, y\right) V_{mi} \tag{2.46}$$

where,

$$\begin{aligned}
\beta_1 &= \frac{1}{2A}\times\left[\left(x_2y_3-x_3y_2\right)+\left(y_2-y_3\right)x+\left(x_3-x_2\right)y\right],\\
\beta_2 &= \frac{1}{2A}\times\left[\left(x_3y_1-x_1y_3\right)+\left(y_3-y_1\right)x+\left(x_1-x_3\right)y\right],\\
\beta_3 &= \frac{1}{2A}\times\left[\left(x_1y_2-x_2y_1\right)+\left(y_1-y_2\right)x+\left(x_2-x_1\right)y\right],\\
A &= \frac{1}{2}\times\left[\left(x_2-x_1\right)\left(y_3-y_1\right)-\left(x_3-x_1\right)\left(y_2-y_1\right)\right],
\end{aligned} \tag{2.47}$$

where, A is the element area, and beta is labeled as the element shape function. Furthermore, the energy per unit length related to the element m employing the Laplace equation is,

$$W_m = \frac{1}{2}\int \varepsilon\left|E_m\right|^2 dS = \frac{1}{2}\int \varepsilon\left|\nabla V_m\right|^2 dS, \tag{2.48}$$

where, from eq. (2.46),

$$\nabla V_m = \sum_{m=1}^{3} V_{mi}\nabla\beta_m \tag{2.49}$$

Plugging eq. (2.49) into eq. (2.48),

$$W_m = \frac{1}{2}\times\varepsilon\left[V_m\right]^t\left[C^{(m)}\right]\left[V_e\right], \tag{2.50}$$

where, t denotes the transposed form and,

$$\begin{aligned}
C_{ij}^{(m)} &= \int \nabla\beta_i.\nabla\beta_j dS,\\
\left[C^{(m)}\right] &= \begin{bmatrix} C_{11}^{(m)} & C_{12}^{(m)} & C_{13}^{(m)} \\ C_{21}^{(m)} & C_{22}^{(m)} & C_{23}^{(m)} \\ C_{31}^{(m)} & C_{32}^{(m)} & C_{33}^{(m)} \end{bmatrix}
\end{aligned} \tag{2.51}$$

where, $[C^{(m)}]$ refers to the element coefficient matrix.

Assembling of the Elements

Let, total L number of elements are assembled to form the complete solution region. The total energy of the assembled elements can be expressed as,

$$W_{total} = \sum_{m=1}^{L} W_m = \frac{1}{2}\varepsilon[V]^t[C][V] \tag{2.52}$$

Where,

$$[V] = \begin{bmatrix} V \\ V \\ \vdots \\ V_k \end{bmatrix} \tag{2.53}$$

where, k is the total nodes present in a single element. A 5×5 global coefficient considering the global numbering can be expressed as,

$$[C] = \begin{bmatrix} C_{11} & C_{12} & C_{13} & C_{14} & C_{15} \\ C_{21} & C_{22} & C_{23} & C_{24} & C_{25} \\ C_{31} & C_{32} & C_{33} & C_{34} & C_{35} \\ C_{41} & C_{42} & C_{43} & C_{44} & C_{45} \\ C_{51} & C_{52} & C_{53} & C_{54} & C_{55} \end{bmatrix} \tag{2.54}$$

Equation Solving

Minimum total energy ensures the satisfaction of the Laplace equation. Therefore,

$$\frac{\partial W}{\partial V_\phi} = 0, \phi = 1, 2, ..., k \tag{2.55}$$

Now, from eq. (2.52) and eq. (2.54),

$$\frac{\partial W}{\partial V_\phi} = 0 = V_1 C_{11} + V_2 C_{12} + V_3 C_{13} + V_4 C_{14} + V_5 C_{15} \tag{2.56}$$

Thus, the general expression is,

$$\frac{\partial W}{\partial V_\phi} = 0 = \sum_{m=1}^{k} V_m C_{mk} \tag{2.57}$$

Considering the 1st node as independent,

$$V_1 = -\frac{1}{C_{11}} \sum_{m=2}^{5} V_m C_{mk} \tag{2.58}$$

Therefore, the general form of expression is,

$$V_\phi = -\frac{1}{C_{\phi\phi}} \sum_{m=1, m\neq\phi}^{k} V_m C_{mk} \tag{2.59}$$

Scattering Boundary Condition (SBC)

SBC ensures a transparent simulation window for the incoming and outgoing/scattered waves. The scattered waves can be expressed as,

1. Plane scattered wave:

$$E = E_{sc} e^{-jk(n.r)} + E_0 e^{-jk(K.r)} \tag{2.60}$$

2. Cylindrical scattered wave:

$$E = \frac{E_{sc} e^{-jk(n.r)}}{\sqrt{r}} + E_0 e^{-jk(K.r)} \tag{2.61}$$

3. Spherical scattered wave:

$$E = \frac{E_{sc} e^{-jk(n.r)}}{r_s} + E_0 e^{-jk(K.r)} \tag{2.62}$$

Scattering Parameters

Scattering parameters (S-parameters) are complex quantities used to describe the different characteristics, for example, transmittance, reflectance, absorbance for an N-port EM device.

Defining voltage through the electric field is convenient in high-frequency operations. Furthermore, superposing the excited and reflected fields at the port generates the computed electric field, which can be expressed as,

$$E_{cm} = E_1 + \sum_{j=1} S_{j1} E_j \tag{2.63}$$

The other ports with no excitation can be expressed as,

$$E_{cm} = \sum_{j=1} S_{j1} E_j \tag{2.64}$$

Therefore, the S-parameters can be defined, considering various orthogonal modes, as,

$$\begin{aligned} S_{11} &= \frac{\int_{port1} \left(\left(E_{cm} - E_1 \right) . E_1 \right) dA_1}{\int_{port1} \left(\left(E_1 E_1^* \right) . E_1 \right) dA_1} \\ S_{21} &= \frac{\int_{port2} \left(\left(E_{cm} - E_2 \right) . E_2 \right) dA_2}{\int_{port2} \left(\left(E_2 E_2^* \right) . E_2 \right) dA_2} \\ S_{31} &= \frac{\int_{port3} \left(\left(E_{cm} - E_3 \right) . E_3 \right) dA_3}{\int_{port3} \left(\left(E_3 E_3^* \right) . E_3 \right) dA_3} \end{aligned} \tag{2.65}$$

and so on. Excitation of port two similarly generates S_{22} and S_{12}. Thus, S-parameters for an N-port device are formulated as,

$$S = \begin{bmatrix} S_{11} & S_{12} & \cdots & S_{1N} \\ S_{21} & S_{22} & \cdots & S_{2N} \\ \vdots & \vdots & \ddots & \vdots \\ S_{N1} & S_{N2} & \cdots & S_{NN} \end{bmatrix} \tag{2.66}$$

Transmittance can be defined as,

$$T = \left| S_{ij} \right|^2 \tag{2.67}$$

S-parameters for a two-port device carries the following meanings:

S_{11} = voltage reflection coefficient at the input port,

S_{21} = voltage transmission coefficient from port one to port two,

S_{12} = reverse voltage gain,

S_{22} = voltage reflection coefficient at the output port.

In decibels, S-parameters can be expressed as,

$$S_{ij}\left(dB\right)=20*\log_{10}\left(\left|S_{ij}\right|\right) \tag{2.68}$$

Port Analysis

Ports are boundary conditions deployed to indicate the input and output sides. S-parameters are associated with the port analysis. Let E_1, E_2, E_3 be the normalized fields. Thus, the power is equal in corresponding ports. Poynting vector defines this power flow and can be expressed as,

$$S_{avg}=\frac{1}{2}\mathrm{Re}\left(E\times H^{*}\right) \tag{2.69}$$

Moreover, the amount of power flowing out is defined by the normal component of the Poynting vector,

$$n.S_{avg}=n.\frac{1}{2}\mathrm{Re}\left(E\times H^{*}\right) \tag{2.70}$$

Mode Analysis

Mode analysis calculates the lowest fundamental mode that propagates within the waveguide and can solve the propagation constant. A complex parameter is present in the phase term of the time-harmonic representation of the E-field,

$$E\left(r,t\right)=\mathrm{Re}\left(\tilde{E}\left(r\right)e^{j\omega t-\gamma z}\right) \tag{2.71}$$

and

$$\gamma = \Psi_z + j\beta = -\lambda \tag{2.72}$$

where, Ψ_z is the damping along the propagating direction and β is the propagation constant.

Chapter 3

Plasmonic Materials

3.1 Refractive Index and Complex Permittivity

Researchers investigate multiple aspects of plasmonic materials on a regular basis. Plasmonic materials are distinguished predominantly by their complex dielectric function, which consists of permittivity and permeability. Considering that metals have a negligible effect on the magnetic field, the permeability () is typically assumed to equal one. Consequently, the complex permittivity of a plasmonic material can be depicted mathematically as

$$\varepsilon(\omega)=\varepsilon_1(\omega)-i\varepsilon_2(\omega) \tag{3.1}$$

Where $\varepsilon_1(\omega)$ represents the real part of $\varepsilon(\omega)$, which is related to polarization. A negative $\varepsilon_1(\omega)$ indicates that the plasmonic character is stronger. $\varepsilon_2(\omega)$ is the imaginary component of $\varepsilon(\omega)$, which accounts for the propagation loss of SPPs. An increasing value of $\varepsilon_2(\omega)$ indicates a system with higher losses, which represents the complex RI. We can write it as,

$$\eta=\eta_1-i\kappa \tag{3.2}$$

where, η = refractive index, and κ = extinction coefficient. Moreover, refractive index and permittivity are interrelated. Thus,

$$\begin{gathered}\eta_1=\frac{1}{\sqrt{2}}\times\sqrt{(\sqrt{\varepsilon_1^2+\varepsilon_2^2})+\varepsilon_1)}\\ \kappa=\frac{1}{\sqrt{2}}\times\sqrt{(\sqrt{\varepsilon_1^2+\varepsilon_2^2})-\varepsilon_1)}\end{gathered} \tag{3.3}$$

3.2 Material Modeling

In 1998, Rakic et al. conducted experiments on eleven candidate plasmonic materials and calculated the values required to match the parameters of two widely used models for material characterization in the high optical frequency range:

the Drude model and

the Lorentz-Drude model [67].

3.2.1 Drude Model

Numerous investigations have shown that the complex permittivity equation is predominantly influenced by two factors: intraband effects, also known as free-electron effects, and interband effects, also known as bound-electron effects. The intraband effects can be defined using the Drude model in the following form:

$$\varepsilon_{free}(\omega) = 1 - \omega_p^2 \Big/ (\omega^2 - i\omega\Gamma_0) \tag{3.4}$$

where, ω_p and Γ_0 refer to plasma and collision frequency, respectively.

3.2.2 Lorentz Model

Similarly, the Lorentz model expresses inter-band effects the following way,

$$\varepsilon_{bound}(\omega) = \sum_{i=1}^{m} \frac{\gamma_i \omega_i^2}{(\omega_i^2 - \omega^2 + i\omega\Gamma_i)} \tag{3.5}$$

where, ω_i, γ_i, and Γ_i are the resonant frequency, oscillator strength and damping frequency.

3.2.3 Lorentz-Drude Model

Summation of eq. (3.4) and eq. (3.5), therefore, constitutes eq. (3.6), the Lorentz Drude Model

$$\varepsilon(\omega) = \varepsilon_{free}(\omega) + \varepsilon_{bound}(\omega) \tag{3.6}$$

3.3 Characterization of Materials

3.3.1 Silica (SiO_2)

Applying a layer of plasmonic metal to the surface of a photonic crystal fiber (PCF) is a typical method for constructing SPR-based sensors. The PCF can be composed of a variety of materials, including polymers and glassware. As the substrate material for the PCF, Fused Silica, also known as silicon dioxide, is the material of choice. Generally, an undoped form of silica is employed. Several advantageous characteristics distinguish silica from other glasses and polymers [68].

- **Chemical Stability:** Silica possesses exceptional chemical stability and lacks hygroscopic properties.

- **Optical Transparency:** Silica possesses excellent optical transparency across a broad spectrum of wavelengths.

- **Mechanical Strength:** Silica possesses exceptional mechanical strength, which makes it resistant to tugging and bending.

- **Minimal Losses:** Silica has minimal scattering and absorption losses, approximately 0.2 dB/km, particularly in the near-infrared spectral region.

- **High-Temperature Compatibility:** Silica can be drawn into fibers at high temperatures, allowing for its use in processes involving fiber fabrication.

- **Fusion Splicing:** Silica exhibits outstanding performance in fusion splicing, enabling reliable and efficient fiber connections.

- **High Damage Threshold:** Due to its high damage threshold, silica is resistant to laser-induced degradation. This characteristic is crucial during the amplification of brief pulses in fiber amplifiers.

These characteristics contribute to the superior performance and dependability of PCFs based on silica in a variety of applications. RI property of fused silica is derived from Sellmeier equation [69]:

$$n_{silica}(\lambda)=\sqrt{1+\frac{B_1\lambda^2}{\lambda^2-C_1}+\frac{B_2\lambda^2}{\lambda^2-C_2}+\frac{B_3\lambda^2}{\lambda^2-C_3}} \tag{3.7}$$

Here, n_{silica} denotes the refractive index of silica. The equation 3.7 is valid within the wavelength range of 0.22 m to 3.71 m [70]. Figure 3.1 depicts the relationship between the wavelength and the refractive index of silica.

Table 3.1 Sellmeier Constants

Constant	Value
B_1	0.69616300
B_2	0.407942600
B_3	0.89747940
C_1	0.00467914826 μm^2
C_2	0.0135120631 μm^2
C_3	97.9340025 μm^2

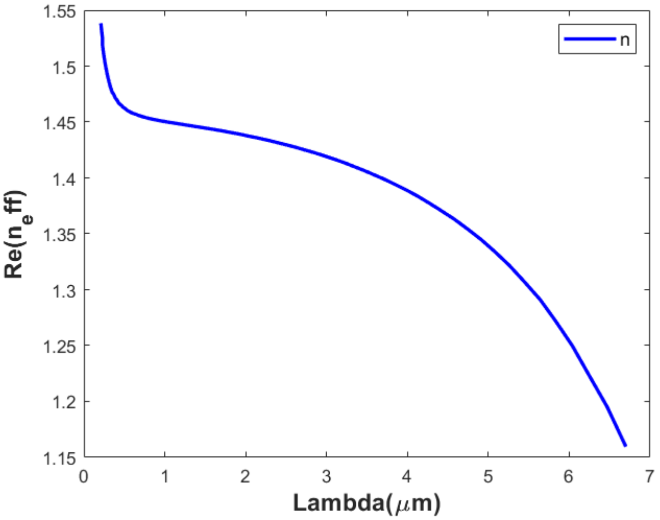

Figure 3.1: Silica RI in relation to light wavelength.

3.3.2 Air

Typically, the PCF's voids are filled with air. As wavelength varies, RI of air fluctuates minimally. However, these variations are negligible, as shown in Figure 3.2.

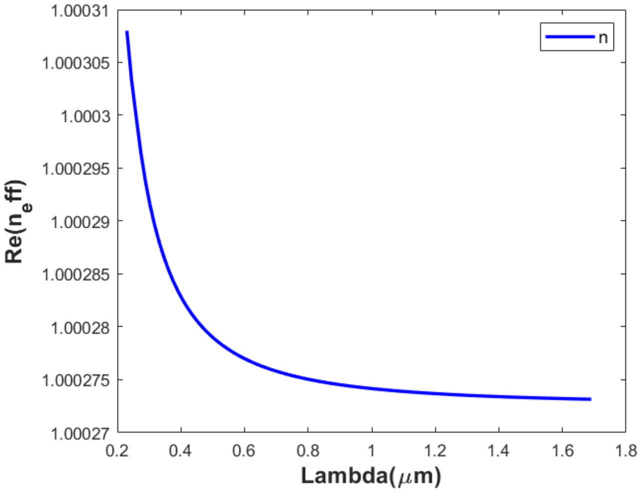

Figure 3.2: Air RI in relation to light wavelength.

The relation of air's RI and wavelength of light is depicted in Figure 3.2. Air's refractive index is always a real number with a value very near to 1. In all our research endeavors, we have therefore presumed that the refractive index of air is 1.

3.3.3 Gold

Gold is utilized as the outer layer material in SPR sensors for its advantages in comparison to other plasmonic materials. Gold is used extensively as plasmonic material due to the following advantages [71]:

- **Chemical Stability and Inertness:** Gold's chemical stability and inertness are exceptional.
- **Resistance to Oxidation:** It remains unoxidized in aqueous environments.
- **Sharp Resonant Peak:** Even in aqueous environments, gold exhibits a distinct resonant peak and a notable peak shift.

Using the Drude-Lorentz model, the dielectric constant of gold can be approximated using the following equation [72]:

$$\varepsilon_{Au} = \varepsilon_{\infty} - \frac{\omega_D^2}{\omega(\omega + j\gamma_D)} - \frac{\Delta\varepsilon\Omega_L^2}{(\omega^2 - \Omega_L^2) + j\Gamma_L\omega} \tag{3.8}$$

In this equation, ε_{Au} represents the permittivity of gold, ε_{∞} represents the high-frequency permittivity with a value of 5.9673. ω is the angular frequency, ω_D and γ_D are plasma and damping frequencies respectively, where $\omega_D = 4227.2\pi$ THz, $\gamma_D = 31.84\pi$ THz. Moreover, $\Delta\varepsilon$ = 1.09 is the weighting factor while the oscillator strength is $\Omega_L = 1300.14\pi$ THz, and spectral width is $\Gamma_L = 209.72\pi$ THz.

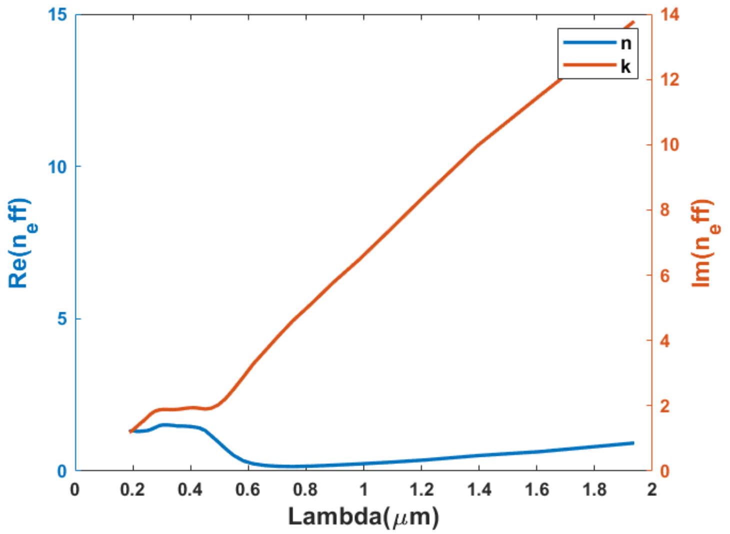

Figure 3.3: Gold RI in relation to light wavelength.

Equation 3.8 indicates that the dielectric constant of gold is a complex number corresponding to the squared value of its refractive index (RI). The RI of gold can be determined by taking the square root of the dielectric constant, which is also a complex value. Figure 3.3 depicts the real and complex components of the refractive index of gold as a function of wavelength.

3.3.4 Aluminium doped Zinc Oxide (AZO)

Being a suppliment plasmonic material to gold, aluminium-doped zinc oxide (AZO) with a 2% aluminum weight in ZnO is available. Despite its susceptibility to oxidation in humid environments, aluminum exhibits optimistic properties. As a plasmonic material, AZO is superior to gold in several ways. Notably, the presence of a thin gold layer causes islands to form. In addition, gold has a high plasma frequency that allows to operate in the UV or visible spectrum. In contrast, AZO, with its modest charge carrier density, possesses a near-IR plasma frequency. Due to the high penetration depth of the evanescent field in the near-infrared region, this property enables AZO-based SPR sensors to play a crucial role in biomedical sensing applications.

Additionally, the charge carrier density of AZO can be modified by adjusting the doping concentration, allowing for control over plasma frequency [73].

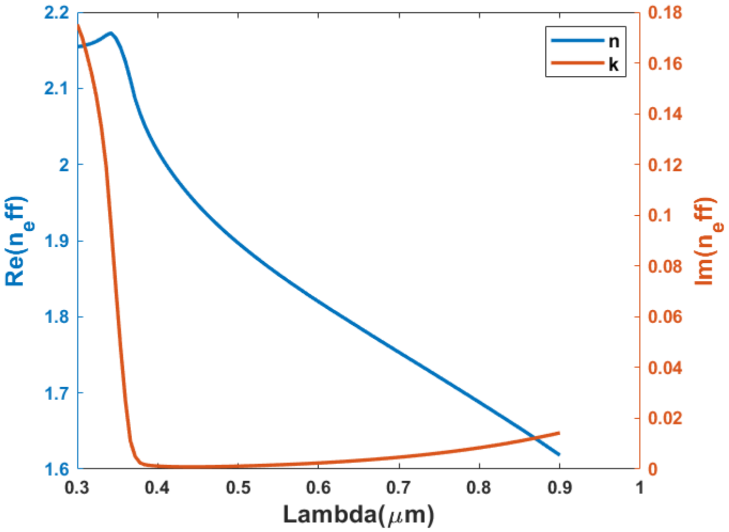

Figure 3.4: AZO RI in relation to light wavelength.

The dielectric characteristics of AZO (2% wt) can be expressed as [73]:

$$\varepsilon_{AZO}(\omega) = \varepsilon_b - \frac{\omega_p^2}{\omega(\omega + j\gamma_D)} - \frac{f_1\omega_1^2}{(\omega_1^2 - \omega^2 - j\omega\gamma_1)} \tag{3.9}$$

where ε_b is the polarization response of core electrons (background permittivity) and has a value of 3.5402 and ω_p is the plasma frequency having a magnitude of 1.7473 eV. The other parameters, γ_p, f_1, ω_1, and γ_1, have the corresponding values of 0.04486 eV, 0.5095, 4.2942 eV, and 0.1017 eV. Figure 3.4 shows the real and complex parts of the effective RI of AZO as a function of light wavelength.

3.3.5 Silver

Silver is utilized as the outer layer material in SPR sensors for better optical properties. Silver is utilized extensively as a plasmonic material due to the following advantages:

- **Enhanced Sensitivity:** Silver has excellent plasmonic characteristics in lower spectrum. This improves light coupling into PCF and sensor sensitivity.

- **Low Losses:** Silver has fewer optical losses than gold and other plasmonic materials. This feature boosts signal-to-noise ratios, improving detection limits and accuracy.
- **Broadband Response:** Silver's plasmonic response spans many wavelengths, making it suited for broadband sensing applications. This broad reaction detects multiple analytes or environmental changes across a wide spectrum of light.
- **Versatility:** PCF may be easily deposited with silver, simplifying production. Depending on sensor design and needs, it can be applied as a thin film or nanostructures.
- **Biocompatibility:** Silver is biocompatible for biomedical sensing. Due to its biocompatibility and low cytotoxicity, biosensors and medical devices employ it.

Silver plasmonic materials in PCF sensors offer sensitivity, low losses, wideband response, adaptability, and biocompatibility. These properties boost PCF sensor performance and usefulness in biological, environmental, and chemical sensing.

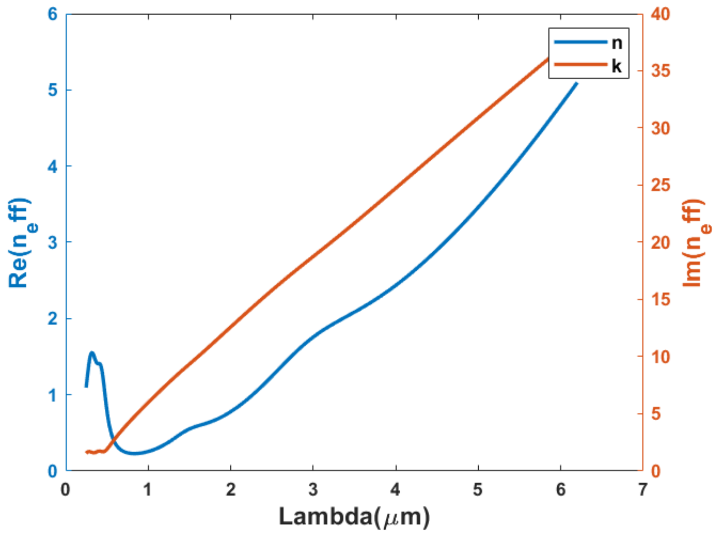

Figure 3.5: Ag RI in relation to light wavelength.

Using the Drude-Lorentz model, the dielectric constant of gold can be approximated using the following equation [74]:

$$\varepsilon_{Ag}(\omega) = 1 - \frac{\omega_p^2}{\omega(\omega - i\Gamma_0)} + \sum_{n=1}^{6} \frac{f_n \omega_n^2}{\omega_n^2 - \omega^2 + i\omega\Gamma_n} \tag{3.10}$$

where, ω_p and ω_n stand for plasma and resonant frequency, respectively, while Γ_0, Γ_n and f_n indicate damping constant, damping frequency, and oscillator strength, respectively. Figure 3.5 shows the real and complex parts of the effective RI of AZO as a function of light wavelength.

Chapter 4

Performance Metrics of an RI Sensor

4.1 NanoRing Resonator

A ring resonator is composed of a straight and loop waveguide. The loop can adopt various shapes (i.e., circle, oval, and racetrack). The nomenclature for most resonators is derived from the term "loop." Hence, a ring resonator is characterized by a coil in the shape of a ring [75]. Figure 4.1 illustrates the configuration of a ring resonator.

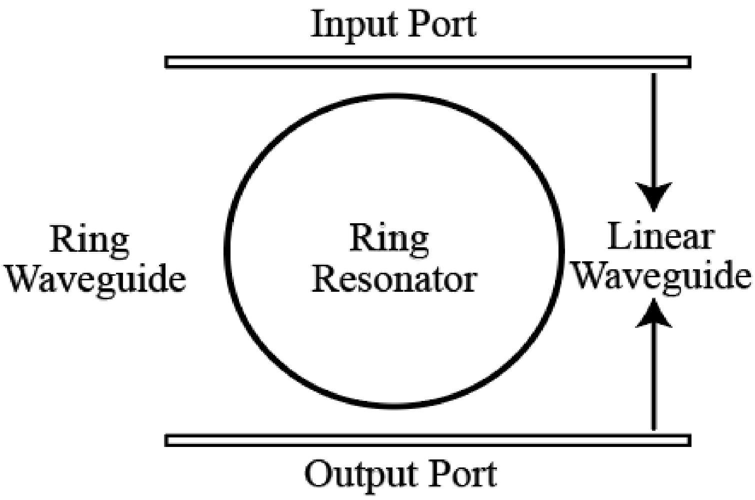

Figure 4.1: Ring Resonator.

The input signal traverses the input port and accumulates in the ring waveguide. This phenomena is driven by the resonance condition, prior to being directed to the output port. In the opposite direction, it is also possible to input a signal through the output port and have it added at the input port, thereby functioning as an add/drop multiplexer [75]. The applications of sensing will be the primary focus.

In sensing and detection applications, the optical ring resonator has come into extensive use. For high Q-factor, it can detect even small changes in RIs by frequency shifting. Whispering Gallery

Modes (WGM) form the foundation of the sensor's operating principle. Due to the resonance condition, as light travels through the input port, it accumulates inside the ring waveguide. The ring, typically composed of a material with a higher RI, such as silicon, couples with the light, whereas the surrounding medium, such as silica or a buffer, has a lower RI [76]. The analytes interact with the evanescent tails of the circulating light, changing the effective refractive index of the ring waveguide. This modification causes redshift of the resonator's resonance frequency, which enables the detection of particles or molecules via this frequency shift. Ring resonator-based sensing relies on this [77].

Not all the laser light that enters the bus waveguide couples to the ring waveguide via the coupler. Only specific wavelengths that satisfy the resonance condition, acting as divisors of the ring circumference, build up the ring waveguide. These frequencies are known as resonance frequencies. Resonance is defined as

$$m\lambda_{res} = 2\pi R n_{eff} \tag{4.1}$$

where m is an integer, λ_{res} is the resonance wavelength, n_{eff} is the effective refractive index, and R is the ring radius [77].

Compared to conventional fiber-based sensors, the ring resonator's effective interaction length makes it a more desirable sensor. Even though the interaction length of a fiber-based sensor is basically its physical length, the resonating light within the ring resonator in resonance mode increases the effective interaction length. In addition, it increases proportionally to the Q-factor value (ranging from 104 to 108). The mathematical expression for the ring resonator's effective interaction length is [78]

$$L_{eff} = \frac{Q\lambda}{2\pi n} \tag{4.2}$$

Consequently, the ring resonator's sensing performance is not dependent solely on its physical size. Its small footprint, ability to handle higher multiplexing levels with small analytes, and overall sensitivity make it an attractive sensor [78].

4.2 PCF based SPR Sensor

PCFs are optical fibers with an ordered air hole cladding surrounding a solid or hollow core [79].

4.2.1 Brief overview

In recent years, extensive research has been conducted on PCF sensors for applications such as medical imaging, telecommunications, healthcare, spectroscopy, chemical and biosensing, environmental monitoring, and drug testing [80]. PCFs can be classified according to their core design, namely solid core fibers and hollow core fibers, as seen in figure 4.2(a,b). Adjusting the lattice arrangement, pitch (distance between air holes), and size of the air holes to meet specific design and functional needs can produce a variety of structures. Solid core PCFs have a cladding with a lower index and a core with a higher effective index. In contrast, hollow core fibers have a core with a lower index than the cladding material, and confinement of light to the core is accomplished via scattering and interference, resulting in the generation of an evanescent field within the cladding.

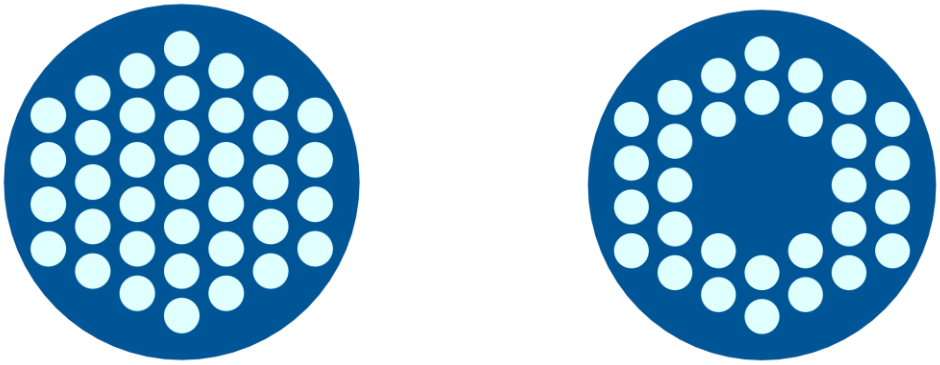

Figure 4.2: Cross-section of (a) solid and (b) hollow core PCF.

4.2.2 Guiding mechanisms

Since the core's refractive index is higher than the cladding, light is confined within the core and transmitted by total internal reflection in a conventional optical fiber. Depending on their structure, photonic crystal fibers (PCFs) exhibit two distinct light-guiding mechanisms. To preserve light within the core, solid-core PCFs use a form of total internal reflection that is similar to that used in conventional fibers. This is accomplished by constructing a solid silica core that has a greater refractive index than the cladding. A cladding filled with an array of air capillaries surrounds the core, lowering its refractive index. These fibers are also called as index guiding PCFs. Hollow core fibers, on the other hand, utilize the photonic band gap mechanism. The core of the fiber in this guiding mechanism contains air holes that lower its refractive index relative to the cladding. Consequently, light propagates due to the existence of a bandgap. It should be noted that only photons with a bandgap greater than that of the cladding region can propagate through the photonic crystal structure. These photons therefore remain evanescent in the cladding region, while the remaining photons travel through the core.

4.3 Performance Metrics of Ring Resonator

4.3.1 Sensitivity (S)

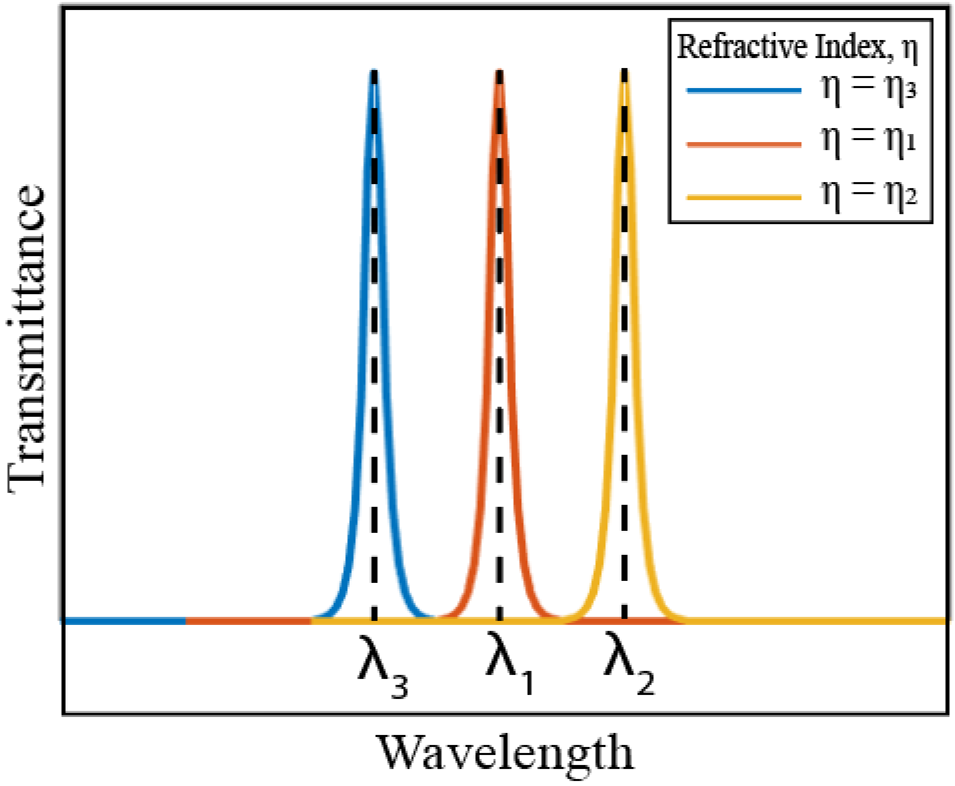

Figure 4.3: Sensitivity calculation.

Sensitivity is the most important performance metric for a RI (refractive index) sensor. Sensitivity (S) is determined by the change in the resonant wavelength and the corresponding change in the refractive index, can be expressed as [81]:

$$S = {}^{\Delta\lambda}\!/_{\Delta n} \tag{4.3}$$

where $\Delta\lambda$ represents the change in the resonant wavelength and Δn represents the change in the RI. Both redshifts and blueshifts are possible. Compared to the central blue curve, the pink curve in Figure 4.3 demonstrates a redshift, while the orange curve demonstrates a blueshift. Calculating the difference between the respective and values yields the sensitivity (S) value.

4.3.2 Figure of Merit (FOM)

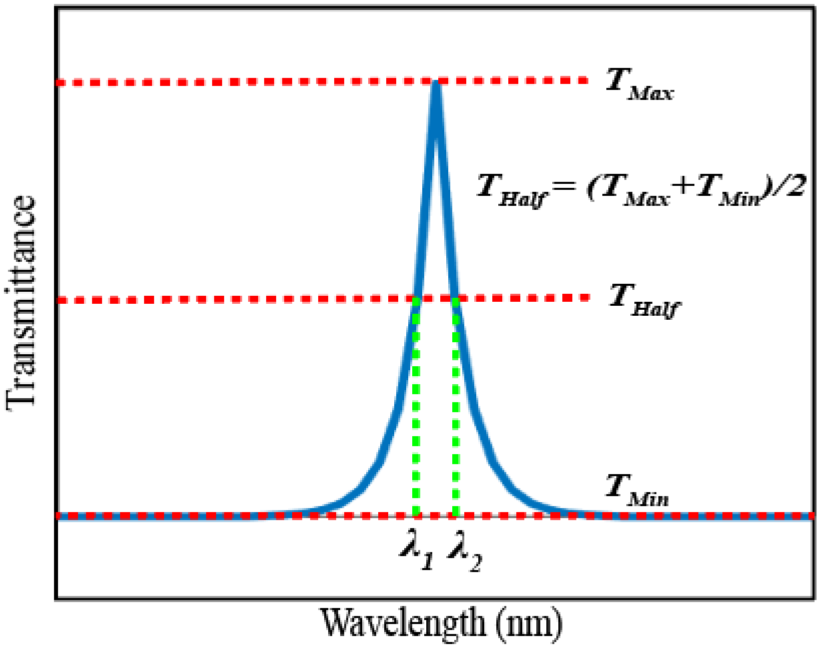

Figure 4.4: Figure of Merit calculation.

The figure of merit is a metric used to assess the efficiency of the RI sensor. A higher FOM/FOM* means that the sensor can easily detect resonant peaks. The formula for calculating FOM/FOM* is [82]:

$$FOM = {S}/{FWHM} \tag{4.13}$$

$$FOM^* = {\Delta T}/{T \Delta n} \tag{4.14}$$

Here, FWHM is the Full Width at Half Maximum. T represents the transmittance of the proposed sensor, whereas ΔT/Δn represents the change in transmittance (ΔT) at a particular wavelength owing to a change in RI (Δn). The FWHM can be calculated from Figure 4.4 by averaging the maximum and minimum transmittance values, denoted as T_{half}. T_{half} intersects the transmittance curve at λ_1 and λ_2 wavelengths. The FWHM is the difference between these two wavelengths.

4.3.3 Quality-factor (Q-factor)

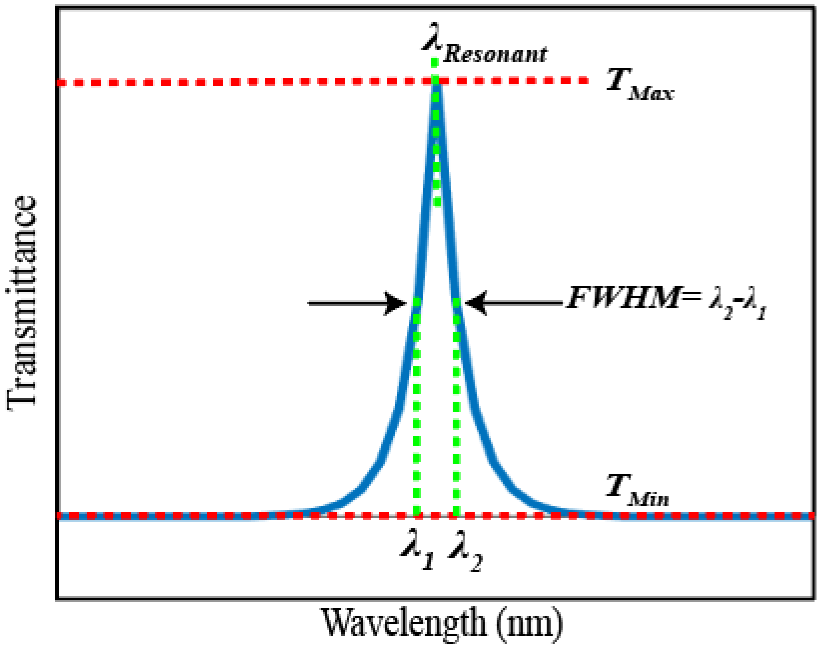

Figure 4.5: Q-factor calculation.

The quality factor (Q-factor) is a performance metric utilized in filtering applications that can be expressed as [83]:

$$Q = {\lambda_{resonant}}/{FWHM} \tag{4.15}$$

where $\lambda_{resonant}$ stands for the resonant wavelength.

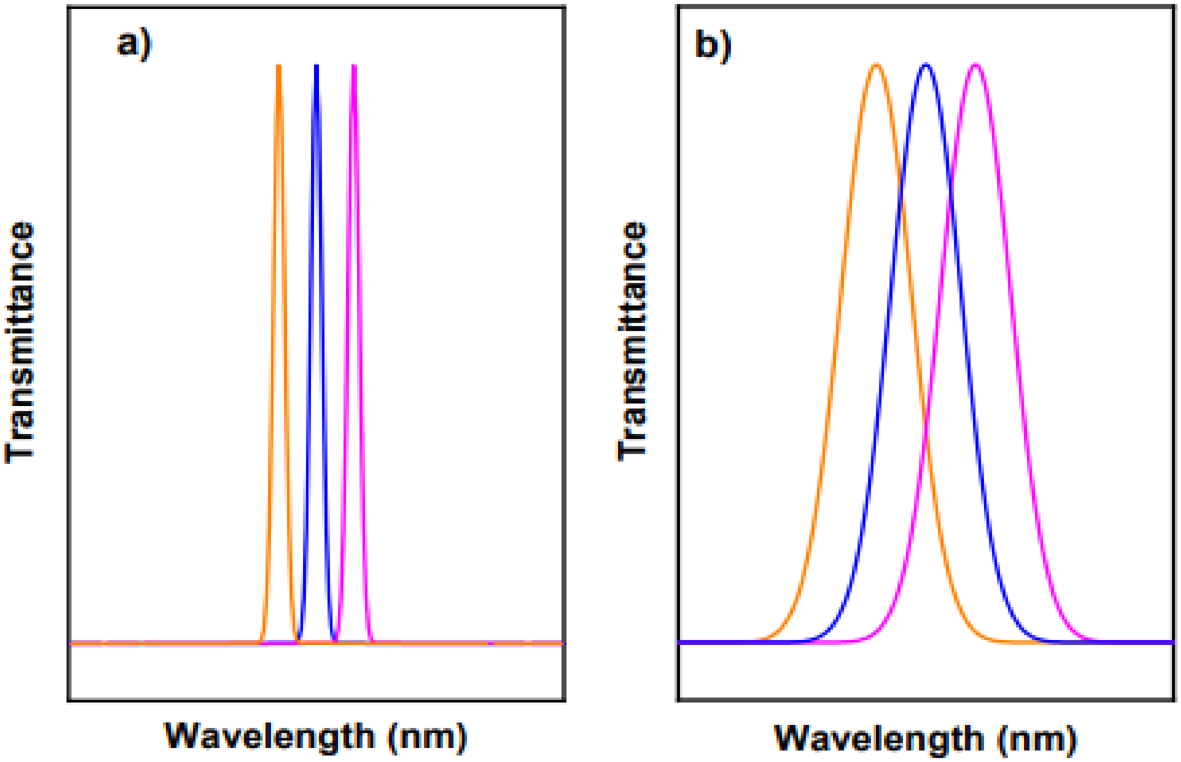

Figure 4.6: (a) High Q-factor and (b) low Q-factor representation.

Figure 4.6a illustrates a response with a sharp/high Q-factor, which makes it suitable for plasmonic filtering applications. Figure 4.6b, on the other hand, displays a low Q-factor response, indicating its ineffectiveness in filtering tasks.

4.3.4 Detection Limit (DL)

The detection limit is a crucial performance parameter for biosensors, representing the smallest change in refractive index that can be accurately detected in biosamples. The detection limit (DL) is calculated as follows [84]:

$$DL = {}^{\Delta\lambda_{\min}}\!\!/_{S} \tag{4.16}$$

Here, $\Delta\lambda_{min}$ = 0.001 nm represents the minimum resolution of a cutting-edge spectrum analyzer.

4.3.5 Dip Strength

Dip strength refers to the difference between the transmittance peak and dip, which can be written as [85]

$$\Delta D = (T_{peak} - T_{dip}) \times 100\% \tag{4.17}$$

4.4 Performance Metrics of PCF based SPR Sensor

4.4.1 Conventional PCF sensors' characteristics

4.4.1.1 Confinement loss (CL)

Confinement loss (CL) is a crucial performance metric for determining the efficiency of PCF sensors because it serves as the foundation for evaluating other metrics. It is the energy that is transmitted from the core mode to the SPP mode by means of modified total internal reflection (MTIR). Imperfections in PCF's structural design result in confinement losses, in which some of the light energy conveyed through the core of the PCF sensor escapes into the surrounding metallic layer. The CL quantifies the quantity of energy lost due to this leakage and can be calculated by [86]:

$$\alpha(dB/cm) = 8.686 \times \left(\frac{2\pi}{\lambda}\right) \times \mathrm{Im}\left(n_{eff}\right) \times 10^4 \tag{4.18}$$

where λ signifies the wavelength, and $\mathrm{Im}(n_{eff})$ represents the imaginary component of the effective mode index. The phase-matching condition is satisfied when the real component of the effective refractive index for the core mode and SPP mode becomes identical at the wavelength of resonance. The resultant confinement loss spectrum can be applied to advancement of PCF-SPR sensors and polarization filters.

4.4.1.2 Effective Material Loss (EML)

The effective material loss (EML) is an essential performance parameter in PCF that has a substantial effect on its sensing capabilities in the THz region. To quantify EML, the formula is:

$\alpha(\nu) = \nu^2 + 0.63\nu - 0.13(dB/cm)$ which establishes a linear relationship between frequency and material absorption loss [87]. This relationship demonstrates the significance of minimizing material absorption loss to enhance the waveguiding characteristics of the sensor.

4.4.1.3 Relative Sensitivity

PCF's relative sensitivity is crucial for determining its adaptability as a sensor. The following equation can be used to quantitatively evaluate it [88]:

$$r = \frac{n_r}{n_{eff}} \times P\% \tag{4.19}$$

where n_r is the analyte's refractive index and n_{eff} is the effective refractive index. The power fraction, denoted by P, is the ratio of the power of the air hole to the total power and is expressed as [89]:

$$P = \frac{\int_{sample} R_e(E_x H_y - E_y H_x)dxdy}{\int_{total} R_e(E_x H_y - E_y H_x)dxdy} \times 100 \tag{4.20}$$

E_x and E_y denote transverse electric fields, while H_x and H_y denote transverse magnetic fields for the fundamental guided mode.

4.4.1.4 Effective cross-sectional area (A_{eff})

The effective area gives a reliable estimate of the core area where light is confined, and electromagnetic waves propagate. Using the following mathematical method [89], precise measurement of the effective area can be accomplished:

$$A_{eff} = \frac{\left[\int I(r) r dr\right]^2}{\left[I^2(r) dr\right]^2} \qquad (4.21)$$

where the intensity distribution of the transverse electric field is $I(r) = |E(t)|^2$

4.4.1.5 Effective refractive index (n_{eff})

The effective refractive index is the ratio between the speed of light in air and medium, taking into account the polarization direction of the light propagating in the guiding structure. Using the following formula [90], one can calculate the effective refractive index of any material:

$$n_{effpm} = \frac{c}{v_{zpm}} = \frac{\beta_{pm}}{k_0} \qquad (4.22)$$

where β_{pm} is the propagation constant and $k_0 = \frac{\omega}{c} = \frac{2\pi v}{c} = \frac{2\pi}{\lambda_0}$ is the vacuum wave quantity. Here, v represents the frequency and λ_0 the wavelength.

4.4.1.6 Numerical Aperture

The numerical aperture (NA) quantifies the ability of a fiber to interact with light. In the case of a PCF sensor, a larger numerical aperture is preferable because it increases light confinement within the core. The numerical aperture can be calculated using the following equation, where c represents the velocity of light, f is the frequency, and A_{eff} is the effective area [89]:

$$NA = \frac{1}{\sqrt{1 + \frac{\pi A_{eff} f^2}{c^2}}} \qquad (4.23)$$

4.4.1.7 Dispersion

Dispersion is the spreading of light waves propagating through a fiber. There are two forms of dispersion: material and waveguide dispersion. Dispersion can be expressed as [91]:

$$\beta_2 = \frac{2}{c}\frac{dn_{eff}}{d\omega} + \frac{\omega}{c}\frac{d^2 n_{eff}}{d\omega^2} \tag{4.24}$$

where ω represents the angular frequency and the other parameters were previously defined.

4.4.2 SPR-PCF based sensors' characteristics

4.4.2.1 Amplitude Sensitivity

Interrogation techniques based on wavelength and amplitude are typically evaluate the potential of a sensor. Unidentified samples can be detected by measuring the variation in loss dip caused by changes in the RI of the analyte. Amplitude interrogation is a technique for detecting various analytes.

$$s_A = -\frac{1}{\alpha(\lambda, n_a)}\frac{\partial_a(\lambda, n_a)}{\partial n_a}(RIU^{-1}) \tag{4.25}$$

where $\alpha(\lambda, n_a)$ represents the confinement loss for a particular sample RI and $\partial_a(\lambda, n_a)$ represents the difference in analyte confinement loss between two adjacent refractive indices [92].

4.4.2.2 Wavelength Sensitivity

The wavelength interrogation, also known as spectral-based assessment, is an additional method for assessing the sensor's efficacy. It relies on observing the fluctuation in the wavelength of resonance and typically offers greater sensitivity than the previously mentioned method. This technique's (WI method) phase-detection procedure is cost-effective, but assessing its sensitivity presents challenges [93]. Wavelength sensitivity can be measured by:

$$s_\lambda = \frac{\Delta\lambda_{Peak}}{\Delta n_a}(nm / RIU) \tag{4.26}$$

where $\Delta\lambda_{Peak}$ denotes the difference between successive resonant wavelengths and Δn_a represents the difference in RIs [94].

4.4.2.3 Figure of Merit (FOM)

In addition to AS and WS, the figure of merit (FOM) is also employed to assess the sensor's performance. It is merely the ratio of WS to FWHM [92]. FWHM represents the width of the confinement loss curve at half and dictates the sharpness of the peak loss. A sensor with a more sharper loss peak possesses greater sensing efficacy. The equation for FOM is

$$FOM = \frac{S_\lambda}{FWHM}(RIU^{-1}) \tag{4.27}$$

4.4.2.4 Resolution

Resolution is a crucial factor to determine the detection accuracy of a sensor. It is the smallest detectable variation in RI. The resolution can be based on amplitude (R(A)), wavelength (R(W)) respectively. The resolution formulas are as follows [92]:

Amplitude resolution:

$$R(A) = \frac{\Delta n_a}{s_A}(RIU) \tag{4.28}$$

Resolution of wavelength:

$$R(\omega) = \frac{\Delta\lambda_{\min}}{s_\lambda}(RIU) \tag{4.29}$$

where $\Delta\lambda_{\min}$ represents the minimum wavelength resolution, all the terms used in these formulas have been previously discussed in antecedent sections.

4.4.2.5 Novel Peak Amplitude Difference Sensitivity

When multiple peaks are present, it is possible to establish a correlation between the amplitudes of different peaks at the same RI of the analyte. This correlation is utilized to define a specific interrogation known as Peak Amplitude Difference Sensitivity. Through the investigation of the variation in peak amplitudes among the multiple resonance wavelengths, a distinguishing parameter for the detection of analytes is identified. The calculation of this sensitivity is determined by an equation, which is presented below:

$$S_{PA-PA} = \frac{1}{(\alpha(\lambda_{p3}, n_b) - \alpha(\lambda_{p1}, n_b))} \frac{(\alpha(\lambda_{p3}, n_a) - \alpha(\lambda_{p1}, n_a)) - (\alpha(\lambda_{p3}, n_b) - \alpha(\lambda_{p1}, n_b))}{n_b - n_a} RIU^{-1} \quad (11)$$

Where S_{PA-PA} represents the PADS and $\alpha(\lambda_{p1}, n_a)$, and $\alpha(\lambda_{p3}, n_a)$ are the first and third loss peaks for refractive index n_a, $\alpha(\lambda_{p1}, n_b)$ and $\alpha(\lambda_{p3}, n_b)$ are the first and third loss peaks for refractive index n_b. Here a correlation is found between even and odd peaks. Utilizing multiple peak analysis represents a significant advance in attaining precise, label-free detection across a broad spectrum of wavelengths. This implies that by employing the distinctive parameters of the odd peaks for detection, even though the findings are almost the same for various RIs, the distinctive parameters of the even peaks can validate and further verify the findings. This provides a more convenient method for accurately detecting any analyte than sensors that rely on a single peak. For analyzing multiple peaks, determining unknown refractive indices using Amplitude Sensitivity (AS) alone may result in a misinterpretation for multiple maximum AS values for the same refractive index in various wavelength regions. When applied to mass detection techniques, WS may necessitate substantial spectral modifications, resulting in an increase in cost. To overcome this problems, we proposed a novel parameter known as PADS, which takes into account for minumum two distinct peaks. Similar to AS, PADS compares these values to a reference value and calculates the unknown refractive index, but with greater precision and accuracy.

Chapter 5

Modeling, Optimization and Numerical Analysis of the Proposed Nanoring Resonator

This section discusses the design, optimization, fabrication, and application of a refraction index sensor. The sensor is designed to provide plasmonic applications with very high sensitivity.

5.1 Sensor Design and Theoretical Analysis

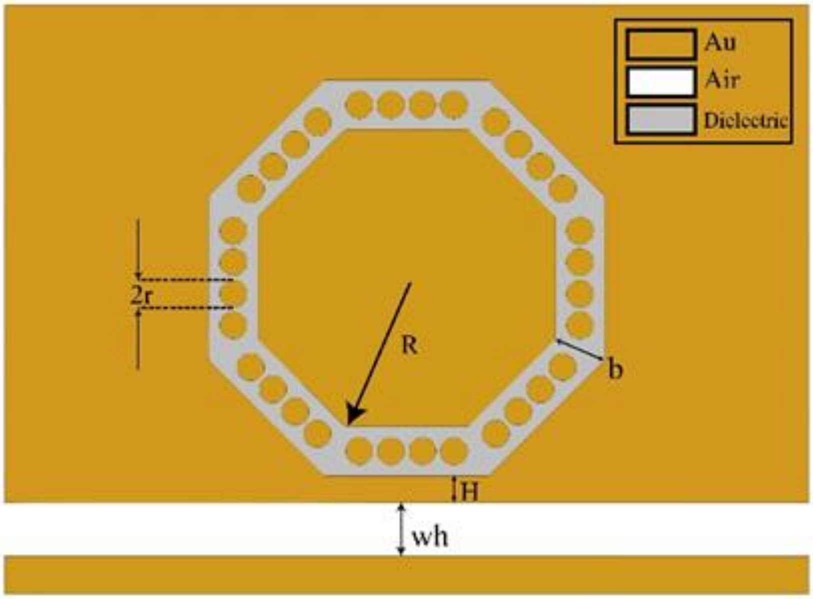

Figure 5.1: 2D model of the designed sensor.

Figure 1 depicts our proposed octagonal plasmonic nanosensor, where various colors represent various materials. Ashes, white, and gold colors represent dielectric, air, and gold, respectively. A bus waveguide and an octagonal ring resonator with 32 nanorods involve the design. The resonator contains a material with a particular refractive index, while air fills the bus waveguide and gold occupies the remaining spaces. The bus waveguide (width) and a laterally coupled nanoring (thickness b), produces a Metal-Insulator-Metal (MIM) structure. SPP's can go across the metal-dielectric junction because of presence of gap (H) between the ring and the bus waveguide. The interior octagon has radius R. For increasing wavelength sensitivity, nanorods are strategically positioned in regions with a strong electric field confinement. Before optimization, the important structural parameters are shown in Table 5.1.

Table 5.1: Preliminary 2D modeling parameters.

Parameters	Symbol	Values (nm)
Width of the waveguide	wh	80
Distance between outer and core radius of the octagonal resonator	b	50
Core radius of the octagonal resonator	R	350
Outer radius of the octagonal resonator	$R+b$	400
Radius of the nanorods	r	((2*sin(22.5/180*pi))*b)/3.5
Gap between the waveguide and the octagonal resonator	H	12

COMSOL Multiphysics is employed to simulate the structure. In frequency domain (ewfd) interface, 2-D FEM and the EM Waves are used to calculate the frequency domain transmission response. Subdomains of “extra fine” triangular meshes assured accuracy utilizing scattering boundary. A plane wave is used to activate the transverse magnetic (TM) mode of the MIM waveguide at its input port. The power transmittance was calculated by [95].

$$T = \frac{Output\ Power(P_o)}{Input\ Power(P_i)}$$

Since the width of the MIM waveguide is significantly less than the wavelength of the incoming wave, the Surface Plasmon Polaritons (SPPs) waves are primarily carried by the waveguide's fundamental transverse magnetic (TM) mode. The dispersion equation for the TM mode can be expressed as follows [96]

$$\varepsilon_d \sqrt{n_{ef}^2 - \varepsilon_d} + \varepsilon_m \sqrt{n_{ef}^2 - \varepsilon_d} \tanh\left(\frac{wh.\pi \sqrt{n_{ef}^2 - \varepsilon_d}}{\lambda} \right) = 0 \qquad (2)$$

Where ε_d represents the dielectric's permittivity, ε_m represents the metal's permittivity. n_{eff} denotes effective refractive index, wh represents the width of the bus waveguide, and represents the wavelength. The transmittance spectrum's resonant wavelength is affected by the effective refractive index of the nanosensor. The coupled-mode theory provides an explanation for this occurrence. Consequently, the resonant wavelength of the transmittance spectrum, denoted by λ_m, can be expressed as [97]

$$\lambda_m = \frac{\mathrm{Re}\left(n_{ef}\right).P_{ef}}{m - \left(\varphi / 2\pi\right)} \qquad (3)$$

where n_{ef} represents the effective refractive index, P_{ef} represents the effective route covered by the Surface Plasmon Polariton (SPP) in the resonator, m is a positive number, and φ represents the phase shift resulting from reflection on the air-metal interface.

5.2 Initial Results and Discussion

As shown in Equation (3), the resonance wavelength conditions (λ_m, P_{ef}, and n_{ef}) and sensor performance of the proposed plasmonic nanosensor are substantially influenced by the structural parameters (R, r, b, and N). The nanoring's core radius is set to R = 350 nm, and the distance between the octagonal resonator's outer and core radii is b = 50 nm. To facilitate fabrication, simulations take into account the maximum number of gold nanorods as N = 32 and $2r = 2 \times \frac{Difference\ between\ outer\ and\ inner\ length\ of\ octagonal\ resonator}{k}\ nm$, where k = 3.5. Figure 3(a-e) depicts a comparison of nanorods of gold with N = 0, 4, 8, 16, and 32. Initial selection for this investigation was a MIM bus waveguide with an 80 nm width and a 12 nm gap between the bus waveguide and the octagonal nanoring. As depicted in Figure 3(f), the investigation of transmittance spectra investigates the proposed plasmonic nanosensor with and without gold nanorods embedded in the octagonal nanoring.

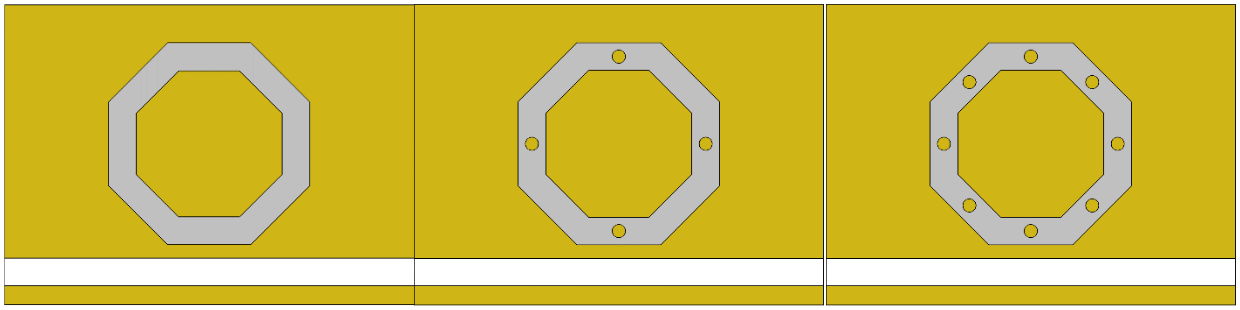

(a) (b) (c)

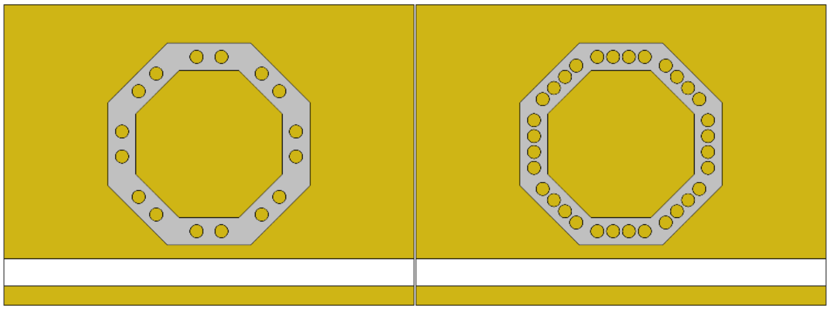

(d) (e)

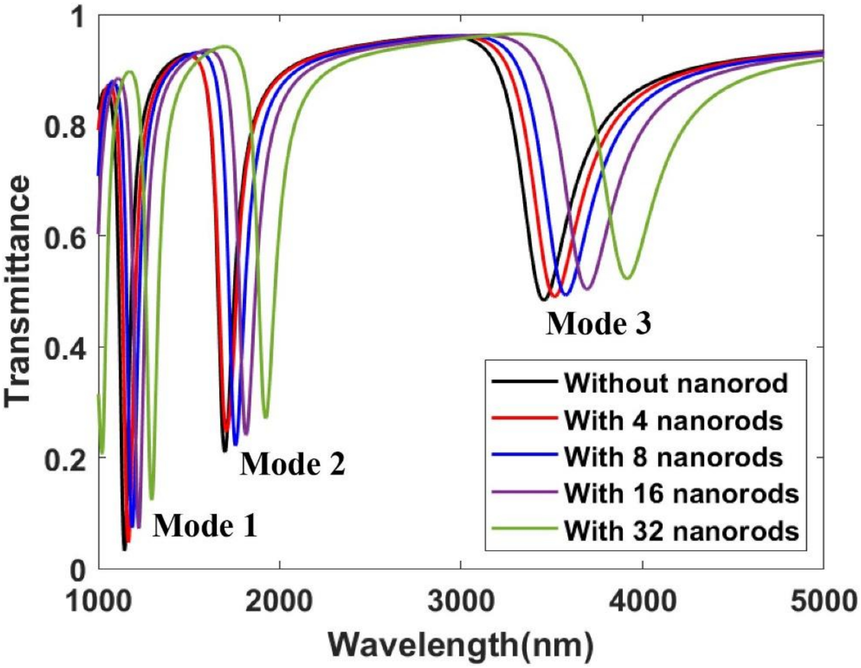

Transmittance
Wavelength(nm)
0
0.2
0.4
0.6
0.8
1
1000
2000
3000
4000
5000
Mode 1
Mode 2
Mode 3
Without nanorod
With 4 nanorods
With 8 nanorods
With 16 nanorods
With 32 nanorods

(f)

Figure 5.2: Illustration of the proposed sensor (a) without, (b) with 4, (c) with 8, (d) with 16, (e) with 32 nanorods and (f) The transmission spectra without (black color) and with gold nanorods (red, blue, purple, and olive colors).

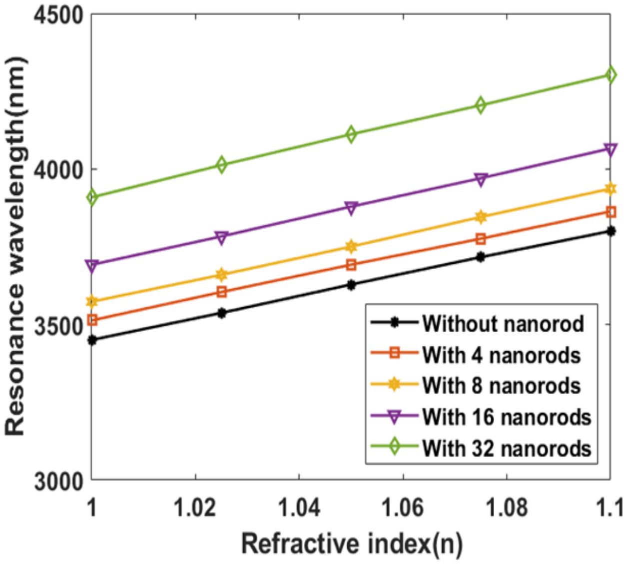

Figure 5.3: The estimated mode 3 resonance wavelength in the absence and presence of 4, 8, 16, and 32 gold nanorods with the variation of refractive index.

Figure 5.3 illustrates the correlation that has been computed between the refractive index of the octagonal ring resonator that has been proposed and the wavelength of resonance. The findings illustrate a direct correlation between refractive index and resonance wavelength in all instances examined, including those without gold nanorods and those with 4, 8, 16, and 32 nanorods.

To evaluate the sensor's performance and capabilities, S (sensitivity), FOM (figure of merit), Q factor, and dip amplitude (T) for modes 1-3 are shown in Figure 7. The sensitivity exhibits a linear increase as the number of nanorods increases, as shown in Figure 7. In the absence of gold nanorods, the refractive index sensitivity is 3628.4 nm/RIU. This sensitivity increases to 3648.4 nm/RIU when four gold nanorods are present, 3809.2 nm/RIU when eight gold nanorods are present, 3,828 nm/RIU when sixteen gold nanorods are present, and 4142.4 nm/RIU when 32 gold nanorods are present. The addition of gold nanorods to the nanoring multiplies sensitivity by 1.13 (or 13.4%). Higher sensitivity comes from higher resonant wavelength. So, mode 3 is the optimal choice for a higher sensitivity. In addition, mode 1 exhibits a higher FOM. Increasing the number of nanorods does not have a linear effect on the FOM, but by employing gold nanorods, the FOM can be adjusted to the desired position for mode 3. It also maintains a nearly constant Q factor, while modes 1 and 2 lack linearity. At last, the sensitivity is 4142.4 nm/RIU, dip strength is 0.757822 for mode 3. Also, an FOM of 16.89 and Q factor of 18.14 for mode 1 is acceptable.

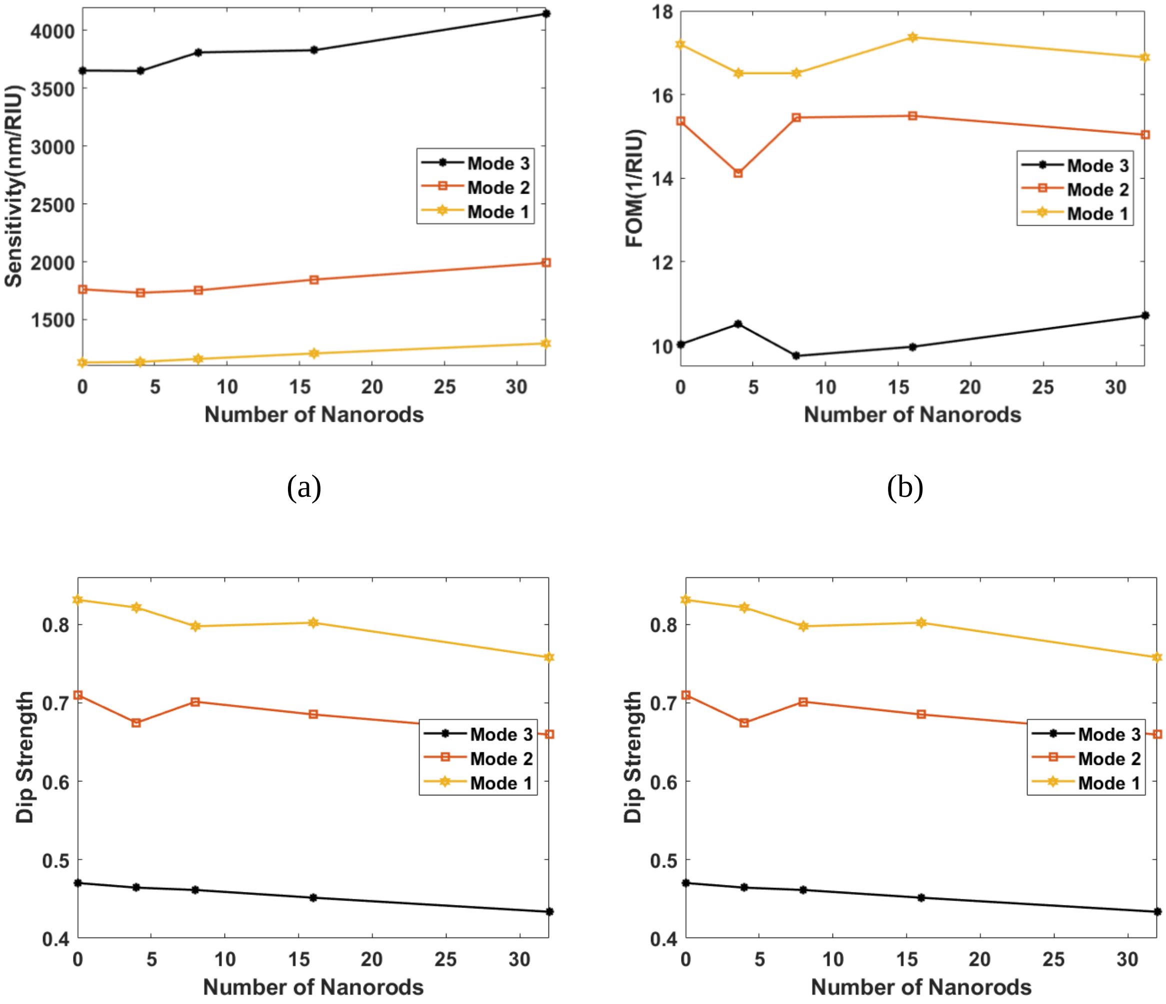

(a)

(b)

(c)

(d)

Figure 5.4: : (a) Sensitivity, (b) FOM, (c) Q factor, and (d) Dip Strength for 3 modes.

5.3 Optimization of Different Geometrical Parameters

5.3.1 Optimization of the Nanorods

To modify the resonant state of the nanoring, the radius of the gold nanorods (r) can be altered. In Figure 5.5, an increase in nanorod radius results in greater confinement and, consequently, a rise in the electric field's total energy. As a result, the resonance wavelength redshifts. Using an equation in which the radius is inversely proportional to the variable k and k is varied from 4 to 2.5 with a decrement of 0.5, the nanorod radius is calculated. The parameters wh = 80 nm, H = 12 nm, R = 350 nm, N = 32, and n = 1.0 are also considered. Notably, the transmittance apex displays a pronounced redshift. When the nanorod radius is between 9 and 15 nm, significant effects on transmittance dips are observed, and as the radius increases, the resonance wavelength undergoes a significant dispersion

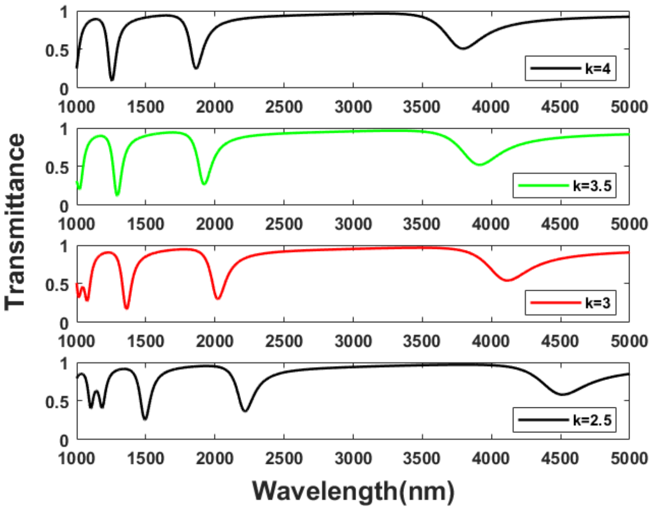

Figure 5.5: The transmittance spectrum of the proposed sensor with the variation of k from 4 to 2.5 with a decrement of 0.5.

5.3.2. Optimization of the Inner Radius

Core radius of the octagon is varied during the optimization process, while the remaining parameters remain unchanged. Figure 5.6 depicts the variation in transmission spectrum of an octagonal ring resonance as the core radius is modified while the outer radius remains unchanged as the core radius is altered. The resonant wavelength increases as the inner radius of the octagon increases. Our observations indicate that a core radius of 370 nm produces the most desirable results, which are characterized by a narrower decline and a longer resonant wavelength. Consequently, this results in highest sensitivity.

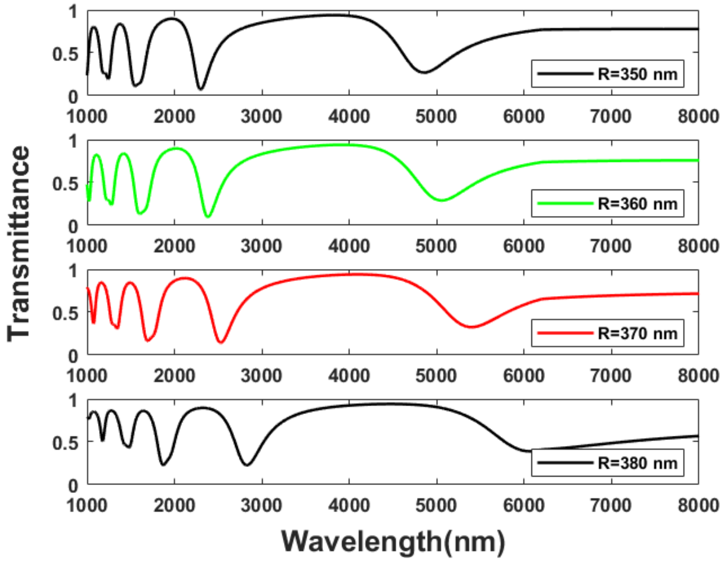

Figure 5.6: The transmittance spectrum of the proposed sensor with the variation of inner radius (R).

5.3.3. Optimization of the Coupling Length

Figure 5.7 illustrates transmittance of the proposed nanosensor in relation to coupling length. Adjusting the coupling length from 0 to 20 nm in increments of 5 nm. As the length increases, the dip goes up and the resonant wavelength blue shifts. Moreover, it influences n_{eff} of the localized SPP modes within the coupling region. Finally, 5 nm yields the most preferable results, characterized by a smaller dip and a longer resonant wavelength. Consequently, this results in a notable increase in sensitivity.

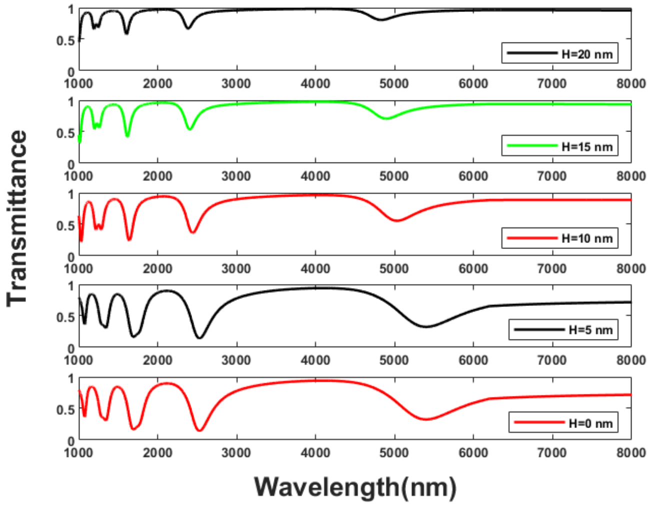

Figure 5.7: The transmittance spectrum of the proposed sensor with the variation of the coupling length (H).

5.4 Performance Evaluation

Table 3. Summary after optimization

Parameter	Value before Optimization	Sensitivity (nm/RIU) before Optimization	Dip Strength (ΔT) before Optimization	Value after Optimization	Sensitivity (nm/RIU) after Optimization	Dip Strength (ΔT) after Optimization
R	350 nm	4142.4	0.6759	370 nm	**13157**	**0.8311**
k	3.5			2.5		
H	12 nm			5 nm		
n	1.0			1.32		

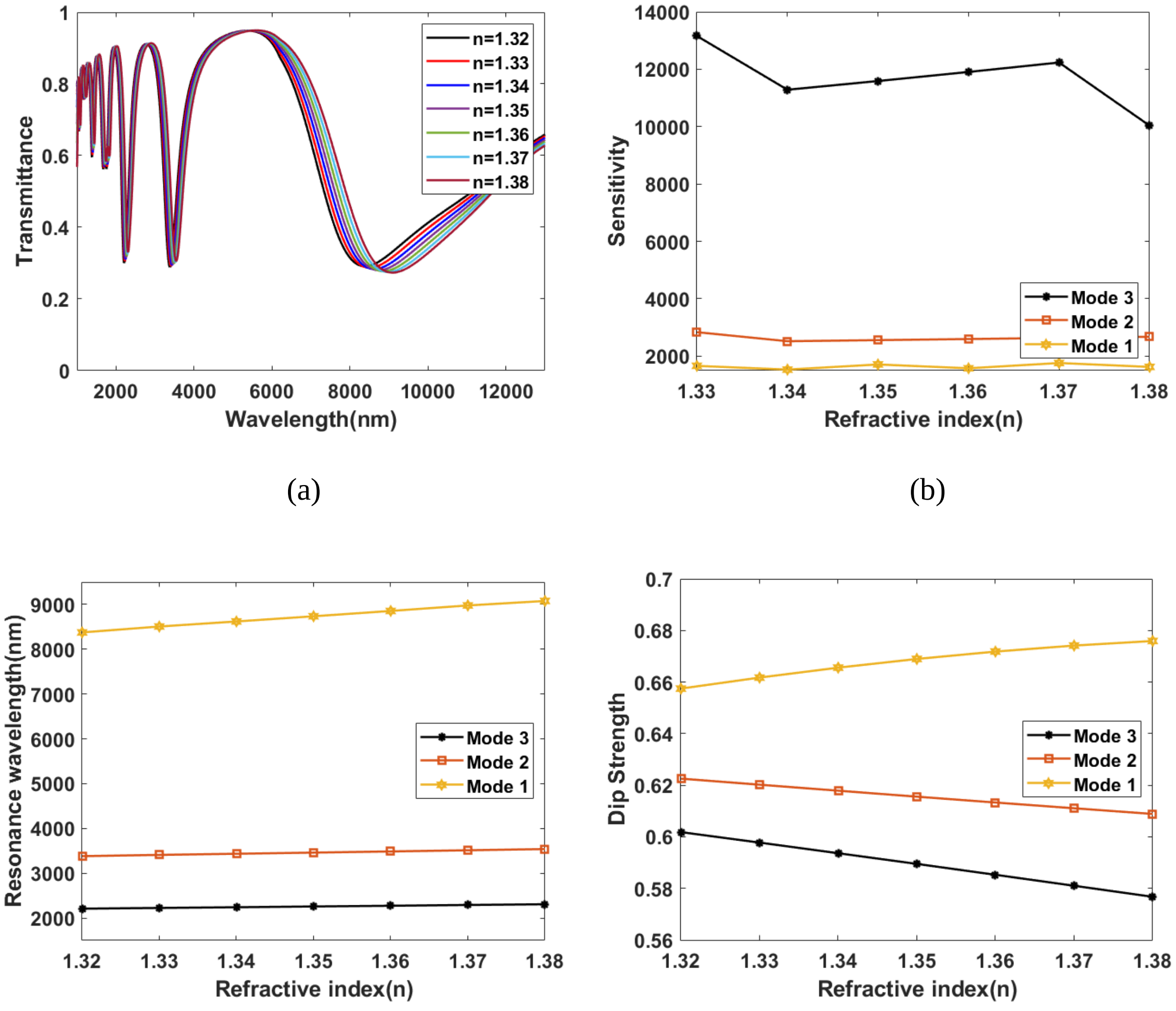

(a) (b)

(c) (d)

Figure 5.8: (a) The transmittance vs. the wavelength after the optimization process for n = 1.32 to 1.38 with an increment of 0.01. (b) Sensitivity (c) Dip Strength (ΔT), and (d) Resonant Wavelength for 3 modes.

Table 3 provides a comprehensive overview of the geometric properties that result in the highest sensitivity. Figure 5.8(a) depicts the transmittance spectra of the sensor after the optimization procedure. The resonance wavelength increases as the refractive index rises. Consequently, both P_{ef} and n_{ef} rise, resulting in an increase in sensitivity. The dip strength endures a substantial increase during the optimization process, reaching 0.831147 for mode 1. When the ambient refractive index descends between 1.32 and 1.38, a significant redshift in the resonant peak and the highest sensitivity of 13157 nm/RIU in mode 3 are observed. Considering a spectrum resolution of $\Delta\lambda = 0.01$, the sensing resolution in this instance is 7.6×10^{-8} RIU.

5.5 Fabrication

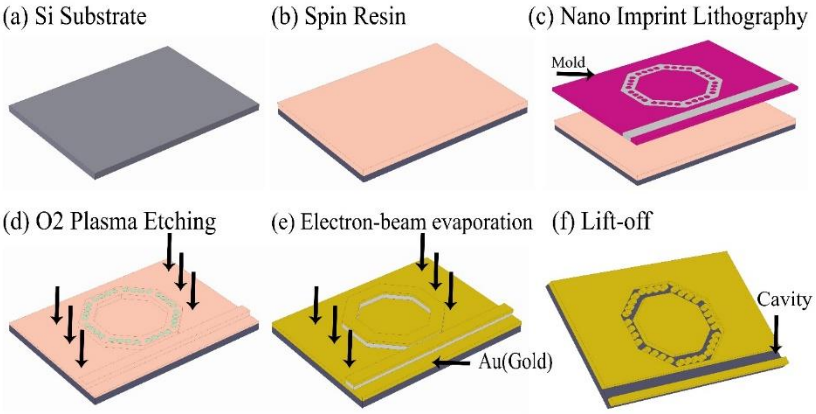

Figure 5.9: Nanoimprint fabrication process for the proposed sensor.

Various techniques, such as focused ion beam milling (FIB), electron beam lithography (EBL), and nanoimprint lithography (NIL), can be used to fabricate the proposed structure. These maskless fabrication technologies offer a high level of resolution. Due to its low cost and high throughput, nanoimprint lithography (NIL) is notably advantageous for both commercial and academic applications [98]. Using a mold, the proposed sensor design is transferred onto a resin-coated Si substrate. After removing the undesired resin layer with additional O_2 plasma etching, an Ag layer is deposited onto the substrate via electron beam evaporation. In the final stage of the lift-off process, the imprint of the resin is eliminated by cavities [99]. The nanosensor manufacturing procedure is depicted in Figure 5.9. Nanofilling permits the incorporation of sensing materials into the device via capillary attraction. By modifying the concentration of the glucose solution, the refractive index can be modulated, allowing for effective sensing [100].

5.6 Application

Different biological components can be identified based on their refractive indices. Various types of water have different refractive indices. For example, normal water has a refractive index of

1.33, while other types exhibit minor variations [101]. All of the previously specified water types have refractive indices between 1.32 and 1.38.

In Figure 5.10, the proposed sensor, which has an octagonal shape and 32 nanorods, is illustrated by transmittance vs wavelength variations induced by the refractive index of each liquid type. This wavelength range encompasses the entire refractive index range of water and extends to certain other liquids, where the sensor obtains a remarkable sensitivity of 13157 nm/RIU.

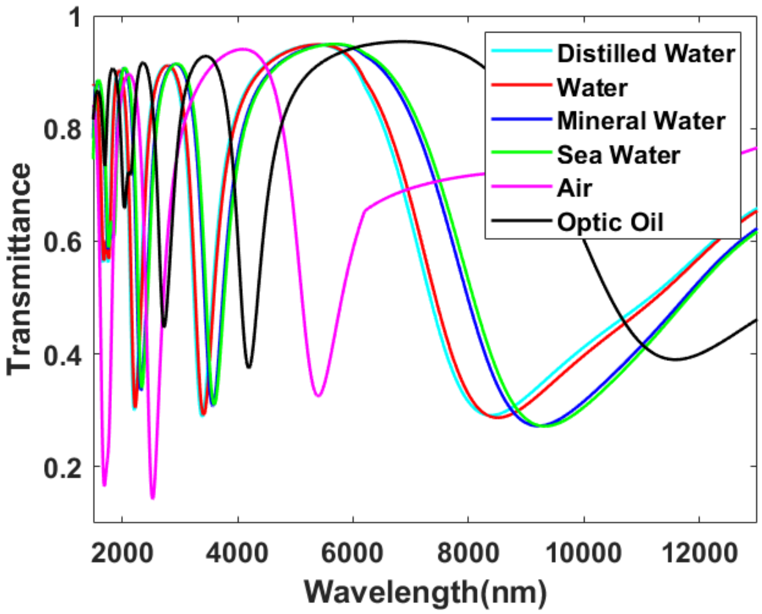

Figure 5.10: Transmittance spectra of the proposed sensor for detecting various fluids.

Chapter 6

Modeling, Optimization and Numerical Analysis of the Proposed PCF-SPR Sensor

6.1 Sensor Structure and Theoretical Analysis

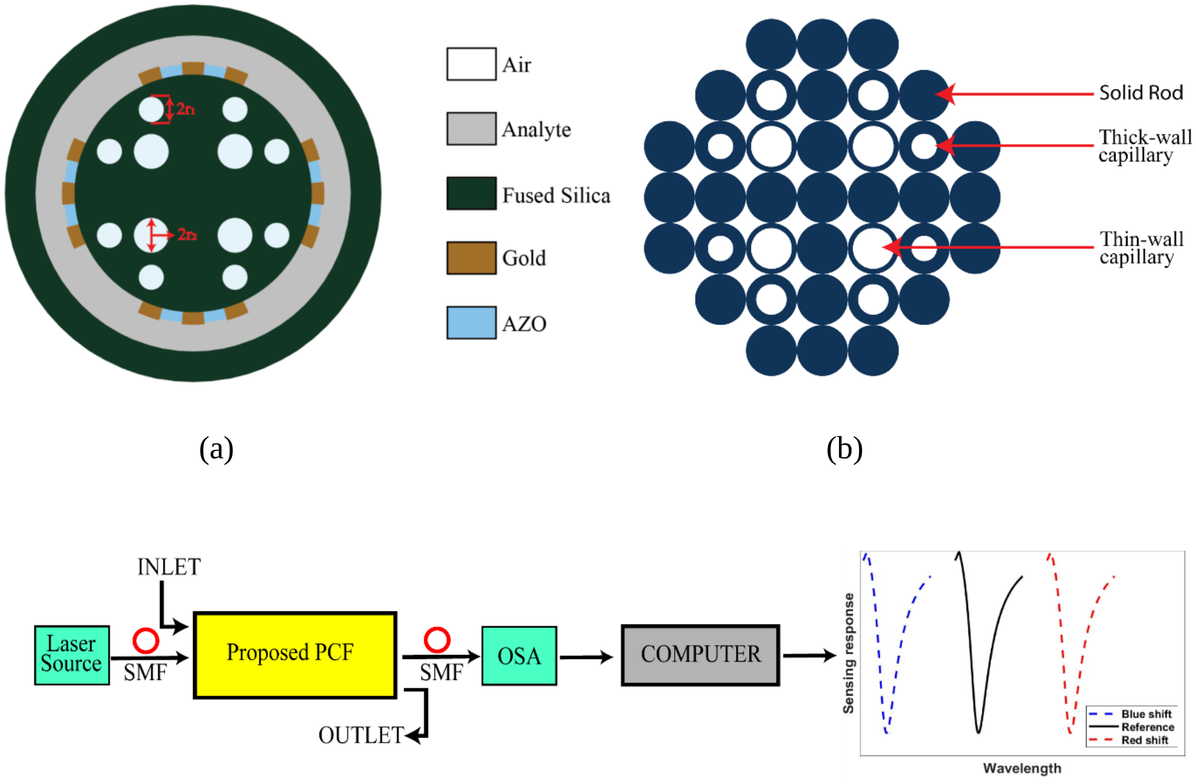

(a) (b)

(c)

Figure 6.1: (a) 2D structure of suggested sensor, (b) Stacked preform, and (c) Experimental setup for the proposed sensor.

This study is notable for its use of arrays composed of two distinct plasmonic materials arranged orthogonally for the detection of an analyte. This unique structural configuration permits the differentiation of analytes with multiple peaks, giving the facility to select any specific peaks based on preferred wavelength ranges. Using arrays of distinct plasmonic materials, PCF-SPR optical sensors can generate multiple peaks. Previous research has investigated the presence of multiple peaks associated with higher-order SPP modes, not for arrays of various plasmonic materials [102].

6.2 Optimization of Different Parameters

Using **FEM** implemented in COMSOL Multiphysics 6, the proposed structure is evaluated. The study specifically analyzes four consecutive peaks, with the gold and AZO plasmonic layers having respective thicknesses of 30 nm and 20 nm.

6.2.1 Thickness of Gold Plasmonic Layer

Figure 2(a) depicts the CL of the fiber at a RI of 1.422 as the thickness of the gold layer is increased from 30 nm to 40 nm with 10 nm increments. It is observed that the resonance wavelength for the last three peaks increases predominantly with increasing gold layer thickness. Notably, altering the gold layer thickness between 30 nm and 40 nm results in a significant redshift and a reduction in propagation loss. Figure 2(c) explicitly depicts the loss spectra for a 35 nm thick gold layer. Remarkably, with a 35 nm gold layer, the highest sensitivity is obtained, reaching 4,000 nm/RIU for the third peak and 20,000 nm/RIU for the fourth peak. The optimal thickness of the gold plasmonic layer is therefore determined to be 35 nm.

6.2.2 Thickness of AZO Plasmonic Layer

Figure 6.2(b) depicts the CL of the fiber varying AZO layer thickness from 20 nm to 30 nm in 5 nm increments, assuming a refractive index (RI) value of 1.422. As shown in Figure 6.2(b), the confinement loss exhibits a nonlinear behavior in this frequency range, and the resonance wavelengths for the 1st and 4th peaks vary. The loss spectra in Figure 6.2(d) corresponds to a 25 nm AZO plasmonic layer. At this optimal thickness, the measured loss peaks are 4.3487 dB/cm, 21.86 dB/cm, 60.286 dB/cm, and 260.87 dB/cm, respectively. Notably, exceeding the optimal thickness of the plasmonic layer limits light transmission, resulting in a loss of sensitivity. Therefore, the optimal thickness for the AZO plasmonic layer has been determined to be 25 nm.

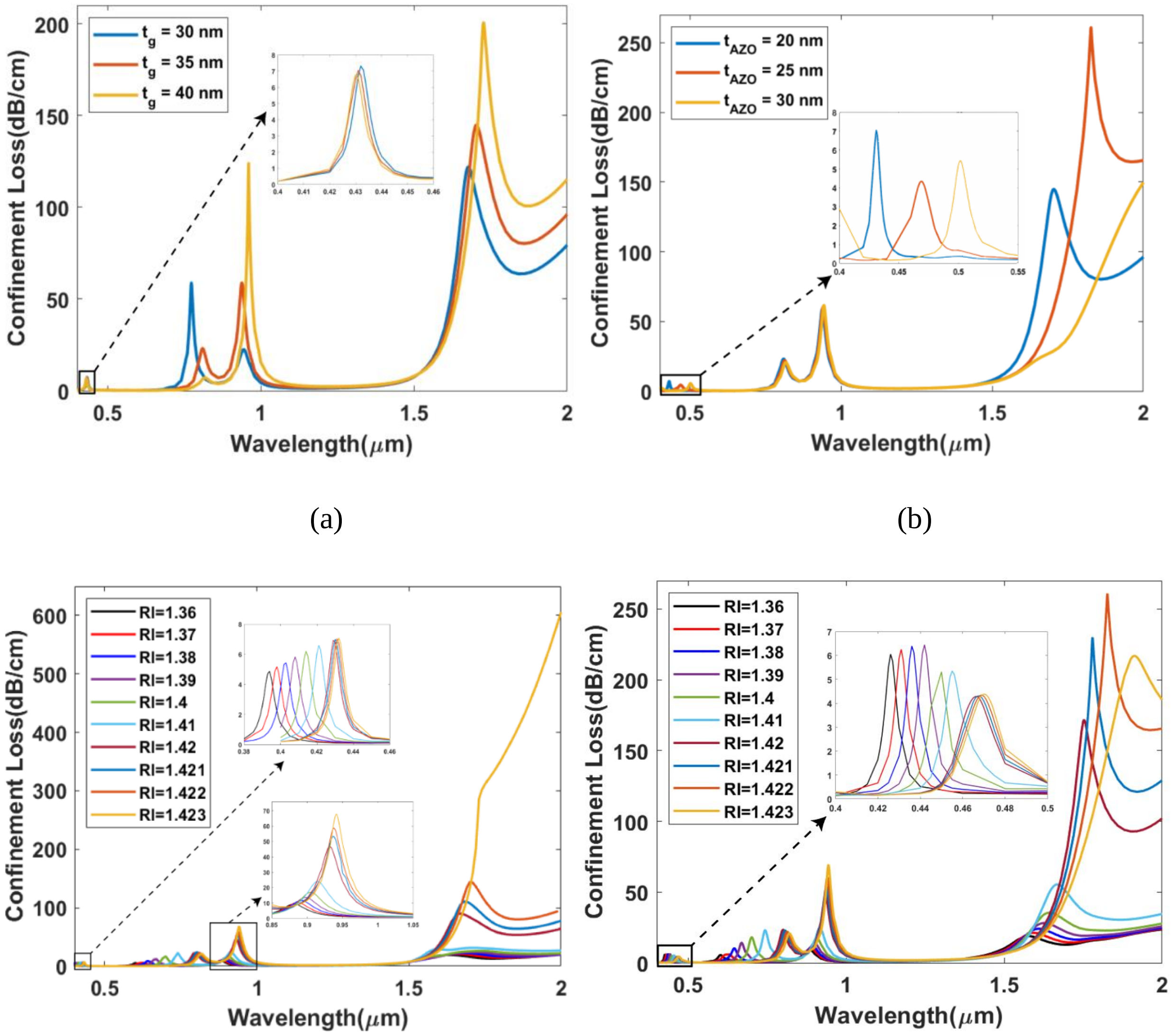

(a) (b)

(c) (d)

Figure 2: CL spectra of the proposed sensor by changing (a) tg, (b) tAZO, for optimum thickness of (c) 35 nm gold layer, (d) 25 nm AZO layer with variation of Refractive index.

6.2.3 The radius of Air Holes

For a small air hole radius, an analysis of the structure with analytes having a RI of 1.422 was conducted. The range of the tiny radius is increased from 0.8 to 1.0 µm by 0.1 µm, as seen in figure 6.3(a). Figure 6.3(a) indicates that CL increases with the decrement of the radius from 1.0 µm to 0.8 µm. This effect arises because light can be redirected effectively to the cladding than to the air spaces [103]. Considering its superior coupling and WS, a tiny air hole with a radius of 0.9 µm was chosen for the optimal choice. Furthermore, the large air hole radii was increased by 0.05 µm, beginning at 1.2 µm and reaching 1.3 µm. As depicted in Figure 3(b), the maximum CL for the large air holes with a radii of 1.25 µm is 260.87 dB/cm. Changing the radii of the large air holes can also reduce the peak loss. So, there are fewer surface plasmons that substantially influence the SPR sensor, decreases in sensitivity [104]. The maximum wavelength sensitivity (WS) value of 85,300 nm/RIU is attained for a r_2 value of 1.25 µm. So, 1.25 µm is chosen for optimum radius.

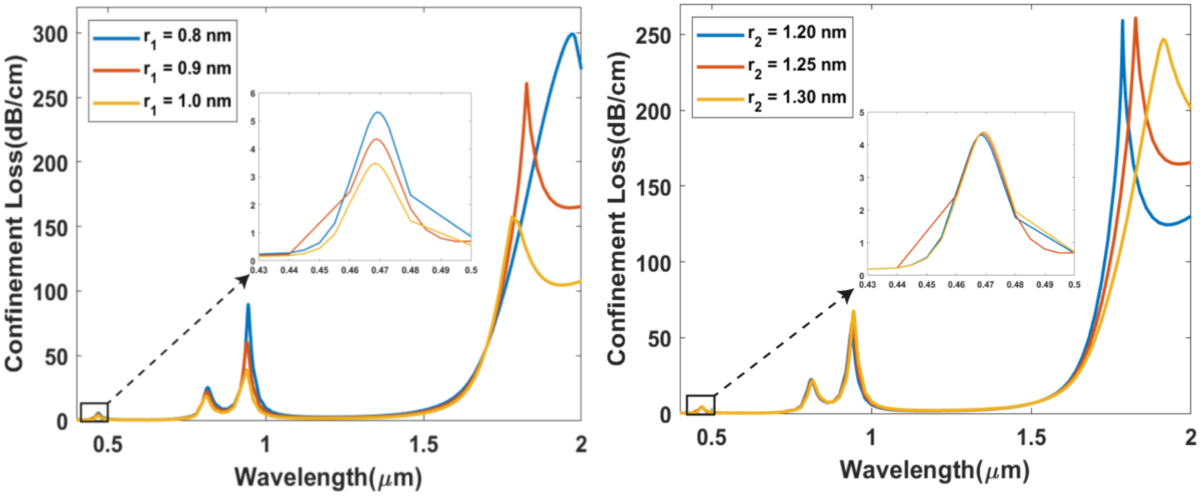

(a) (b)

Figure 3: CL spectrum for the proposed sensor by varying (a) r_1, and (b) r_2

6.3 Features of the proffered sensor

6.3.1 Multiple Resonance

Surface plasmon resonance occurs when the frequencies of the evanescent field and electron vibration in a plasmonic material align. At certain wavelengths and for certain refractive indices, distinguishing between core mode and SPP mode becomes challenging. This means that the fiber has its highest absorption at that specific wavelength, leading to resonance and a notable peak in confinement loss. For the arrays of two distinct plasmonic materials, the proposed sensor separates the evanescent field into distinct segments, allowing each material to generate multiple SPP modes simultaneously. Figure 6.4 depicts the photo energy distribution of core and SPP modes for the four consecutive peaks, with SPP modes depicted in Figure 6.4(a-d) and core-guided mode in Figure 6.4(e-h). Multiple phase-matching conditions and peaks are observed. AZO, and gold plasmonic layers contribute to these multiple peaks, which resulted in the identification of four phase-matching conditions and subsequent analysis of four loss peaks. Fig. 6.4(i) depicts the dispersion relation for the four peaks.

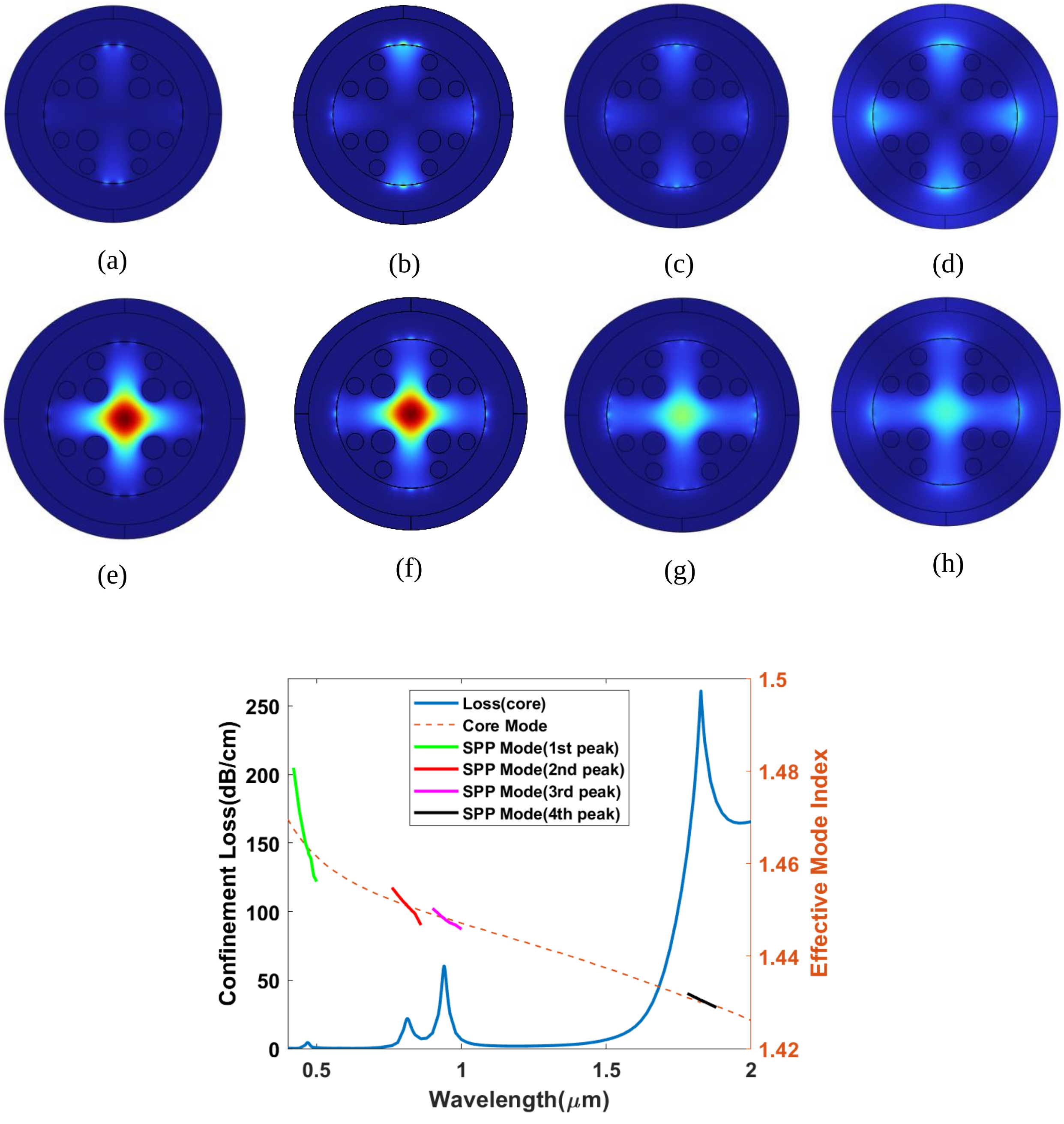

(a) (b) (c) (d)

(e) (f) (g) (h)

(i)

Figure 4: Optical distribution of (a - d) SPP mode and (e - h) core mode for four peaks, and (i) dispersion relation of the proposed sensor for RI = 1.422.

6.3.2 Analyte RI Detection

The proposed sensor can detect analytes with resonance wavelengths ranging from 400 to 2000 nm and refractive index from 1.36 and 1.423.

Figure 6.5 depicts the CL profile observed in the suggested sensor for various analytes with refractive indices from 1.36 to 1.423. As the index of refraction increases, the resonant peaks attenuate. Due to higher sensitivity within the refractive indices ranging from 1.36 to 1.423, detecting the refractive index of analytes is suitable for applications such as identifying organic chemical substances, and accurately diagnosing diseases. Consequently, the suggested sensor has applications in the biomedical areas.

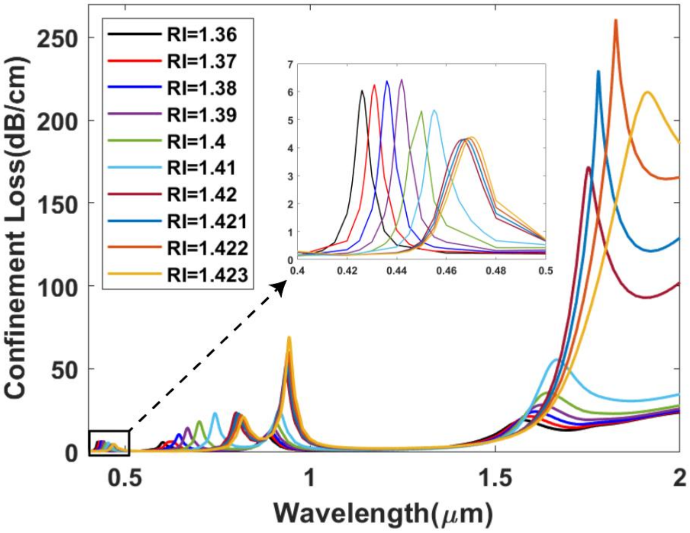

Figure 5: Confinement loss within RI span 1.36 - 1.423.

6.3.3 Maximum Spectral Sensitivity

Figure 6(a-d) illustrates the WS for the four analyzed peaks at various wavelengths. The first peak has the highest WS at 2,000 nm/RIU, while the second and third peaks have sensitivities of 7,000 nm/RIU and 4,000 nm/RIU, respectively. At a RI of 1.422, the greatest wavelength sensitivity for the fourth peak is 85,300 nm/RIU. Figure 6.6 depicts the WS for the proposed sensor for multiple peaks.

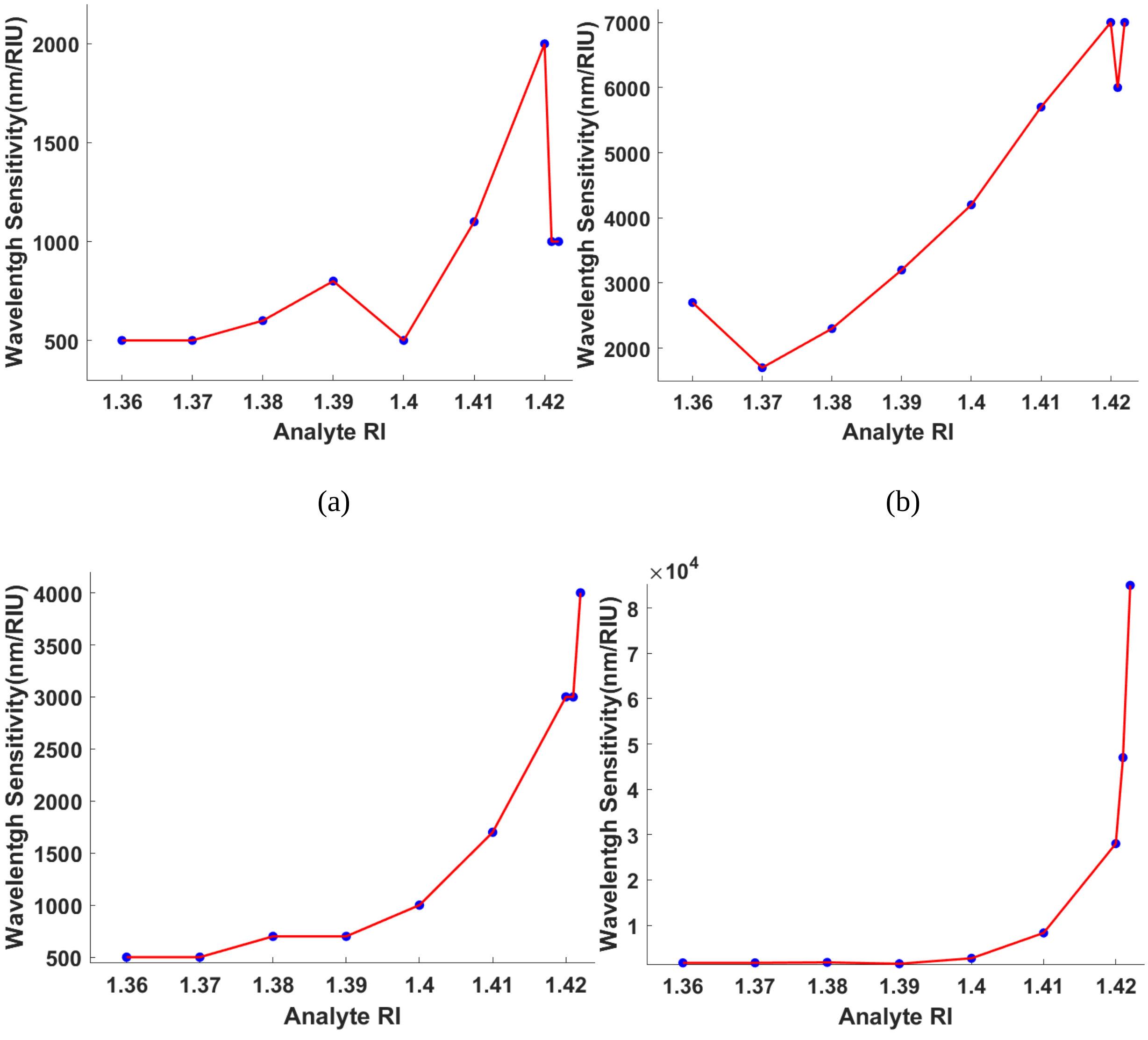

(a) (b)

(c) (d)

Figure 6: WS of four peaks with different RIs.

6.3.4 Maximum Amplitude Sensitivity

Figure 6.7 illustrates the AS analysis for refractive indices ranging from 1.36 to 1.423. Within this range, the a maximum AS achieved is 800.037 RIU^{-1} at 0.746 μm for the 2nd peak, and 793 RIU^{-1} at 1.826 μm for the 4th peak. These results highlight the efficiency and stability of our sensor.

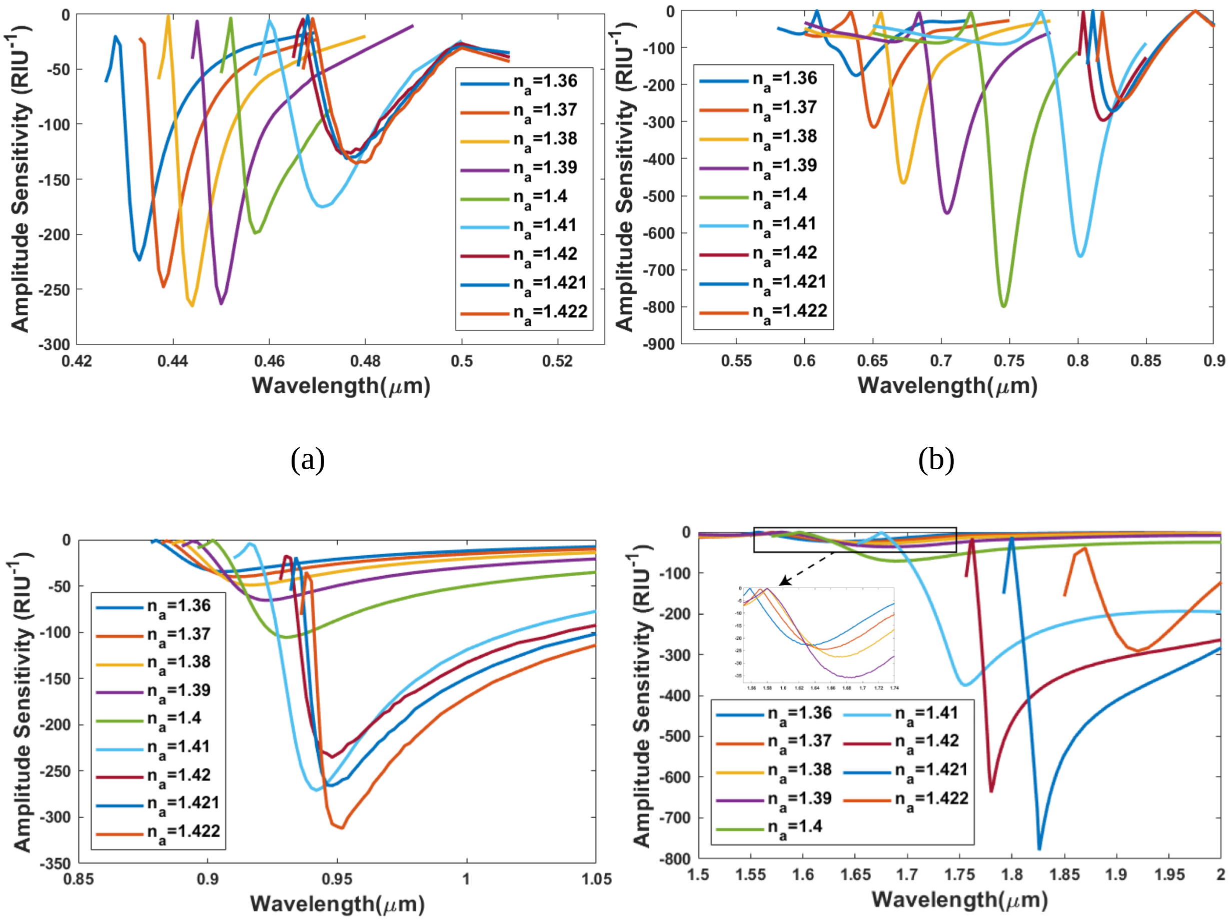

(a) (b)

(c) (d)

Figure 7: AS of four peak with different RIs.

6.3.5 Effective Calibration of the Sensor

To calibrate a sensor effectively, it is essential to have a linear sensor. Fig. 8 shows how regression analysis methods are used to measure the performance of the sensor. In Fig. 8 (a-d), the resonant wavelengths of multiple peaks are fitted with polynomial curves, with corresponding R-squared values. The proposed sensor has four peaks, allowing for four distinct curve fittings. 1st peak achieves the quadratic fitting equation y = $5.16196x^2 - 13.68314x + 9.48799$ that yields a coefficient value of $R^2 =$ 0.997015, indicating a closeness to 1. 2nd peak is described by the cubic equation $761.03x^3 - 3139.20x^2 + 4318.39x - 1980.49$, with $R^2 =$ 0.99978. Similarly, 3rd peak is expressed by the cubic fitting equation y = $313.42358x^3 - 1295.68036x^2 + 1785.89462x - 819.84699$ with a coefficient of $R^2 =$ 0.99798.

The fifth order equation $y = 1.30405x^5 - 9.05057x^4 + 25.12436x^3 - 34.87071x^2 + 24.19766x - 6.71619$ yields a coefficient value of $R^2 = 0.98091$ for the fourth peak.

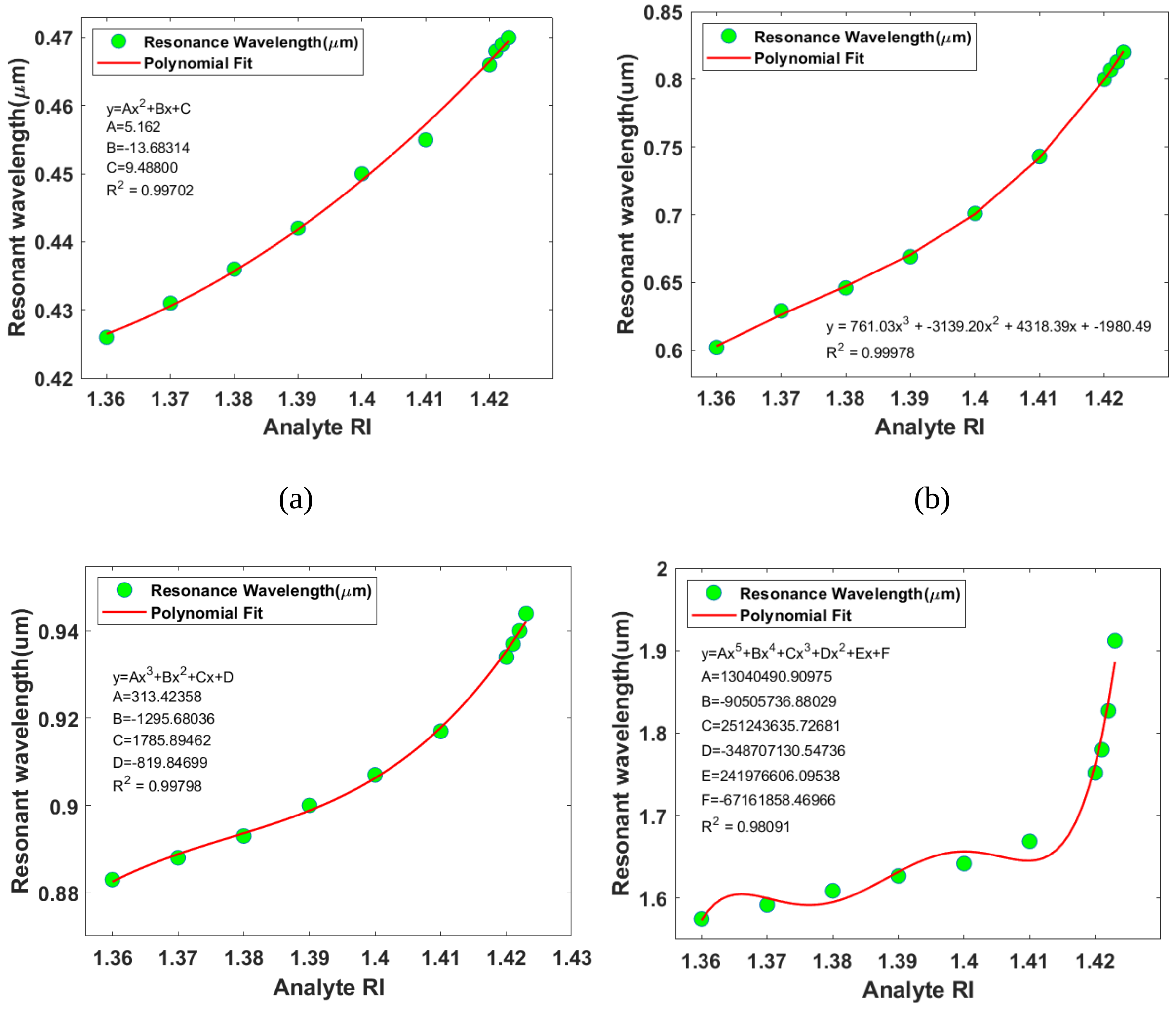

(a)

(b)

(c)

(d)

Figure 8: Regression lines of the four peaks of resonant wavelengths at different RIs.

6.3.6 Sensor Length

The sensor length is illustrated in Figure 6.9. The suggested structure achieves the maximum sensor length of 0.233258 cm.

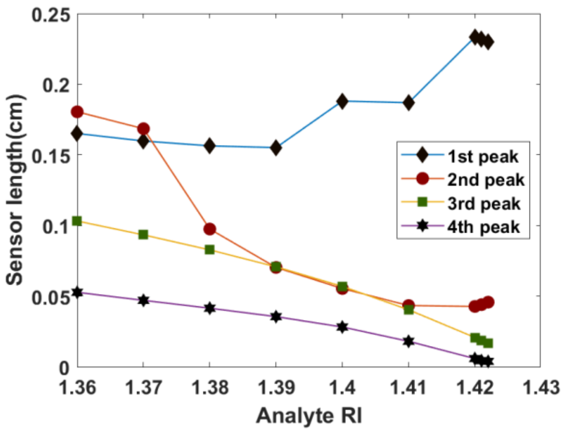

Figure 9: Sensor lengths of multiple peaks.

6.3.7 Figure of Merit (FOM)

A higher FOM value is required for a sensor to function properly. During model optimization, the proposed design attains an exceptionally high FOM of 370.8 RIU^{-1}. This significantly greater FOM achieved by utilizing multiple peaks has not been investigated in prior research. Consequently, the efficiency of the proposed sensor surpasses that of previous sensors [46, 57].

6.3.8 Resolution

The optimal amplitude resolution of 1.26×10^{-5} RIU **is achiev**ed when the RI is maintained at 1.422. In addition, the highest wavelength resolution obtained is 1.17×10^{-6} RIU. **Hence**, the sensor demonstrates the ability to precisely detect on the order of 10^{-6}.

6.3.9 Novel Peak Amplitude Difference Sensitivity (PADS)

As indicated previously, the proposed sensor design demonstrates multiple distinct CL peaks at different resonant wavelengths for a certain RI. The relationship between the difference in peak amplitude of even and odd peaks is depicted in Figure 6.10 (a, b). Due to the existence of multiple peaks, the amplitude disparity between each pair of peaks rises from 1.36 to 1.422. Indicated by a high coefficient of correlation $R^2 = 0.95051$, the correlation between the difference between the odd and even peaks for the same analyte refractive index is highly significant, while the equation for the second pair of peaks remains unchanged. This indicates that the relationship is highly linear.

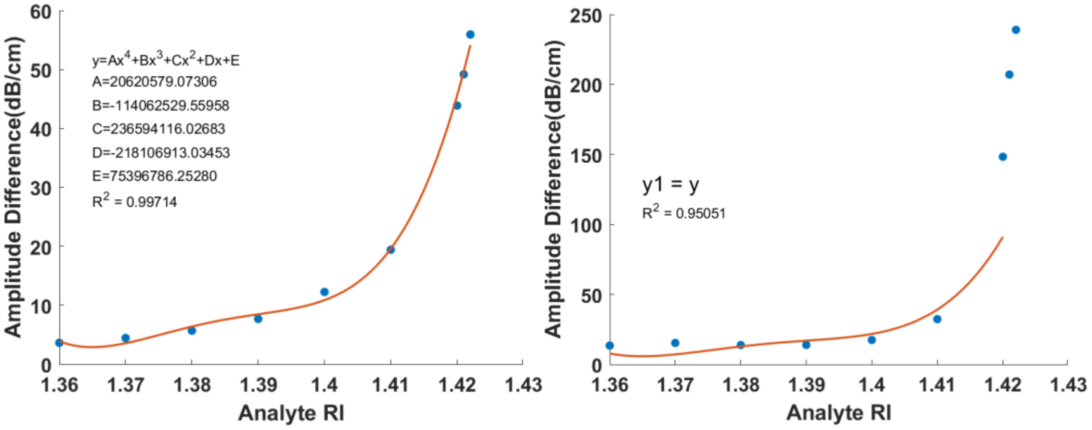

(a) (b)

Figure 10: Difference of peak amplitude of (a) odd peaks, and (b) even peaks.

Maximum PADS of 396.175 RIU^{-1} was demonstrated by the proposed sensor. Figure 6.11 illustrates the PADS for the odd peak and even peaks, with RI values ranging from 1.36 to 1.422.

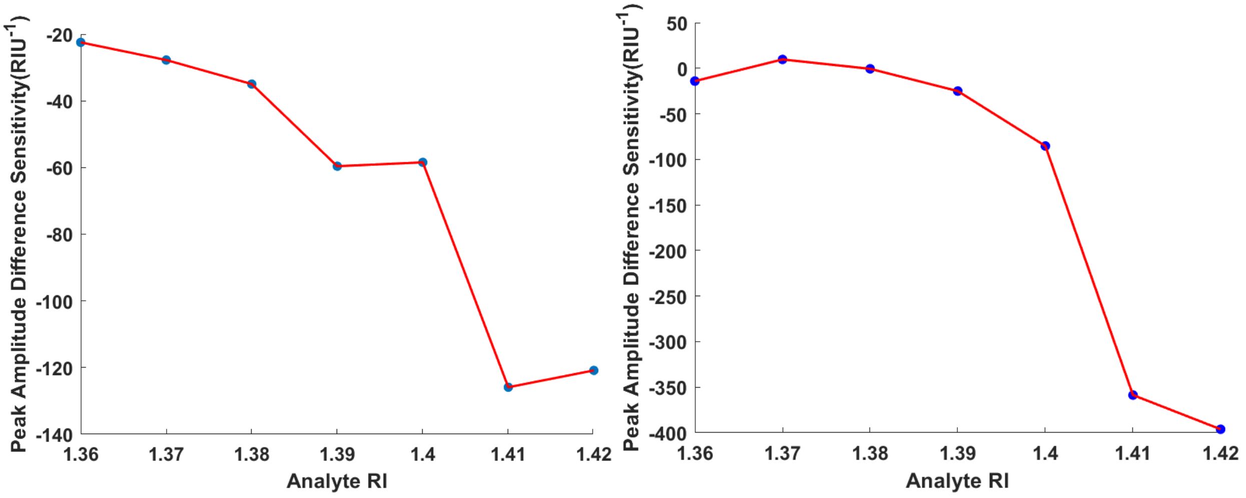

(a) (b)

Figure 11: Novel PADS within RI span 1.36-1.42 for (a) odd, and (b) even peaks.

Figure 6.11 displays the presence of two peak amplitude difference sensitivities that correspond to the four distinct peaks with a high correlation coefficient of $R^2 = 0.9332$. Consequently, either one of these can detect the RI of the substate. When confirmation of detection is required, the second parameter can be utilized.

6.4 Fabrication Process

Figure 6.12 depicts the manufacturing procedure for the proposed sensor. Using the stack-and-draw technique, the sensor's core and cladding can be constructed [105]. Initially, capillaries with thick and thin walls that are approximately hundred times greater than the desired size are created. This arrangement of capillaries and solid rods corresponds to the pattern of air holes in the suggested sensor. Subsequently, the cane, an intermediate preform, is shaped in accordance with particular specifications. Two-step photolithography is used to fabricate AZO and gold layers [106]. Chemical Vapor Deposition (CVD) is utilized to cover the entire fiber surface uniformly with one of the plasmonic layers [107]. Then, a mask is utilized to encompass selectively the designated area for both plasmonic layers. Two pumps are used to create the sensor layer, with one pump allowing analytes to infiltrate the layer and the other pump removing them [108]. Using these techniques, the proposed sensor can be fabricated using conventional manufacturing processes.

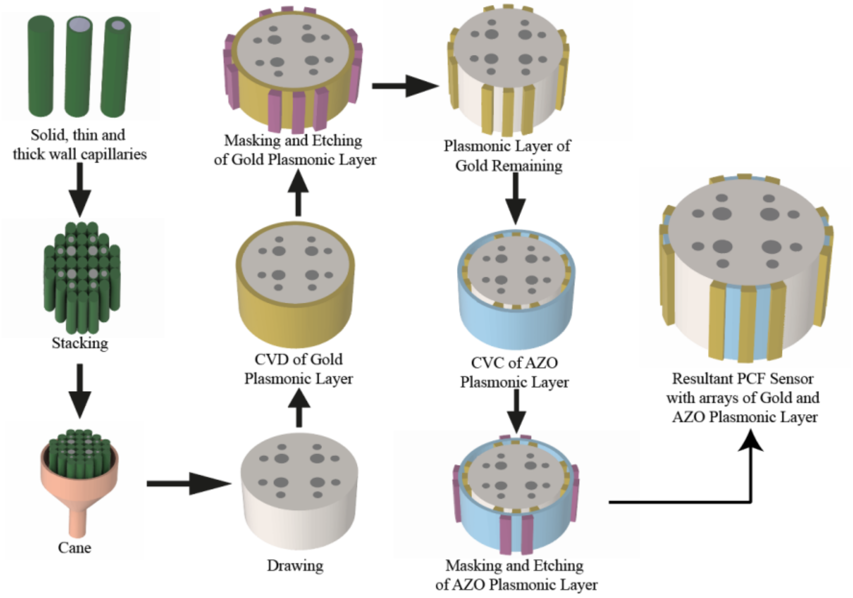

Figure 12: Fabrication process for the suggested sensor.

Chapter 7

Modeling, Optimization and Numerical Analysis of the Proposed PCF based SPR Sensor

7.1 Sensor Design and Theoretical Analysis

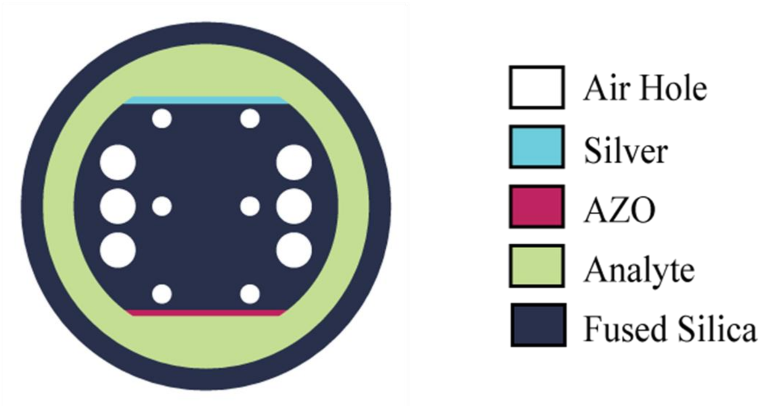

Figure 7.1: 2D view of the proposed PCF-SPR sensor.

Figure 7.1 depicts the geometric structure of the proposed sensor, which was designed using the software COMSOL Multiphysics 6a. The illustration demonstrates that the analyte layer and the Perfectly Matched Layer (PML) are located outside of the cladding region to enable external sensing. Two opposing plasmonic layers comprised of silver and AZO (Aluminum Zinc Oxide) are arranged beneath the analyte layer. Silver is chosen for its ability to increase sensitivity, whereas AZO is chosen for its operational frequency range, which enables deeper penetration of evanescent waves [109]. The cladding region is composed of two concentric rings of circular air holes, with ten octagonal-shaped rings and two central holes within each octagonal ring. The larger air holes, represented by r2, are strategically placed to tightly confine light within the core, thereby minimizing confinement loss. As the background material, fused silica is employed.

7.2 Features of the proffered sensor

7.2.1 Double Resonance

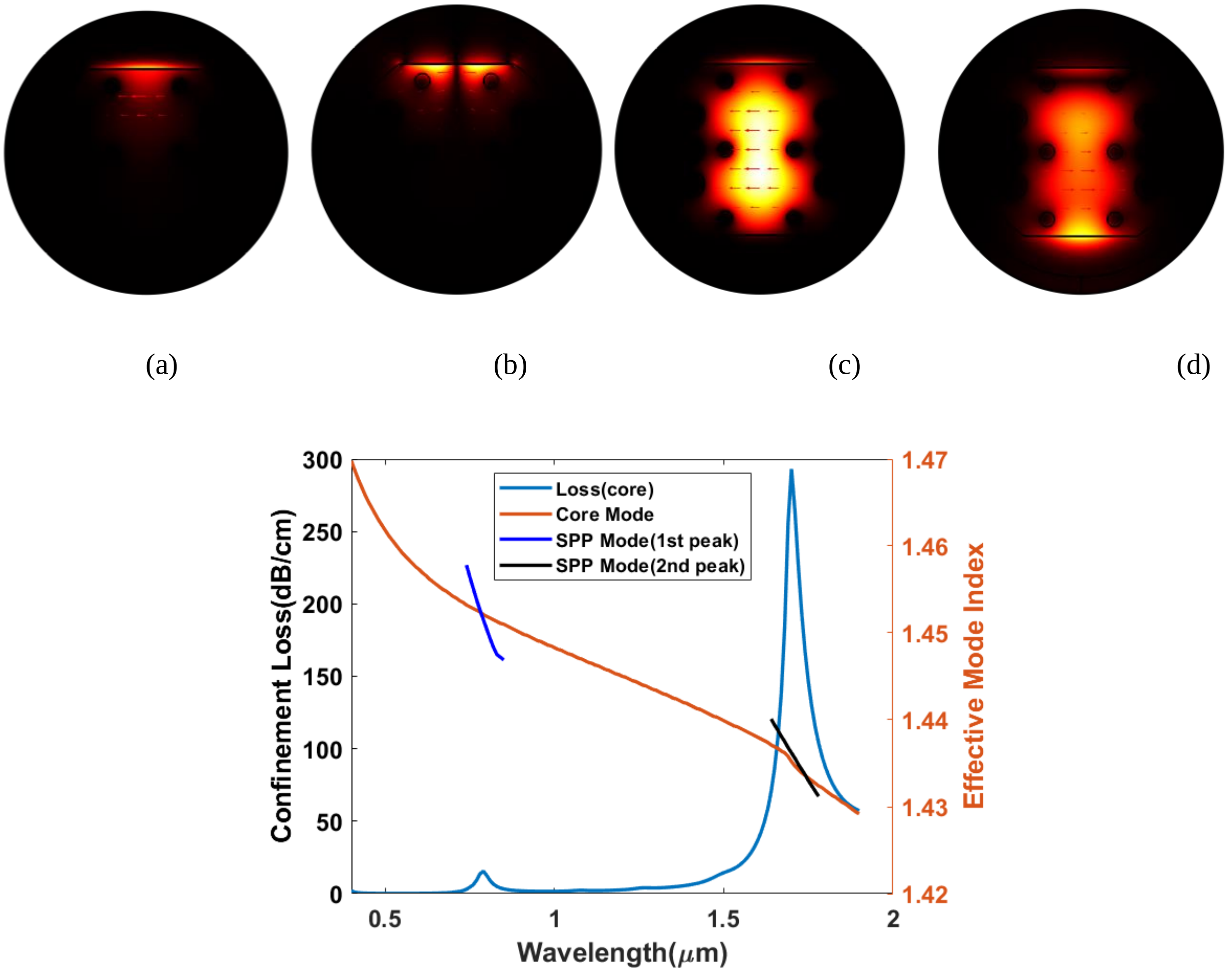

(a) (b) (c) (d)

(e)

Figure 7.2: Light Energy distribution of the (a, b) SPP mode and (c, d) core mode for two successive peaks, respectively, and (e) the dispersion relation of the core mode and two SPP modes at analyte RI of 1.4.

When the effective refractive index in both the core guide mode and SPP mode matches with each other, resulting in optimal light confinement, the fiber exhibits resonance at specific wavelengths. This resonance is distinguished by a notable peak in the inclusion loss. Using silver and AZO as plasmonic materials, the SPR-PCF sensor can split the evanescent field into two distinct SPP modes, one for each material. Consequently, both the x-polarized and y-polarized modes exhibit distinct resonant wavelengths and phase matching conditions. The distribution of the electromagnetic field is depicted in Figure 7.2 (a-d), where Figures 7.2 (a, b) depict the core mode and Figures 7.2 (c, d) depict the SPP mode. In e case of x polarization, the first loss peak is due to AZO, while the second loss peak is due to silver, as shown in Figure 7.2(e).

7.2.2 Analyte RI Detection

Our sensors can detect analytes with a refractive index between 1.34 and 1.42 in the xpol wavelength range of 400 to 1200 nm. We examined the confinement loss associated with these refractive index values through an investigation. Figure 8.5 demonstrates that as the refractive index increases, the loss trajectories shift to the red, resulting in peak shifts in all cases. As the refractive index of the analyte gradually increases, it tends to approach the value of the submerged cladding region in fused silica. This gradual decrease in the disparity between the core and cladding quantities improves their coupling. Therefore, as the propagation factors decrease, the effective mode index tends to decrease with the refractive index, causing the core and SPP modes to converge at longer wavelengths.

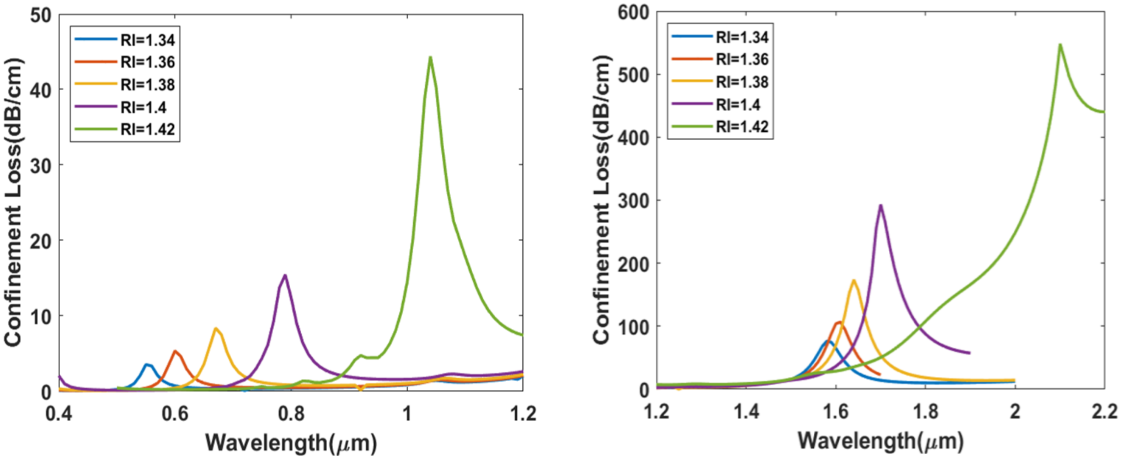

Figure 7.3: Confinement loss within RI span 1.34-1.42 for x-pol

7.2.3 Maximum Spectral Sensitivity

Spectral sensitivity is a measure of the effectiveness of perception in relation to the wavelength or frequency of light. In Figure 7.3, it is observed that the highest sensitivity achieved for the first peak is 24000 nm/RIU, while for the second peak, the highest sensitivity recorded is 34000 nm/RIU at RI = 1.42.

7.2.4 Maximum Amplitude Sensitivity

To practically implement the sensor, the first step is to couple a light source with the fiber that is surrounded by the target analyte [45]. Afterwards, the fiber-optic is connected, allowing light to propagate to the proposed PCF. When the incoming wave and the surface plasmon wave have the same frequency, surface plasmon resonance (SPR) occurs within the PCF, leading to significant light absorption and the appearance of an SPR dip at the output. This resonance dip can be measured using an optical spectrum analyzer, and its position can shift based on minute fluctuations in the refractive index (RI) of the analyte. To ensure a high degree of sensitivity, the observations were limited to a RI of 1.42, as the peak of the clipping loss diminishes, thereby decreasing the amplitude sensitivity. By employing the amplitude interrogation technique, we were able to achieve a remarkable amplitude sensitivity of 1248 RIU^{-1} for y-polarization, demonstrating the effectiveness and dependability of our design.

7.2.5 Resolution up to 10^{-6} Order

The resolution of sensors is a vital component of their ability to detect and accurately indicate small changes in the refractive index (RI). The amplitude interrogation method achieves a maximum resolution of 2.94×10^{-6} RIU for x polarization when the RI is maintained at 1.40.

7.3 Optimization of Silver Plasmonic Layer

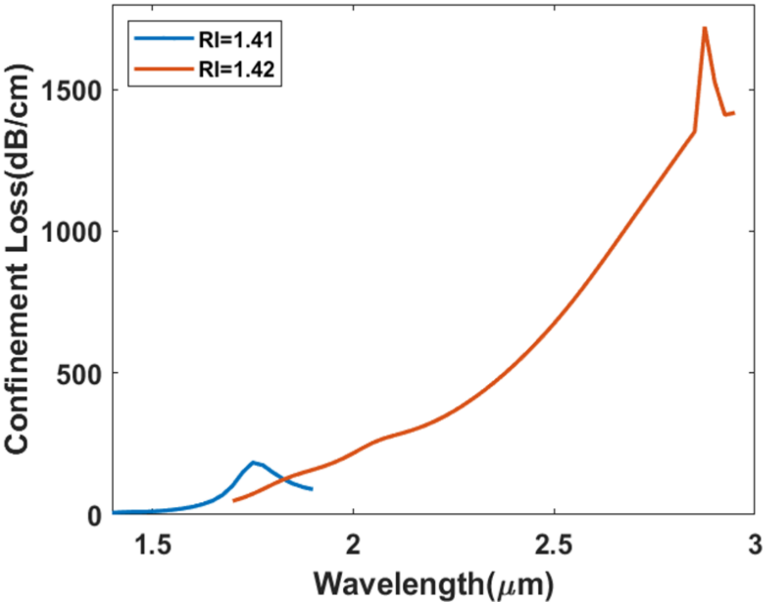

Figure 7.4: CL for optimum thickness of 60 nm silver layer.

The thickness of silver layer is critical to the sensor's performance. Changes in each of these parameters can cause the RW and loss peaks to vary. Here the changes in x-pol modes are explained because of their higher losses than that of y-pol. Figure 7.4 shows that increasing the thickness of silver to 60 nm pushes the peak of the losses to the right side and enhances the RW values. For RI of 1.41, the maximum sensitivity achieved is **1,12,500 nm/RIU** which is higher than any other research so far our knowledge. So, the optimal thickness of the silver layer is fixed to 60 nm.

Chapter 8

Conclusion and Future Work

8.1 Conclusion

The proposed waveguide-based sensor consists of dual octagonal rings and a straight waveguide. Extensive simulations display that the transmission spectrum shows notable shifts in resonant wavelengths due to alterations in nanorods, and a maximum sensitivity of 13,157 nm/RIU is obtained. Moreover, dip strength and sensing resolution of the sensor are 0.8311 and 7.6×10^{-8} RIU, respectively. The tolerance capability of the structure is also studied by introducing nano slits on the rings and demonstrates satisfactory performance. Furthermore, the sensor proves to be highly sensitive for the label-free detection of different types of water, air, and optic oil.

In case of PCF-SPR sensors, using surface plasmon resonance, we were able to determine the identity of the unknown analyte. The PCF-based SPR sensors have a small structure, and the evanescent field can be controlled by adjusting certain PCF parameters. By modifying the air cavity geometries, it is possible to control the propagation of light through the cladding region of photonic crystal fibers (PCFs). Various plasmonic materials are utilized to increase the sensors' sensitivity. Maximum amplitude sensitivity and maximum wavelength sensitivity are the most important factors in determining the effectiveness of a sensor. In this thesis, we have provided an in-depth analysis of all the designs we have created each of which contributes uniquely to the field of biosensing. Four distinctive SPR biosensor designs have been described in detail, each of which demonstrates outstanding sensing performance. All sensors have a precisely matched layer (PML) surrounding the fiber, which guarantees the absorption of the dispersed evanescent field. We performed numerical investigations using the full vectorial finite element method (FEM) method of the COMSOL Multiphysics simulation software. All parameters of the fiber have been optimized for optimal sensing performance. These sensors can be utilized at any temperature and force. Due to the simple and strategic nature of the designs, it will be simpler to fabricate them using the currently available techniques. As previously discussed, after optimizing all performance-determining parameters of the fibers, we discovered outstanding values for amplitude and wavelength sensitivities (AS and WS), confinement loss, birefringence, FOM, etc. Lastly, we can say that our devised sensors hold great promise for sensing applications and medical diagnostics due to their design feasibility and high sensitivity performance.

8.2 Future Work

In our designs, we have mostly used circular air holes of different diameters along with different placements of air holes. Adding to that we also used fused silica as background material mostly in designing our fibers. We believe that there are many opportunities to make further advancements for different applications of photonic crystal fiber along with improvements in the performance of fibers such as

1. Air holes of our designed second PCF based sensor can be optimized to achieve higher performance parameters.

2. The thickness of different plasmonic layers will be further optimized.

3. Different performance parameters will be optimized for better performance and detection.

4. Suitable fabrication process for more economic operations and label free detection.

References

[1] Munim, Nasir Muhammad, et al. "Design and analysis of an ultra-high sensitive and tunable metal-insulator-metal waveguide-coupled octagonal ring resonator utilizing gold nanorods." Sensing and Bio-Sensing Research, vol. 38, pp. 100529, 2022.

[2] Mohammad Rakibul Islam, et al. “Peak Amplitude Difference Sensitivity (PADS): An Interrogation Technique for PCF-SPR Sensors Using Symmetrical Arrays of Plasmonic Layers,” vol. 48, 2023, pp. 106434, https://doi.org/10.1016/j.rinp.2023.106434.

[3] Khan, M.R.H.; Chowdhury, A.A.; Islam, M.R.; Hosen, M.S.; Mim, M.H.; Nishat, M.M, “Wave-Shaped Microstructure Cancer Detection Sensor in Terahertz Band: Design and Analysis,” Appl. Sci., vol. 13, pp. 5784, 2023. https://doi.org/10.3390/app13095784

[4] Islam, M.R., Moazzam, E., Khan, R.L., Islam, R. and Tasnim, Z., 2023, “Analysis of a highly temperature-sensitive gold-coated plasmonic biosensor for analyte detection,” Ain Shams Engineering Journal, p.102206, 2023.

[5] Rahman, M., Islam, M.R. Siraz, S. and Anzum, M.S., “A high crosstalk modified D-shaped single-polarization filter for S and U band optical communication”, Optical and Quantum Electronics, vol. 55, no.3, p.276, 2023.

[6] Islam, Nazrul, Md Faizul Huq Arif, Mohammad Abu Yousuf, and Sayed Asaduzzaman, "Highly sensitive open channel based pcf-spr sensor for analyte refractive index sensing," Results in Physics, vol. 46, pp. 106266, 2023.

[7] Al Mahmud, Md Abdullah, Mohammad Rakibul Islam, A. N. M. Iftekher, Md Moshiur Rahman, and Farhana Akter Mou, "Design and numerical analysis of a porous core photonic crystal fiber for refractometric THz sensing," Microsystem Technologies, vol. 29, no. 1, pp. 115-126, 2023.

[8] Islam, Mohammad Rakibul, Md Moinul Islam Khan, Ahmed Mujtaba Al Naser, Fariha Mehjabin, Fatema Zerin Jaba, Jubair Alam Chowdhury, Fariha Anzum, and Mohibul Islam, "Design of a quad channel SPR-based PCF sensor for analyte, strain, temperature, and magnetic field strength sensing," Optical and Quantum Electronics, vol. 54, no. 9, pp. 563, 2022.

[9] Rahman, Md Moshiur, Farhana Akter Mou, Mohammed Imamul Hassan Bhuiyan, Md Abdullah Al Mahmud, and Mohammad Rakibul Islam, "Design and characterization of a photonic

crystal fiber for improved THz wave propagation and analytes sensing," Optical and Quantum Electronics, vol. 54, no. 10, pp. 669, 2022.

[10] Islam, Mohammad Rakibul, Ahmed Mujtaba Al Naser, Fatema Zerin Jaba, Fariha Anzum, Abu Nayeem Mohammad Iftekher, Md Rezaul Hoque Khan, and Mirza Muntasir Nishat, "Design of a hexagonal outlined porous cladding with vacant core photonic crystal fibre biosensor for cyanide detection at THz regime," IET Optoelectronics, vol. 16, no. 4, pp. 160-173, 2022.

[11] R. A. Wahsheh, Z. Lu, and M. A. Abushagur, “Nanoplasmonic couplers and splitters,” Optics Express, vol. 17, no. 21, pp. 19033–19040, 2009.

[12] Y. Guo, L. Yan, W. Pan, B. Luo, K. Wen, Z. Guo, H. Li, and X. Luo, “A plasmonic splitter based on slot cavity,” Optics Express, vol. 19, no. 15, p. 13831, 2011.

[13] M. Matsuo, H. Yabuki, and M. Makimoto, “Dual-mode stepped-impedance ring resonator for bandpass filter applications,” IEEE Transactions on Microwave Theory and Techniques, vol. 49, no. 7, pp. 1235–1240, 2001.

[14] Islam, Mohammad Rakibul, Kazi Rakibul Hasan, Md Moinul Islam Khan, Abu Nayeem Mohammad Iftekher, Fariha Mehjabin, Md Julkar Nayen, Jubair Alam Chowdhury, Saimon Bin Islam, and Mohibul Islam, "Design of a Dual Cluster and Dual Array-Based PCF-SPR Biosensor with Ultra-high WS and FOM," Plasmonics, vol. 17, no. 3, pp. 1171-1182, 2022.

[15] M. F. Hassan, R. H. Sagor, I. Tathfif, K. S. Rashid, and M. Radoan, “An optimized dielectric-metal-dielectric refractive index nanosensor,” IEEE Sensors Journal, vol. 21, no. 2, pp. 1461–1469, 2020.

[16] M. Butt, S. Khonina, and N. Kazanskiy, “Hybrid plasmonic waveguide-assisted metal–insulator–metal ring resonator for refractive index sensing,” Journal of Modern Optics, vol. 65, no. 9, pp. 1135–1140, 2018.

[17] R. Moreira, F. Chenlo, and A. Saint-Olympe, “Kinematic viscosity of aqueous solutions of ethanol and glucose in the range of temperatures from 20 to 45 c,” International Journal of Food Properties, vol. 12, no. 4, pp. 834–843, 2009.

[18] R. H. Sagor, M. F. Hassan, A. A. Yaseer, E. Surid, and M. I. Ahmed, “Highly sensitive refractive index sensor optimized for blood group sensing utilizing the 92 Fano resonance,” Applied Nanoscience (Switzerland), vol. 11, no. 2, pp. 521– 534, 2021.

[19] P. J. A. Sazio et al., “Microstructured optical fibers as high-pressure microfluidic reactors,” Science (80-.)., vol. 311, no. 5767, pp. 1583–1586, 2006, doi: 10.1126/science.1124281.

[20] M. A. Butt, S. N. Khonina, and N. L. Kazanskiy, “A plasmonic colour filter and refractive index sensor applications based on metal-insulator-metal square μ-ring cavities,” Laser Physics, vol. 30, no. 1, 2020.

[21] M. S. M. R. M. Islam et al., “Design and Analysis of a Biochemical Sensor Based on Surface Plasmon Resonance with Ultra-high Sensitivity,” Plasmonics, pp. 1–13, Jan. 2021, doi: 10.1007/s11468-020-01355-9.

[22] Islam, M.R., Khan, M.M.I., Mehjabin, F., Chowdhury, J.A., Islam, M., Yeasir, A.J., Mim, J.A. and Nahid, T.A., “Design of a dual spider-shaped surface plasmon resonance-based refractometric sensor with high amplitude sensitivity,” IET Optoelectronics, 17(1), pp.38-49, 2023.

[23] Rahman, Md Moshiur, Farhana Akter Mou, Mohammed Imamul Hassan Bhuiyan, and Mohammad Rakibul Islam, "Refractometric THz sensing of blood components in a photonic crystal fiber platform," Brazilian Journal of Physics, vol. 52, no. 2, pp. 47, 2022.

[24] X. Zhao, Z. Zhang, and S. Yan, “Tunable fano resonance in asymmetric mim waveguide structure,” Sensors, vol. 17, no. 7, p. 1494, 2017.

[25] N. Jankovic and N. Cselyuszka, “Multiple fano-like mim plasmonic structure based on triangular resonator for refractive index sensing,” Sensors, vol. 18, no. 1, p. 287, 2018.

[26] Q. Yang, X. Liu, F. Guo, H. Bai, B. Zhang, X. Li, Y. Tan, and Z. Zhang, “Multiple fano resonance in mim waveguide system with cross-shaped cavity,” Optik, vol. 220, p. 165163, 2020.

[27] M. R. Rakhshani, “Optical refractive index sensor with two plasmonic doublesquare resonators for simultaneous sensing of human blood groups,” Photonics and Nanostructures - Fundamentals and Applications, vol. 39, no. October 2019, p. 100768, 2020.

[28] Y.-Y. Xie, Y.-X. Huang, W.-L. Zhao, W.-H. Xu, and C. He, “A novel plasmonic sensor based on metal–insulator–metal waveguide with side-coupled hexagonal cavity,” IEEE Photonics Journal, vol. 7, no. 2, pp. 1–12, 2015.

[29] Y. Wang, M. Zheng, Q. Ruan, Y. Zhou, Y. Chen, P. Dai, Z. Yang, Z. Lin, Y. Long, Y. Li, N. Liu, C. W. Qiu, J. K. Yang, and H. Duan, “Stepwise-nanocavityassisted transmissive color filter array microprints,” Research, vol. 2018, pp. 10– 14, 2018.

[30] Y. Zhang and M. Cui, “Refractive index sensor based on the symmetric mim waveguide structure,” Journal of Electronic Materials, vol. 48, no. 2, pp. 1005– 1010, 2019.

[31] M. A. Butt, S. N. Khonina, and N. L. Kazanskiy, “Metal-insulator-metal nano square ring resonator for gas sensing applications,” Waves in Random and Complex Media, vol. 0, no. 0, pp. 1–11, 2019.

[32] H. Su, S. Yan, X. Yang, J. Guo, J. Wang, and E. Hua, “Sensing features of the fano resonance in an MIM waveguide coupled with an elliptical ring resonant cavity,” Applied Sciences (Switzerland), vol. 10, no. 15, 2020.

[33] Y.-P. Qi, L.-Y. Wang, Y. Zhang, T. Zhang, B.-H. Zhang, X.-Y. Deng, and X.-X. Wang, “Multiple fano resonances in metal–insulator–metal waveguide with umbrella resonator coupled with metal baffle for refractive index sensing,” Chinese Physics B, vol. 29, no. 6, p. 067303, 2020.

[34] K. Diest, J. A. Dionne, M. Spain, and H. A. Atwater, “Tunable color filters based on metal-insulator-metal resonators,” Nano Letters, vol. 9, no. 7, pp. 2579–2583, 2009.

[35] M. A. Butt, S. N. Khonina, and N. L. Kazanskiy, “A plasmonic colour filter and refractive index sensor applications based on metal-insulator-metal square μ-ring cavities,” Laser Physics, vol. 30, no. 1, 2020.

[36] Z. Zhang, J. Yang, H. Xu, S. Xu, Y. Han, X. He, J. Zhang, J. Huang, D. Chen, and W. Xie, “A plasmonic ellipse resonator possessing hybrid modes for ultracompact chipscale application,” Physica Scripta, vol. 94, no. 12, p. 125511, 2019.

[37] Islam, Mohammad Rakibul, A. N. M. Iftekher, Mariea Sharaf Anzum, Muntaha Rahman, and Sadia Siraz, "LSPR Based Double Peak Double Plasmonic Layered Bent Core PCF-SPR Sensor for Ultra-Broadband Dual Peak Sensing," *IEEE Sensors Journal, vol.* 22, no. 6, pp. 5628-5635, 2022.

[38] Khetani, A.; Momenpour, A.; Alarcon, E.I.; Anis, H. Hollow core photonic crystal fiber for monitoring leukemia cells using surface enhanced raman scattering (SERS). Biomed. Opt. Express 2015, 6, 4599. [Google Scholar] [CrossRef][Green Version]

[39] Fang, L.-M.; Chen, H.-M. Double-core D-type photonic crystal fiber refractive indexsensor based on grid coating. Proc. SPIE 2019, 11191, 13. [Google Scholar]

[40] Mollah, M.A.; Yousufali, M.; Ankan, I.M.; Rahman, M.M.; Sarker, H.; Chakrabarti, K. Twin core photonic crystal fiber refractive index sensor for early detection of blood cancer. Sens. Bio-Sens. Res. 2020, 29, 100344. [Google Scholar] [CrossRef]

[41] Wang, D.; Yi, Z.; Ma, G.; Dai, B.; Yang, J.; Zhang, J.; Yu, Y.; Liu, C.; Wu, X.; Bian, Q. Two-channel photonic crystal fiber based on surface plasmon resonance for magnetic field and temperature dual-parameter sensing. Phys. Chem. Chem. Phys. 2022, 24, 21233–21241. [Google Scholar] [CrossRef]

[42] Fatema, S.; Absar, R.; Reja, M.I.; Akhtar, J. Effect of core infiltration in the birefringence of photonic crystal fiber. In Proceedings of the 2017 IEEE International Conference on Telecommunications and Photonics (ICTP), Dhaka, Bangladesh, 26–28 December 2017; pp. 1–5. [Google Scholar]

[43] Shafkat, A.; Reja, M.I.; Miah, M.J.; Fatema, S.; Absar, R.; Akhtar, J. Numerical exploration of external sensing scheme based photonic crystal fiber surface plasmonic sensor with different noble plasmonic materials and their alloys. Optik 2021, 231, 166418. [Google Scholar] [CrossRef]

[44] Wang, H.; Liao, M.; Xiao, H.; Han, X.; Jiang, Y.; Tan, J.; Zhang, P.; Shao, J.; Tian, Y.; Yang, J. High sensitivity temperature sensor based on a PDMS-assisted bow-shaped fiber structure. Opt. Commun. 2021, 481, 126536. [Google Scholar] [CrossRef]

[45] Rifat, A.A.; Haider, F.; Ahmed, R.; Mahdiraji, G.A.; Adikan, F.M.; Miroshnichenko, A.E. Highly sensitive selectively coated photonic crystal fiber-based plasmonic sensor. Opt. Lett. 2018, 43, 891–894. [Google Scholar] [CrossRef]

[46] Ramola, A.; Marwaha, A.; Singh, S. Design and investigation of a dedicated PCF SPR biosensor for CANCER exposure employing external sensing. Appl. Phys. A 2021, 127, 643. [Google Scholar] [CrossRef]

[47] Yan, X.; Wang, Y.; Cheng, T.; Li, S. Photonic crystal fiber SPR liquid sensor based on elliptical detective channel. Micromachines 2021, 12, 408. [Google Scholar] [CrossRef]

[48] Goodrich, T.T.; Lee, H.J.; Corn, R.M. Direct detection of genomic DNA by enzymatically amplified SPR imaging measurements of RNA microarrays. J. Am. Chem. Soc. 2004, 126, 4086–4087. [Google Scholar] [CrossRef]

[49] Nooke, A.; Beck, U.; Hertwig, A.; Krause, A.; Krüger, H.; Lohse, V.; Negendank, D.; Steinbach, J. On the application of gold based SPR sensors for the detection of hazardous gases. Sens. Actuators B Chem. 2010, 149, 194–198. [Google Scholar] [CrossRef]

[50] Mouvet, C.; Harris, R.D.; Maciag, C.; Luff, B.J.; Wilkinson, J.S.; Piehler, J.; Brecht, A.; Gauglitz, G.; Abuknesha, R.; Ismail, G. Determination of simazine in water samples by waveguide surface plasmon resonance. Anal. Chim. Acta 1997, 338, 109–117. [Google Scholar] [CrossRef]

[51] Eid, M.M.A.; Rashed, A.N.Z.; Bulbul, A.A.M.; Podder, E. Mono-rectangular core photonic crystal fiber (MRC-PCF) for skin and blood cancer detection. Plasmonics 2020, 16, 717–727. [Google Scholar] [CrossRef]

[52]Modeling_And_Simulation_Of_Surface_Plasmonic_Resonance_In_Photonic_Crystal_Fiber. Available online: http://studentsrepo.um.edu.my/8794/ (accessed on 1 March 2022).

[53] Kashif, M.; Bakar, A.A.A.; Hashim, F.H. Analysing surface plasmon resonance phase sensor based on mach-zehnder interferometer technique using glycerin. Opt. Commun. 2016, 380, 419–424. [Google Scholar] [CrossRef]

[54] Momota, M.R.; Hasan, M.R. Hollow-core silver coated photonic crystal fiber plasmonic sensor. Opt. Mater. 2018, 76, 287–294. [Google Scholar] [CrossRef]

[55] Wieduwilt, T.; Tuniz, A.; Linzen, S.; Goerke, S.; Dellith, J.; Hübner, U.; Schmidt, M.A. Ultrathin niobium nanofilms on fiber optical tapers—A new route towards low-loss hybrid plasmonic modes. Sci. Rep. 2015, 5, 17060. [Google Scholar] [CrossRef][Green Version]

[56] Haque, E.; Mahmuda, S.; Hossain, M.A.; Hai, N.H.; Namihira, Y.; Ahmed, F. Highly sensitive dual-core pcf based plasmonic refractive index sensor for low refractive index detection. IEEE Photonics J. 2019, 11, 1–9. [Google Scholar] [CrossRef]

[57] Shafkat, A.; Rashed, A.N.Z.; El-Hageen, H.M.; Alatwi, A.M. The effects of adding different adhesive layers with a microstructure fiber sensor based on surface plasmon resonance: A numerical study. Plasmonics 2021, 16, 819–832. [Google Scholar] [CrossRef]

[58] Suvarnaphaet, P.; Pechprasarn, S. Graphene-based materials for biosensors: A review. Sensors 2017, 17, 2161. [Google Scholar] [CrossRef][Green Version]

[59] K. Yee, "Numerical solution of initial boundary value problems involving maxwell's equations in isotropic media," IEEE Transactions on antennas and propagation, vol. 14, no. 3, pp. 302–307, 1966.

[60] A. Taflove and S. C. Hagness, Computational electrodynamics: the finitedifference time-domain method. Artech house, 200

[61] J.-P. Berenger, "A perfectly matched layer for the absorption of electromagnetic waves," Journal of computational physics, vol. 114, no. 2, pp. 185–200, 1994.

[62] T. Weiland, "A discretization method for the solution of maxwell's equations for six-component fields.-electronics and communication,(aeü), vol. 31," 1977.

[63] T. Weiland, "Time domain electromagnetic field computation with finite difference methods," International Journal of Numerical Modelling: Electronic Networks, Devices and Fields, vol. 9, no. 4, pp. 295–319, 1996.

[64] Z. Rahimi, "The finite integration technique (fit) and the application in lithography simulations," 2011.

[65] C. S. Desai and J. F. Abel, Introduction to the finite element method; a numerical method for engineering analysis. Van Nostrand Reinhold, 1971.

[66] M. N. Sadiku, Numerical techniques in electromagnetics with MATLAB. CRC press, 2018.

[67] A. D. Rakic, A. B. Djuriši ´ c, J. M. Elazar, and M. L. Majewski, “Optical proper- ´ ties of metallic films for vertical-cavity optoelectronic devices,” Applied optics, vol. 37, no. 22, pp. 5271–5283, 1998.

[68] “RP Photonics Encyclopedia - silica fibers, optical fiber, glass, fiber optics.” https://www.rp-photonics.com/silica_fibers.html (accessed Feb. 19, 2021).

[69] E. K. Akowuah, T. Gorman, H. Ademgil, S. Haxha, G. K. Robinson, and J. V. Oliver, “Numerical analysis of a photonic crystal fiber for biosensing applications,” IEEE J. Quantum Electron., vol. 48, no. 11, pp. 1403–1410, 2012, doi: 10.1109/JQE.2012.2213803.

[70] M. S. Islam et al., “A Hi-Bi Ultra-Sensitive Surface Plasmon Resonance Fiber Sensor,” IEEE Access, vol. 7, pp. 79085–79094, 2019, doi: 10.1109/ACCESS.2019.2922663.

[71] S. Sharmin, A. Bosu, and S. Akter, “A Simple Gold-Coated Photonic Crystal Fiber Based Plasmonic Biosensor,” in 2018 International Conference on Advancement in Electrical and Electronic Engineering (ICAEEE), Nov. 2018, pp. 1–4, doi: 10.1109/ICAEEE.2018.8643003.

[72] A. A. Rifat et al., “Surface Plasmon Resonance Photonic Crystal Fiber Biosensor: A Practical Sensing Approach,” IEEE Photonics Technol. Lett., vol. 27, no. 15, pp. 1628– 1631, Aug. 2015, doi: 10.1109/LPT.2015.2432812.

[73] J. N. Dash, R. Das, and R. Jha, “AZO coated microchannel incorporated PCF-based SPRsensor: A numerical analysis,” IEEE Photonics Technol. Lett., vol. 30, no. 11, pp. 1032–1035, 2018, doi: 10.1109/LPT.2018.2829920.

[74] S. A. Maier, “Surface plasmon polaritons at metal/insulator interfaces,” in Plasmonics: Fundamentals and Applications, pp. 21–37, Springer, 2007.

[75] Rohit Grover, “Indium Phosphide Based Optical Micro Ring resonators” PhD thesis, pages: 1- 50, Graduate School of the University of Maryland, Collage Park, 2003.

[76] Mi Kyoung Park, Jack Sheng Kee, Jessie Yiying Quah, Vivian Netto, Junfeng Song, Qing Fang, Eric Mouchel La Fosse, “Label-free aptamer sensor based on silicon microring resonator”, Sensor and Actuators B (2013), 552-559.

[77] Rajib Ahmed, Saeed Mahmud Ullah, “Design & Analysis on Silicon based Optical Micro-Ring Resonator Sensor Device for Biomedical Applications at μm wavelength”, In proceeding of CIOMP-OSA Summer Session: Lasers and Their Applications, 2011.

[78] Yuze Sun, Xudong Fan, “Optical ring resonator for biochemical and chemical sensing”, Springer, Anal Bional Chem (2011) 399: 205-211.

[79] H. F. Fakhruldeen and A. Z. Ghazi Zahid, “An Overview of Photonic Crystal Fiber (PCF),” no. April 2019, 2019, [Online]. Available: www.tnsroindia.org.in.

[80] M. A. Islam, M. R. Islam, S. Siraz, M. Rahman, M. S. Anzum, and F. Noor, “Wheel structured Zeonex-based photonic crystal fiber sensor in THz regime for sensing milk,” Appl. Phys. A Mater. Sci. Process., vol. 127, no. 5, pp. 1–13, 2021, doi: 10.1007/s00339- 021-04472-2.

[81] H. Emami Nejad, A. Mir, and A. Farmani, “Supersensitive and Tunable NanoBiosensor for Cancer Detection,” IEEE Sensors Journal, vol. 19, no. 13, pp. 4874–4881, 2019.

[82] N. L. Kazanskii, M. A. Butt, S. A. Degtyarev, and S. N. Khonina, “Achievements in the development of plasmonic waveguide sensors for measuring the refractive index,” Computer Optics, vol. 44, no. 3, pp. 295–318, 2020.

[83] M. F. Hassan, R. H. Sagor, I. Tathfif, K. S. Rashid, and M. Radoan, “An optimized dielectric-metal-dielectric refractive index nanosensor,” IEEE Sensors Journal, vol. 21, no. 2, pp. 1461–1469, 2020.

[84] I. M. White and X. Fan, “On the performance quantification of resonant refractive index sensors,” Optics express, vol. 16, no. 2, pp. 1020–1028, 2008.

[85] Chou Chao, Chung-Ting, Yuan-Fong Chou Chau, and Hai-Pang Chiang, "Breaking the symmetry of a metal–insulator–metal-based resonator for sensing applications," Nanoscale Research Letters, vol. 17, no. 1, pp. 48, 2022.

[86] M. R. Islam et al., “Design and numerical analysis of a gold-coated photonic crystal fiber based refractive index sensor,” Opt. Quantum Electron., vol. 53, no. 2, Feb. 2021, doi: 10.1007/s11082-021-02748-8.

[87] S. Islam et al., “Extremely low-loss, dispersion flattened porous-core photonic crystal fiber for terahertz regime,” Opt. Eng., 2016, doi: 10.1117/1.oe.55.7.076117.

[88] M. R. Hasan, S. Akter, T. Khatun, A. A. Rifat, and M. S. Anower, “Dual-hole unit-based kagome lattice microstructure fiber for low-loss and highly birefringent terahertz guidance,” Opt. Eng., 2017, doi: 10.1117/1.oe.56.4.043108.

[89] M. R. Islam, M. A. Hossain, K. M. A. Talha, and R. K. Munia, “A novel hollow core photonic sensor for liquid analyte detection in the terahertz spectrum: design and analysis,” Opt. Quantum Electron., 2020, doi: 10.1007/s11082-020-02532-0.

[90] K. Ahmed et al., “Refractive Index-Based Blood Components Sensing in Terahertz Spectrum,” IEEE Sens. J., 2019, doi: 10.1109/JSEN.2019.2895166.

[91] I. K. Yakasai, P. E. Abas, S. Ali, and F. Begum, “Modelling and simulation of a porous core photonic crystal fibre for terahertz wave propagation,” Opt. Quantum Electron., vol. 51, no. 4, pp. 1–16, Apr. 2019, doi: 10.1007/s11082-019-1832-x.

[92] M. S. Islam et al., “A Hi-Bi Ultra-Sensitive Surface Plasmon Resonance Fiber Sensor,” IEEE Access, vol. 7, pp. 79085–79094, 2019, doi: 10.1109/ACCESS.2019.2922663.

[93] S. Chakma, M. A. Khalek, B. K. Paul, K. Ahmed, M. R. Hasan, and A. N. Bahar, “Goldcoated photonic crystal fiber biosensor based on surface plasmon resonance: Design and analysis,” Sens. Bio-Sensing Res., vol. 18, pp. 7–12, Apr. 2018, doi: 10.1016/J.SBSR.2018.02.003.

[94] M. R. M. Islam et al., “Design and analysis of birefringent SPR based PCF biosensor with ultra-high sensitivity and low loss,” Optik (Stuttg)., vol. 221, p. 165311, Nov. 2020, doi: 10.1016/j.ijleo.2020.165311.

[95] Kazi Sharmeen Rashid, Infiter Tathfif, Ahmad Azuad Yaseer, Md. Farhad Hassan, Rakibul Hasan Sagor, Cog-shaped refractive index sensor embedded with gold nanorods for temperature sensing of multiple analytes. Optics Express. 29 (2021) 37541-37554.

[96] X.-P. Jin, X.-G. Huang, J. Tao, X.-S. Lin, Q. Zhang, A novel nanometeric plasmonic refractive index sensor. IEEE transactions on nanotechnology. 9 (2010) 134–137.

[97] Chung-Ting Chou Chao, Yuan-Fong Chou Chau, Hung Ji Huang, N. T. R. N. Kumara, Muhammad Raziq Rahimi Kooh, Chee Ming Lim, Hai-Pang Chiang, 2020. Highly Sensitive and Tunable Plasmonic Sensor Based on a Nanoring Resonator with Silver Nanorods. N*anomaterials.* 10, 1399.

[98] W. K. Jung, K. M. Byun, 2011. Fabrication of nanoscale plasmonic structures and their applications to photonic devices and biosensors. Biomedical Engineering Letters. 1 (2011), 153.

[99] Seung-Woo Lee, Kyeong-Seok Lee, Junhyoung Ahn, Jae-Jong Lee, Min-Gon Kim, Yong-Beom Shin, Highly sensitive biosensing using arrays of plasmonic au nanodisks realized by nanoimprint lithography. ACS nano. 5 (2011) 897– 904.

[100] R. H. Sagor, M. F. Hassan, A. A. Yaseer, E. Surid, and M. I. Ahmed, Highly sensitive refractive index sensor optimized for blood group sensing utilizing the fano resonance. Applied Nanoscience. 11 (2021) 521–534.

[101] Dragan Z. Stupar, Jovan S. Bajić, Ana V. Joža, Bojan M. Dakić, Miloš P. Slankamenac, Miloš B. Živanov, Edvard Cibula, 2012. Remote monitoring of water salinity by using side-polished fiber-optic U-shaped sensor. 15th International Power Electronics and Motion Control Conference (EPE/PEMC).

[102] F. Haider, R. A. Aoni, R. Ahmed, W. J. Chew, and G. A. Mahdiraji, "Alphabetic-Core Assisted Microstructure Fiber Based Plasmonic Biosensor," Plasmonics, vol. 15, no. 6, pp. 1949–1958, 2020.

[103] Md. A. Islam, M. R. Islam, A. M. al Naser, F. Anzum, and F. Z. Jaba, "Square structured photonic crystal fiber based THz sensor design for human body protein detection," J Comput Electron, vol. 20, no. 1, pp. 377–386, Feb. 2021.

[104] M. R. Islam et al., "Surface plasmon resonance based highly sensitive gold coated PCF biosensor," Applied Physics A, vol. 127, no. 2, pp. 118, Feb. 2021.

[105] D. Pysz et al., "Stack and draw fabrication of soft glass microstructured fiber optics," Bull. Polish Acad. Sci. Tech. Sci., vol. 62, no. 4, pp. 667–682, Dec. 2014.

[106] Y. Nishimura et al., "Photolithography," in Flat Panel Display Manufacturing. Hoboken, NJ, USA: Wiley, pp. 287–310, 2018.

[107] P. J. A. Sazio et al., “Microstructured optical fibers as high-pressure microfluidic reactors,” Science, vol. 311, no. 5767, pp. 1583–1586, 2006.

[108] M S Islam et al., “Dual-polarized highly sensitive plasmonic sensor in the visible to near-IR spectrum,” Opt. Exp., vol. 26, no. 23, pp. 30347–30361, 2018.

[109] M. S. M. R. M. Islam et al., “Design and Analysis of a Biochemical Sensor Based on Surface Plasmon Resonance with Ultra-high Sensitivity,” Plasmonics, pp. 1–13, Jan. 2021, doi: 10.1007/s11468-020-01355-9.

List of Publications

Journal

[1] Nasir Muhammad Munim, Tahmina Tabassum Treena, Mohammad Rakibul Islam, and Mirza Muntasir Nishat, "Design and analysis of an ultra-high sensitive and tunable metal-insulator-metal waveguide-coupled octagonal ring resonator utilizing gold nanorods," Sensing and Bio-Sensing Research, vol. 38, pp. 100529, 2022. (Explained in chapter 6)
https://doi.org/10.1016/j.sbsr.2022.100529

[2] Mohammad Rakibul Islam, Tahmina Tabassum Treena, Nasir Muhammad Munim, and Syed Iftekhar Ali, "Peak amplitude difference sensitivity (PADS): An interrogation technique for PCF-SPR sensors using symmetrical arrays of plasmonic layers." Results in Physics, vol. 48, pp. 106434, 2023. (Explained in chapter 7)
https://doi.org/10.1016/j.sbsr.2022.100529